4-5-2017

In Vivo Channel Characterization and Energy Efficiency Optimization and Game Theoretical Approaches in WBANs

Yang Liu
University of South Florida, yangl@mail.usf.edu

In Vivo Channel Characterization and Energy Efficiency

Optimization and Game Theoretical Approaches in WBANs

by

Yang Liu

A dissertation submitted in partial fulfillment
of the requirements for the degree of
Doctor of Philosophy
Department of Electrical Engineering
College of Engineering
University of South Florida

Major Professor: Richard D. Gitlin, Sc.D.
Huseyin Arslan, Ph.D.
Nasir Ghani, Ph.D.
Srinivas Katkoori, Ph.D.
Kaiqi Xiong, Ph.D.

Date of Approval:
February 28, 2017

Keywords: *In vivo* communications, channel modeling, energy efficiency maximization, game theory

DEDICATION

To my family.

ACKNOWLEDGEMENTS

First of all, I would like to dedicate my gratitude to my advisor, Dr. Richard D. Gitlin, for his invaluable guidance, encouragement, support, and trust during my Ph.D. in USF. I am proud to be a member of *i*nnovations in Wireless Information Networking Lab (*i*WINLAB). In this lab, I have gained a lot of experiences and become an expert in my research area, due to Dr. Gitlin's guidance.

Next, I want to express my appreciation to Dr. Kemal Davaslioglu, who has helped me a lot in my research. Without his patient help, I could not make such big progresses in my research and publications. I also learned a lot from him, such as how to come up with ideas from reading the references, how to develop the formulations and so on. I would also like to thank Dr. Thomas Ketterl and Dr. Gabriel Arrobo, who have provided me with valuable advices in my research.

I am thankful to the committee and chair of my dissertation for reviewing my dissertation and making suggestions to my defense. I am grateful to my colleagues our research group for their help and encouragement during my life in USF.

Last but not least, many thanks to my family and all my friends I have in USF for their unconditional support and company.

TABLE OF CONTENTS

LIST OF TABLES

LIST OF FIGURES

ABSTRACT

This dissertation presents several novel accomplishments in the research area of Wireless Body Area Networks (WBANs), including *in vivo* channel characterization, optimization and game theoretical approaches for energy efficiency in WBANs.

First, we performed the *in vivo* path loss simulations with HFSS human body model, built a phenomenological model for the distance and frequency dependent path loss, and also investigated angle dependent path loss of the *in vivo* wireless channel. Simulation data is produced in the range of 0.4−6 GHz for frequency, a wide range of distance and different angles. Based on the measurements, we produce mathematical models for in body, on body and out of body regions. The results show that our proposed models fit well with the simulated data. Based on our research, a comparison of *in vivo* and *ex vivo* channels is summarized.

Next, we proposed two algorithms for energy efficiency optimization in WBANs and evaluated their performance. In the next generation wireless networks, where devices and sensors are heterogeneous and coexist in the same geographical area creating possible collisions and interference to each other, the battery power needs to be efficiently used. The first algorithm, Cross-Layer Optimization for Energy Efficiency (CLOEE), enables us to carry out a cross-layer resource allocation that addresses the rate and reliability trade-off in the PHY, as well as the frame size optimization and transmission efficiency for the MAC layer. The second algorithm, Energy Efficiency Optimization of Channel Access Probabilities (EECAP), studies the case where the nodes access the medium in a probabilistic manner and jointly determines the optimal access

probability and payload frame size for each node. These two algorithms address the problem from an optimization perspective and they are both computationally efficient and extensible to 5G/IoT networks.

Finally, in order to switch from a centralized method to a distributed optimization method, we study the energy efficiency optimization problem from a game theoretical point of view. We created a game theoretical model for energy efficiency in WBANs and investigated its best response and Nash Equilibrium of the single stage, non-cooperative game. Our results show that cooperation is necessary for efficiency of the entire system. Then we used two approaches, Correlated Equilibrium and Repeated Game, to improve the overall efficiency and enable some level of cooperation in the game.

CHAPTER 1. INTRODUCTION[1]

1.1 Wireless Body Area Networks (WBANs)

Wireless communication for biomedical applications and technologies is a research area that has seen a significant increase in attention in recent years. The wireless body area network (WBAN) [1], [2] IEEE 802.15 Task Group 6 studied the devices and technologies on, in or around the human body for various kinds of applications such as healthcare and entertainment.

According to IEEE 802.15.6 standard [3], the available frequency bands for WBAN include Medical Implant Communications Service (MICS), Wireless Medical Telemetry Services (WMTS), Industrial, Scientific and Medical (ISM). The MICS (402-405 MHz) [4] is a low power and unlicensed band which supports diagnostic or therapeutic functions associated with implanted medical devices and applications. The WMTS is used for medical telemetry system and has several scattered bands within the range of 420 MHz to 1.4 GHz. Unlike MICS and WMTS, the ISM band [5] supports high data rate and also has different bands such as 2.4 GHz, 5.8 GHz and up to 245 GHz. Besides these narrow bands, there is also an Ultra Wideband (UWB) available, which ranges from 3.1 GHz to 10.6 GHz [6].

1.2 *In Vivo* Communications and Networking

Our main research focus is *in vivo* wireless communications, which means the study of wireless communication with implanted nodes inside the human body. It is an interesting and

[1] This chapter was published in [21]. Permissions are included in Appendix A.

promising area for its usefulness in bio-medical applications such as Minimally Invasive Surgery (MIS). Modeling the *in vivo* channel is fundamental research that moves forward the other research topics. In practice, it is necessary to explore and understand the effects of using different types of antennas and choose the appropriate kind of antenna for specific scenario. When it comes to the system level, we demonstrate that higher data rates, capacity and better performance can be achieved by using MIMO technology.

Compared to the research on the communication technologies around and on the human body, the research on *in vivo* wireless communication is still in the early stages. The characteristics of the *in vivo* channel are significantly different than those of classical wireless cellular and Wi-Fi systems.

Our research on the *in vivo* wireless communication is ultimately directed towards optimizing the *in vivo* physical layer signal processing, and designing efficient networking protocols that ultimately will make possible the deployment of wireless body area networks inside the human body.

Channel propagation modeling is directed towards creating an empirical mathematical formula to characterize the signal propagation and express it as a function of frequency, distance and other factors. Using such a developed single model can predict the behavior of propagation of all similar links under similar conditions.

The traditional wireless propagation models have been investigated for more than 50 years, and different kinds of channel models have been established [7]. These classic models have provided excellent guidance in designing cellular and WiFi systems, and which has three well-understood components (path loss, shadow fading, and small scale fading). Although the *in vivo*

environment is different from the cellular environment, the basic principles and methods can be still utilized to develop the channel models for WBANs [8]–[15].

In characterizing the *in vivo* channel, we need to consider the inhomogeneous and very lossy nature of the *in vivo* medium. Furthermore, additional factors need to be taken into account, such as near-field effects and highly variable propagation speeds through different organs and tissues.

For the research on MIMO *in vivo*, first, the proper design of the *in vivo* transmit antennas is required for reliable and efficient communications in the *in vivo* environment. Second, we need to set up a software platform for the whole MIMO *in vivo* system (e.g., HFSS [16] and SystemVue [17]). Third, the methods to evaluate the performance of the MIMO *in vivo* system need to be investigated. Fourthly, for some cases with limited physical dimensions, the mutual coupling of the near-field effect needs to be studied and compensated for in order that the MIMO *in vivo* system properly work. Finally, the capacity of the MIMO *in vivo* system needs to be investigated.

We have presented our primary work in MIMO *in vivo* in [18], [19]. In these papers, we evaluated the performance of the MIMO *in vivo* system based upon an IEEE 802.11n system model.

1.3 Energy Efficiency in Wireless Networks

A plethora of sensor applications and wearable technologies exists that enable the ubiquitous recording and storage of vital health signs. With the advances in, and miniaturization of sensors such as implantable medical sensors (i.e., *in vivo* sensors), health and fitness trackers, health monitors, and smart clothing, patients can be monitored without hindering their daily activities. In order to address the unique demands of wireless body area networks (WBANs), the IEEE 802.15.6 standard finalized in 2012 defines a standard for a short-range, extremely low power (also low-duty cycle), and reliable communication to support a variety of applications for

medical monitoring and personal entertainment [20]. The IEEE 802.15.6 standardizes three physical (PHY) layer methods: narrowband PHY, ultra wideband (UWB) PHY, and human body communications PHY. In [21], we are interested in the applications using the UWB PHY instead of the narrowband PHY as UWB PHY is more robust to the channel variations and operates at very low-power levels for human body applications [22].

The application areas, channel models, standards, recent research efforts, and design challenges of WBANs have been studied in numerous surveys, see, e.g., [23]–[25]. Our interest here is on the resource allocation for energy efficiency and throughput.

In [21], we formulate an energy efficiency maximization problem for the IEEE 802.15.6 IR-UWB PHY. We propose a cross-layer optimization algorithm for energy efficiency (CLOEE) to determine the PHY and MAC layer parameters. Specifically, we focus on the optimal payload size and number of pulses per burst. The effects of FEC on the successful packet detection, QoS constraints of minimum throughput, and static power consumption in the circuitry are included in the formulation. We first prove that the energy efficiency is a quasiconcave function of the frame length. Then, we derive closed-form expressions for the optimal frame length that maximizes the energy efficiency and throughput, and propose a low-complexity algorithm to determine the optimal frame length and number of pulses per burst with constraints. We note that prior work in this area has considered either optimization with respect to only one of the parameters and without addressing the rate constraints [26]–[28], or when they did, they relied on high complexity integer programming solutions for narrowband PHY and no closed-form expressions were obtained [29], [30]. In [21], we provide a comprehensive solution to address the shortcomings of the prior work and provide insight on determining where the crossovers of these parameters occur in order to facilitate real-time link adaptation.

1.4 Contributions and Organizations of This Dissertation

The contributions presented in this dissertation are directed to investigate the *in vivo* channel characteristics and optimize the energy efficiency in WBANs.

- *In vivo channel characterization*: A phenomenological *in vivo* path loss [in dB] model was created based on the data obtained by HFSS human body model [31]. Frequency/distance/angle dependent path loss was characterized [32]. A comparison of the characteristics for *ex vivo* and *in vivo* wireless channels was provided [33], [34]. We also obtained the measurements of the channel coefficients for MIMO *in vivo*.
- *Energy efficiency optimization in WBANs*: We created two optimal algorithms, CLOEE and EECAP [35], for energy efficiency maximization in IEEE 802.15.6 IR-UWB WBANs. In CLOEE, a simple, but yet optimal, algorithm was developed to determine the frame sizes and number of pulses per burst. EECAP was created to determine optimal channel access probabilities and frame sizes for each node by considering two different energy efficiency models. Both algorithms are computationally efficient and extendable to 5G/IoT networks.
- *Game theoretical approaches for energy efficiency in WBANs*: A game theoretical model for energy efficiency in WBANs is created [36]. The best response (the strategy that produces the most favorable outcome for a player, taking other players' strategies in account) and the Nash Equilibrium (the concept of a non-cooperative game in which each player is assumed to know the equilibrium strategies of the other players, and no player has anything to gain by changing only his or her own strategy) to the game were investigated to show that cooperation is necessary for efficiency of the entire system.

Correlated Equilibrium and Repeated Game were designed to improve the overall efficiency and enable some level of cooperation in the game.

This dissertation is organized as follows. Chapter 2 presents a literature review for the different research areas in this dissertation. The approaches and simulation results for *in vivo* channel characterization is given in Chapter 3. Two algorithms, CLOEE and EECAP, for optimization of the energy efficiency in WBANs are presented and evaluated in Chapter 4. Several game theoretical methods are studied in Chapter 5 for the same energy efficiency maximization problem in WBANs. Chapter 6 concludes the dissertation and provides some future research directions.

CHAPTER 2. LITERATURE REVIEW[2]

2.1 *In Vivo* Communications and Networking

The classic wireless communications channel has been thoroughly investigated since Hata's pioneering modeling in 1980 [37]. For different scenarios, such as urban, suburban and rural, the channel models can be built by adding appropriate correction factors based on the Hata Model. For wireless network planning, the Standard Propagation Model (SPM) [38] can be used, which is also based on the original Hata model. However, the *in vivo* channel is quite different from the classical wireless channel, as explained in Section I, so it is necessary to build a novel model for it.

There has been some research on the channel modeling for WBAN. The IEEE P802.15 TG6 WBAN channel model provides guidance as to how the channel model should be developed for body area networks. For on/around-body channel modeling [12], [13], [39], [40], the data required by channel modeling can be gathered by conducting physical experiments to obtain the corresponding channel characteristics. For *in vivo* channel modeling, a phantom or a human body model is necessary to be used for measurement. For example, in [41], the authors observed the radio frequency (RF) propagation from medical implants inside a human body via a 3D Immersive Platform. An *in vivo* channel model for homogeneous human tissues was developed in [42]. Using ingested wireless implants, the authors in [43] performed numerical and experimental investigations for biotelemetry radio channels and wave attenuation in human subjects.

[2] This chapter was published in [21]. Permissions are included in Appendix A.

Understanding the *in vivo* wireless channel is critical to advancing many bio-medical and other procedures. The authors [44] performed signal strength and channel impulse response simulations using an accurate human body model and investigated the variation in signal loss at different RF frequencies as a function of position around the human body. In [45], the maximum allowable transmitted power levels for *in vivo* devices was studied in order to achieve a required bit error rates (BER) at the external node (receiver) while maintaining the specific absorption rate (SAR) under a required threshold.

The channel modeling of *in vivo* channel is in a relatively early stage. Unlike the prior research, we consider this problem in three-dimensional space, which is reasonable and necessary for the *in vivo* environment, with the goal of deriving a phenomenological channel model. Also, the familiar properties of *ex vivo* channels need to be investigated for the *in vivo* channel such as shadowing and fading.

For *in vivo* wireless communications, the appropriate design of the implanted antenna is critical, because of the limited space and complex medium inside the human body.

Several different types of implanted antennas have already been designed. The authors in [46] performed a study of two types of implanted antennas --- microstrip antenna and planar inverted-F antenna (PIFA). These two types of antennas are not only popular in classical wireless communication, but also quite appropriate to work as *in vivo* antennas because of their small size and high radiation efficiency. An antenna that works at 2.4-2.48 GHz ISM band was designed in [47] and its dimensions are small enough to meet the requirements of implanted antenna. The authors in [47] also designed a similar implanted antenna at the 402-405MHz MICS band in [48]. In [49], a PIFA working at MICS band was employed and calculated as the antenna located on the surface of the pacemaker since it was able to suppress radiation power toward the inside of the

human body. A implantable microstrip patch antenna working at MICS band was designed in [50] and the design parameters of the antenna was evaluated by using the finite-difference time-domain (FDTD) method. In [51], the authors designed a small-size dual-band implantable antenna for continuous glucose-monitoring applications and developed gels mimicking the human skin to test the designed antenna *in vitro*.

However, most of the antennas in previous research are omnidirectional antennas and there is little research on *in vivo* directional antennas. Since the wavelength is greatly decreased inside the human body and the in-body space is limited, the size of the *in vivo* antenna is much smaller than those in classic wireless environments. The smaller size will result in lower power output of the antenna. For high data rate requirements in transmitting image or video, an antenna that works at higher frequency and wider bandwidth needs to be developed and tested. Also, the testing of the implanted antenna in most of the prior research was performed using man-made homogenous material that is similar to the properties of human body. Therefore, to perform an accurate and practical test, a human body model or a phantom is needed.

MIMO technology, the use of multiple antennas both in transmitter and receiver, can significantly improve the capacity and performance of the communication system in comparison to the conventional system with a single antenna. In modern communications systems, the combination of MIMO and OFDM technology [52] is extremely popular and takes advantage of multipath and materially improves the radio transmission performance.

There has been some research that focuses on MIMO in WBANs. There are a few models for MIMO systems that can be applied to WBANs. In [53], the authors place the antennas on human clothing and analyze the performance of the proposed wearable MIMO systems, which has a significantly better performance than the previous system on a handheld platform. The wideband

body-to-body radio channel in MIMO systems is investigated in [54] and the authors also present several critical characterizations of the channel such as path loss, body shadowing, and small-scale fading.

The previous research is mostly about evaluating the performance of MIMO systems around the human body instead of inside the human body. Our research on MIMO *in vivo* is presented in [18]. We evaluated the performance of MIMO for *in vivo* environment, using ANSYS HFSS [16] and its Human Body Model [55], to determine the maximum data rates that can be achieved using a complete OFDM-based communication (IEEE 802.11n) system in SystemVue. We analyzed the bit error rate (BER) and symbol error rate (SER) for this MIMO system with one pair of antennas placed inside the body and the second pair placed inside and outside the body at various distances from the *in vivo* antennas. The results were compared to SISO simulations and showed that by using MIMO *in vivo*, it is possible to achieve target data rates in the 100 Mbps range at acceptable power levels.

2.2 Energy Efficiency in Wireless Networks

In general, resource allocation for energy efficiency and throughput has been primarily investigated for the narrowband PHY applications, see e.g., [29], [30], [56], [57]. This is probably due to an attractive feature that the standard introduces: a m-periodic scheduled allocation mode where the hub and nodes communicate in every m superframes allowing the nodes to sleep between superframes. The optimal m that maximizes the device lifetime has been investigated in [29], where the current drawn in different states of the nodes are taken into account. The numerical study in [29] was later extended in [30] by solving the problem by integer programming techniques. However, in both studies, the packets are assumed to be error-free and no closed-form expressions were obtained for the optimal MAC parameters. Note that, depending on the size of the problem,

a mixed integer programming solution may be computationally expensive for a low-power device. The effects of erroneous transmissions and forward error correcting (FEC) for m-periodic scheduled allocation mode were numerically evaluated in [56], but again without any closed-form expressions. Reference [57] extended the results of [29], [30], [56] to two-hop relay nodes. Energy efficiency of impulse-radio (IR) UWB PHY for IEEE 802.15.6 applications has been recently studied in the literature, see, e.g., [26]–[28]. These papers have slightly different definitions for energy efficiency. In [26], it is defined as the number of bits that can be successfully received per energy consumption with the units of bits/Joule, whereas the one in [27] divides the energy consumed to generate l payload bits to the one for the payload plus overhead (unitless). Both metrics can be extended to the case that accounts for channel errors. A numerical evaluation is presented in [26] to find the optimal coding rate for different distances and modulations. The optimal frame length without any QoS constraints is determined in [27] using a closed-form expression. The bit error probability of an IR-UWB system that accounts for the effects of intra-symbol interference is derived in [28].

CHAPTER 3. *IN VIVO* CHANNEL CHARACTERIZATION[3]

3.1 HFSS and Its Human Body Model

ANSYS HFSS (High Frequency Structural Simulator) software [16] is a high-performance full-wave electromagnetic (EM) field simulator for arbitrary 3D volumetric passive device modeling that takes advantage of the familiar Microsoft Windows graphical user interface. ANSYS HFSS employs the Finite Element Method (FEM), adaptive meshing, and brilliant graphics for all of 3D EM problems. Through this software, some important parameters and results can be calculated, such as S-Parameters, Resonant Frequency, and Electromagnetic Fields.

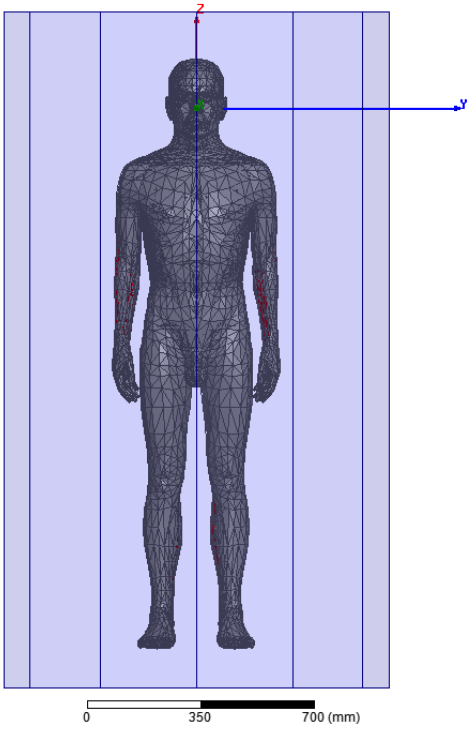

Figure 3.1. HFSS human body model.

[3] This chapter was published in [18-19], [31], [33-34]. Permissions are included in Appendix A.

We use the ANSYS HFSS 15.0.3 Human Body Model software to perform our simulations. The whole human body model is shown in Fig. 3.1. To reduce the required computing resources, we usually cut the whole body and make it into a truncated human body. The human body model contains an adult male body with more than 300 parts of muscles, bones and organs modeled to 1 mm with realistic frequency dependent material parameters. A library file is used to provide the parameters of human-body materials. These parameters are included in datasets of relative permittivity ϵ_r and conductivity σ. The original body model only has the parameters from 10 Hz to 10 GHz. We have increased the maximum operating frequency to 100 GHz by manually adding the values of the parameters to the datasets. So now our human body model can run up to 100 GHz, which is important to our future research at higher frequency. The parameters can be found in [58].

3.2 Simulation Setup

3.2.1 Simulation Setup Using a Hertzian-Dipole

In order to investigate the path loss with minimal antenna effects, we use the Hertzian-Dipole as the antenna, which can be treated as an ideal dipole. The Hertzian-Dipole contains a wire of infinitesimal length δl. It is so small that it has little interaction with its surrounding environment. Also it can be seen as the building block of the practical antennas, because we can interpret the finite length antenna as that it consists of an infinite number of Hertzian-Dipoles. Moreover, the antenna arrays can be represented by means of a plurality of finite length antenna elements. So its unique property is very useful in properly understanding the radiation behavior of a Hertzian-Dipole and it will help to explore the effects of using different types of antennas. More details such as the feeding arrangement and coordinate system for Hertzian-Dipole, radiation fields derived by Maxwell's equations can be found in [6].

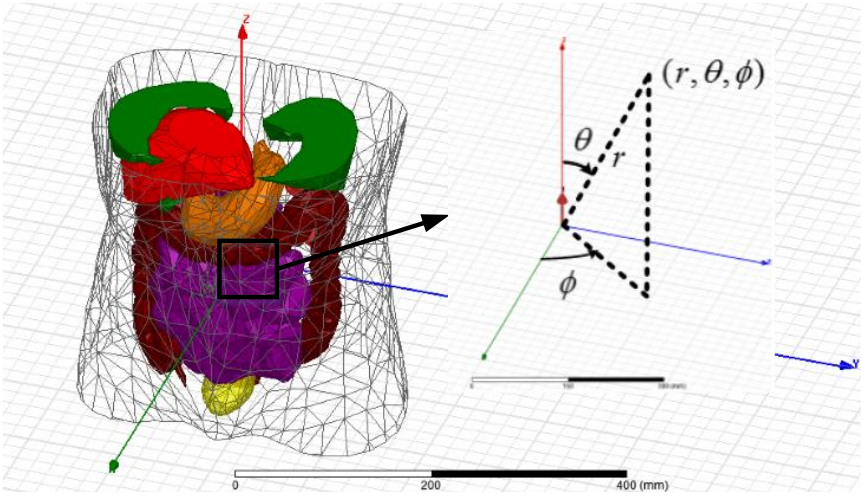

Figure 3.2. Truncated human body with Hertzian-Dipole in spherical coordinate system.

Since the *in vivo* environment is an inhomogeneous medium, it is instructive to measure the path loss in the spherical coordinate system. The truncated human body, the Hertzian-Dipole and the spherical coordinate system are shown in Fig. 3.2. The operating frequency for our simulation is 2.4 GHz ISM band.

The path loss can be calculated as:

$$Path\ loss(r, \theta, \phi) = 10 * \log_{10}\left(\frac{|E|^2{}_{r=0}}{|E|^2{}_{r,\theta,\phi}}\right), \tag{3.1}$$

where r represents the distance from the origin, i.e. the radius in spherical coordinates, θ is the polar angle and ϕ is the azimuth angle. $|E|^2{}_{r,\theta,\phi}$ is the square of the magnitude of the electric E field at the measuring point and $|E|^2{}_{r=0}$ is the square of the magnitude of E field at the origin.

3.2.2 Simulation Setup Using Dipoles

Scattering parameters (S parameters) describe the input-output relationship between ports (or terminals) in an electrical system. Taking the two-port network as an example, a port can be loosely defined as any place where we can deliver voltage and current. So, if we have a

communication system with two radios (radio 1 and radio 2), then the radio terminals (which deliver power to the two antennas) would be the two ports.

In the two-port network, there are four S parameters. S_{11} is defined as the return loss of antenna 1, which is the reflected power that radio 1 is trying to deliver to antenna 1. S_{22} is similarly defined for antenna 2. S_{12} is the power from radio 2 that is delivered through antenna 1 to radio 1. Note that in general S-parameters are a function of frequency (i.e. vary with frequency). In our simulation in HFSS, if we set Port 1 on transmit antenna and Port 2 on receive antenna, then S_{21} represents the power gain of Port 1 to Port 2, that is

$$|S_{21}|^2 = \frac{P_r}{P_t}. \tag{3.2}$$

Therefore, including the antenna gains, we can calculate the path loss by the formula below,

$$Path\ loss(dB) = -20\log_{10}|S_{21}|. \tag{3.3}$$

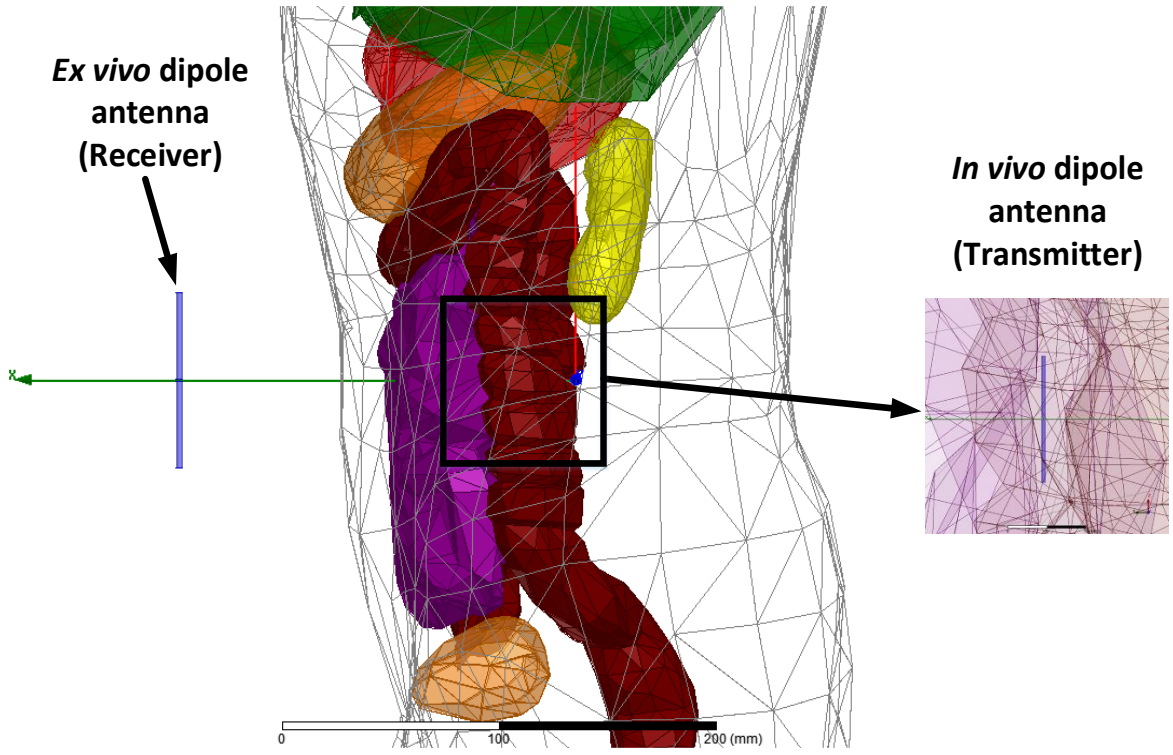

Figure 3.3. HFSS simulation setup by using dipole antennas.

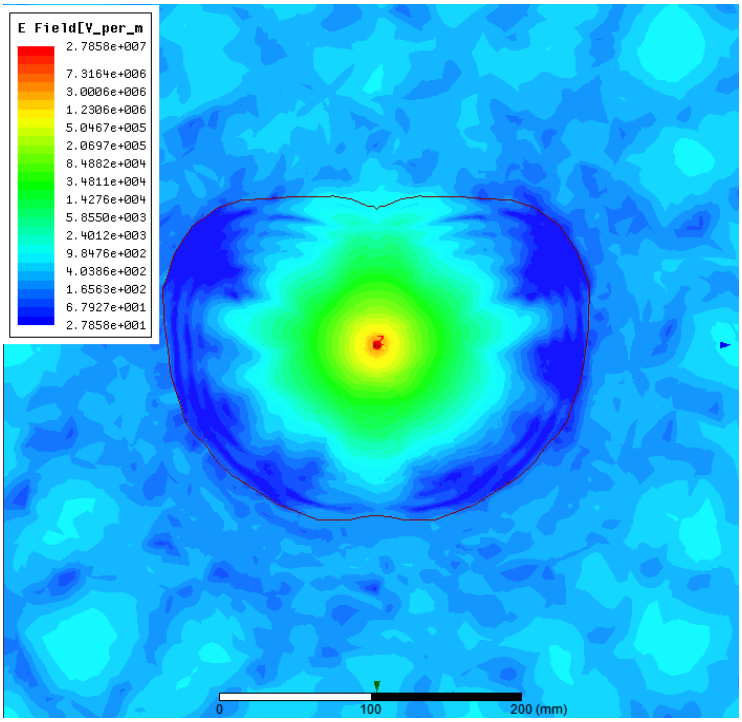

(a)

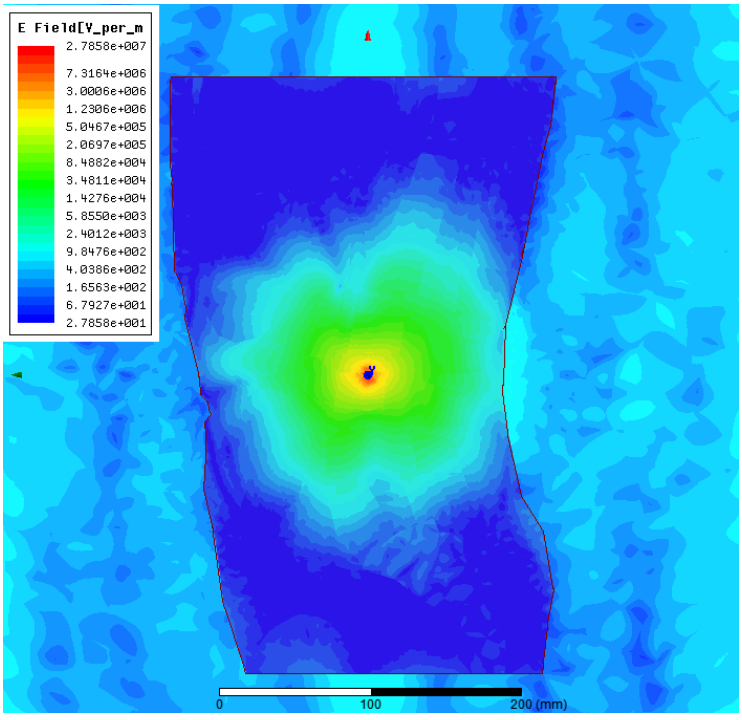

(b)

Figure 3.4. Top view of E field plot on the XY plane and right side view of E field plot on the XZ plane.

In practice, we choose dipole in our simulation setup, which is shown in Fig. 3.3. In the Cartesian coordinate system, the *in vivo* transmit antenna is fixed at (35mm, 0, 0), which is located behind the small intestine. The receive antenna is moving along the X-axis and it has the same size as the transmit antenna when it is inside the body. When the receive antenna is outside the body, it equals to the size of the free space dipole antenna, which is as 4−6 times as large as the *in vivo* antenna, since the wavelength in free space is as 4−6 times longer than inside the body.

The frequency range we are investigating is from 0.4 GHz to 6 GHz. Since a dipole is not a wideband antenna, we choose seven dipoles that operating at different frequencies (0.4, 0.7, 1.2, 1.7, 2.4, 3.5 and 5.0 GHz) to cover this frequency range. The measuring distance ranges from $\lambda/50$ to 3λ, where λ is the free space wavelength.

Considering the return loss of the antenna is not constant at each measuring frequency and even at different positions, we develop the following formula as a modification to (3.3) to calculate the path loss and remove the effects on antenna gains from different return losses,

$$Path\ Loss\ (dB) = -S_{21} + 10 * \log_{10}\left(1 - 10^{\frac{S_{11}}{10}}\right) + 10 * \log_{10}\left(1 - 10^{\frac{S_{22}}{10}}\right), \quad (3.4)$$

where S_{11} and S_{22} are the return losses of the transmit and receive antennas, respectively. The parameter S_{21} represents the power gain between these two antennas and all S-parameters are expressed in dB.

3.3 Simulation Results

3.3.1 Overview of the Attenuation from E Field Plots

Figure 3.4 shows the E field strength distribution that is produced by a Hertzian-Dipole at 2.4 GHz on the XY and XZ plane. The red boundary is the body exterior. From these results, we can see the Electric field inside the body first attenuates rapidly within a short distance ($r < 30mm$) and then attenuates smoothly. The main reason for this phenomenon is that the human organs and

tissues absorb a lot of the energy. Inside the body, the attenuation is very high and also varies with angle. Outside the body, many constructive and destructive waves are caused by reflections and refractions, which result in the fluctuant E field. In general, the path loss at front of the body is higher than that at the back, due to more organs being present at the front.

3.3.2 Simulation Results Using Hertzian-Dipole

3.3.2.1 Path Loss vs. Distance

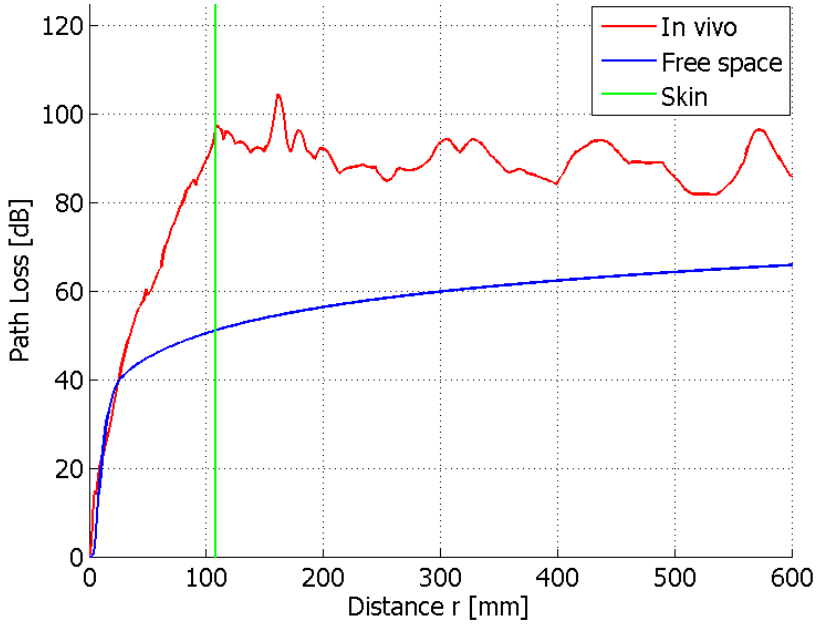

Figure 3.5. Path loss vs. distance at azimuth angle $\phi = 0°$ and polar angle $\theta = 90°$

When we fix the azimuth and polar angles to 0° and 90°, respectively, we obtain the relationship between path loss and distance, as shown in Fig. 3.5. For the *in vivo* case, the skin boundary is at $r = 108mm$. We can clearly observe the different behavior of the path loss between the *in vivo* and *ex vivo* regions. In the body, the path loss increases rapidly and the curve can be approximately seen as a line with a slope of 0.815 dB/mm. Outside the body, there exist many constructive and deconstructive waves, which come from refractions through the skin. These waves make the path loss fluctuant.

In contrast, at the skin boundary, the *in vivo* path loss is about 45 dB greater than the free space path loss. In the range of $r = 108 - 600\ mm$, the difference between *in vivo* and free space path loss fluctuates within 18 dB to 50 dB. Both the free space and *in vivo* path losses initially increase rapidly, but the *in vivo* path loss rises rapidly inside the body while free space path loss also does so for $r = 1 - 20\ mm$, which is exactly the free space near field region.

3.3.2.2 Path Loss vs. Azimuth Angle

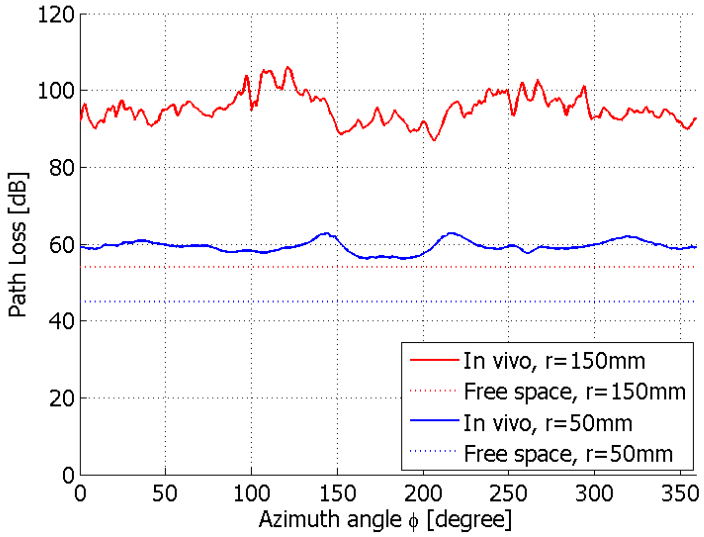

Figure 3.6. Path loss vs azimuth angle at polar angle $\theta = 90°$ and distance $r = 150mm, 50mm$.

In this simulation, we vary the distance $r = 150\ mm/50mm$ and fix the polar angle at $\theta = 90°$. In this way, we obtain the path loss vs azimuth angle as shown in Fig. 3.6. Overall, the *in vivo* path loss is about 32-52 dB greater than the free space path loss at $r = 150\ mm$, which is outside the body. At $r = 50\ mm$, which is inside the body, the difference between *in vivo* and free space path loss is 11-18 dB. We can see that the free space path loss is flat and the *in vivo* path loss varies with azimuth angle. The variation is larger for the region outside of the body than inside the body. At $r = 150\ mm$, we note that the path loss is lower at the back of the body, when azimuth angle $\phi = 150° - 210°$. These fluctuations show that the human body is inhomogeneous

as expected and, consequently, that the path loss is angular dependent. Compared with our another method of measuring the path loss by using monopole [44], we found the path loss measured by using Hertzian-Dipole has less angular variation than that by using monopole. Therefore, we assume that the significant variations in Received Signal Strength is caused by both the angular dependent path loss and the significantly modified *in vivo* antenna effects.

3.3.2.3 Path Loss vs. Polar Angle

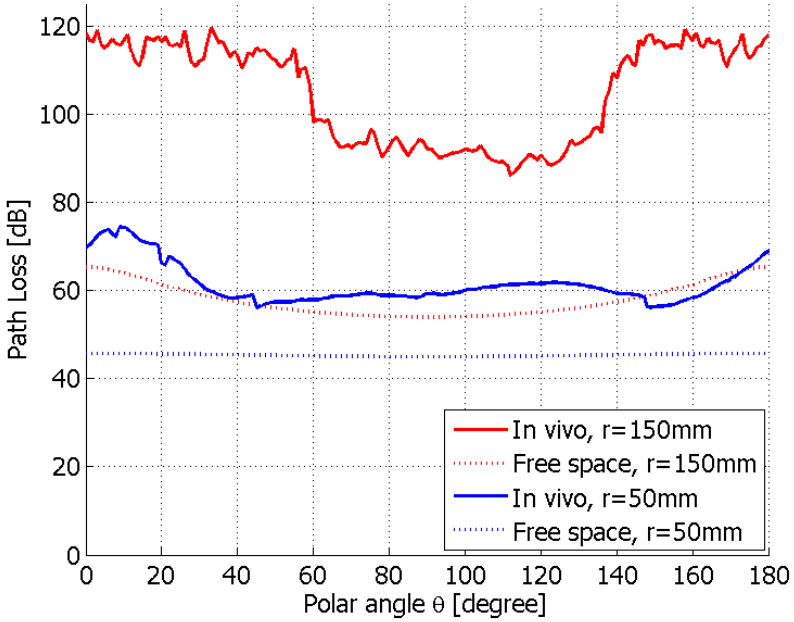

Figure 3.7. Path loss vs polar angle at azimuth angle $\phi = 0°$ and distance $r = 150mm, 50mm$.

Figure 3.7 shows the path loss vs polar angle when the distance $r = 150mm/50mm$ and azimuth angle $\phi = 0°$. For the case of $r = 150mm$, the *in vivo* path loss curve is fluctuating and also has a concave within $\theta = 60° - 135°$. The cause of this concave is that the path is outside the body in this range, which makes it has less attenuation. The reason why the curve of the free space path loss appears as an arch instead of a flat line is that the Hertzian-Dipole has some effects on the path loss in different polar angles because of its donut-shaped antenna pattern. However, when the distance $r = 50mm$, the free space path loss is almost a flat line, which means that there

is little antenna effect. For the *in vivo* path loss at $r = 50mm$, we observe that there is an arch at $\theta = 45° - 145°$. This is because the path is passing through the small intestine, which makes the path loss relatively greater.

3.3.3 Simulation Results Using Dipoles

3.3.3.1 Frequency and Distance Dependent Path Loss

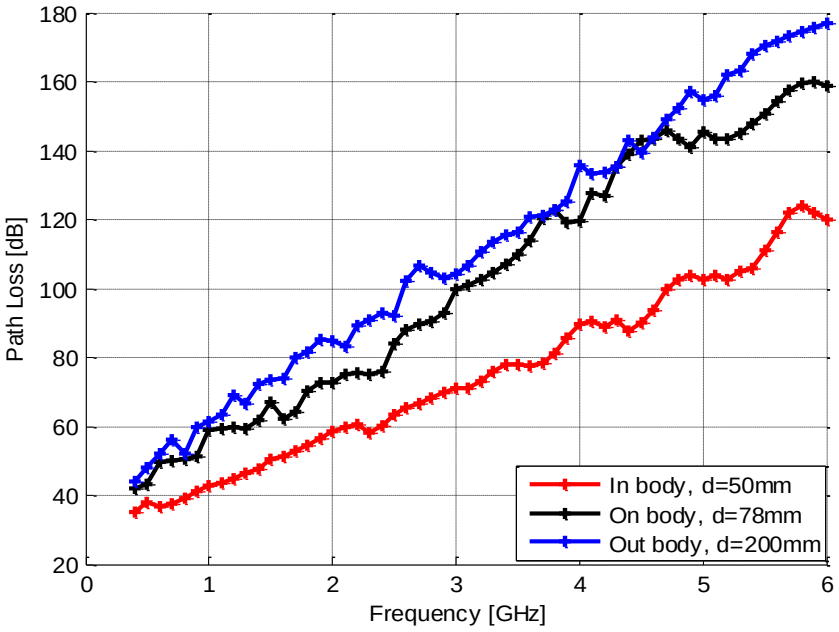

Figure 3.8. Frequency dependent path loss at different locations.

We denote the distance between transmit and receive antennas as d in mm and the frequency as f in GHz. The skin boundary of the body is at $d = 78mm$. From the measured data, we plot the frequency dependent path loss in Fig. 3.8 for three different positions: $d = 50mm$ (in body), $d = 78mm$ (on body), $d = 200mm$ (out of body). From the results, we observe that the frequency dependent path loss [in dB] increases linearly at different locations. Therefore, the frequency dependent *in vivo* path loss [in ratio] increases exponentially, which is faster than that in free space.

In Fig. 3.9 and Fig. 3.10, the distance dependent path loss at different frequencies is shown. We measured the path loss from 0.4 GHz to 6 GHz in 0.1 GHz increment. In the figures, we only

display the optimal operating frequencies for all the seven dipoles. We observe that the path loss [in dB] increases linearly inside the body and then grows logarithmically outside the body.

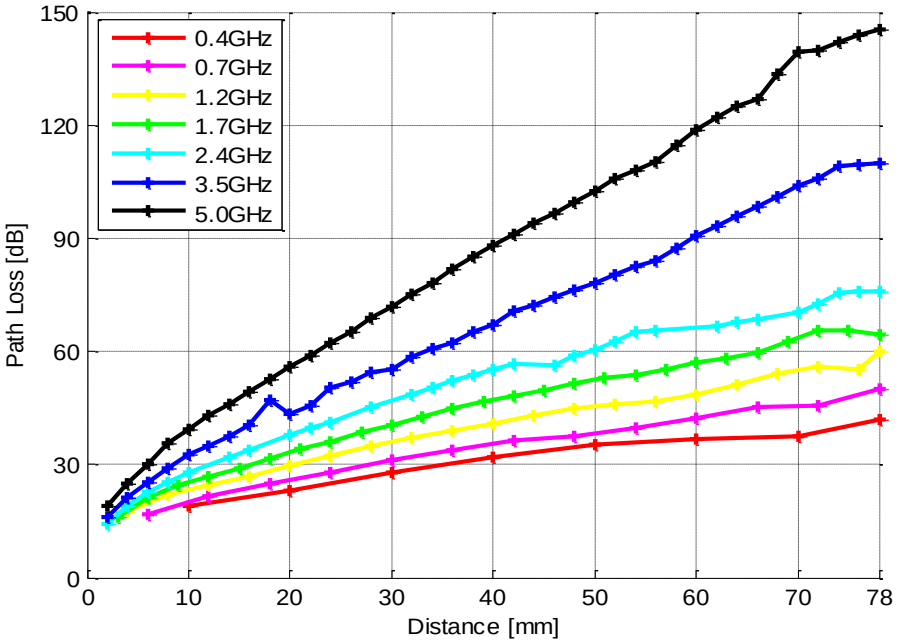

Figure 3.9. In body distance dependent path loss.

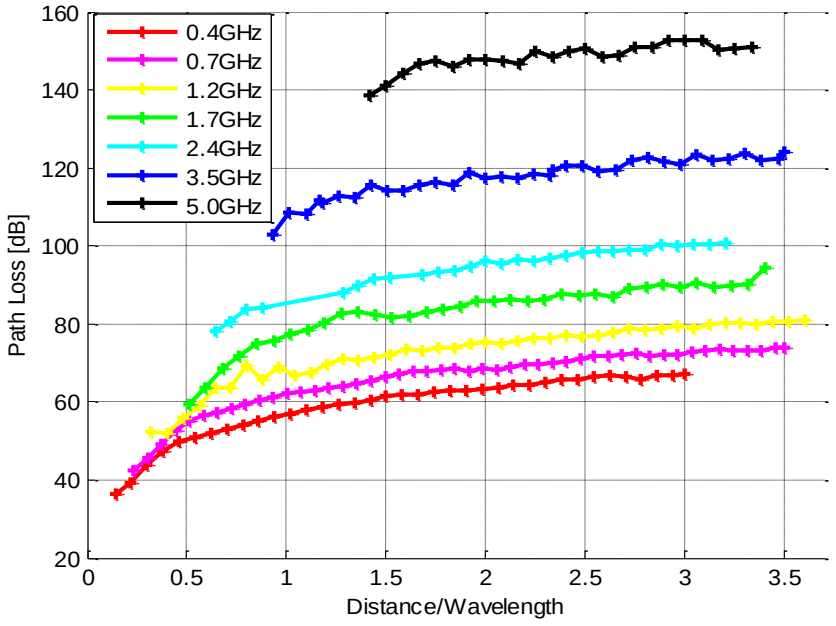

Figure 3.10. Out of body distance dependent path loss.

3.3.3.2 Data Fitting

The observations in Section 3.3.3.1 provides us with important guidance for fitting the measured data into a phenomenological model. We use the Curve Fitting Toolbox in MATLAB to perform the data fitting. The procedure is described below.

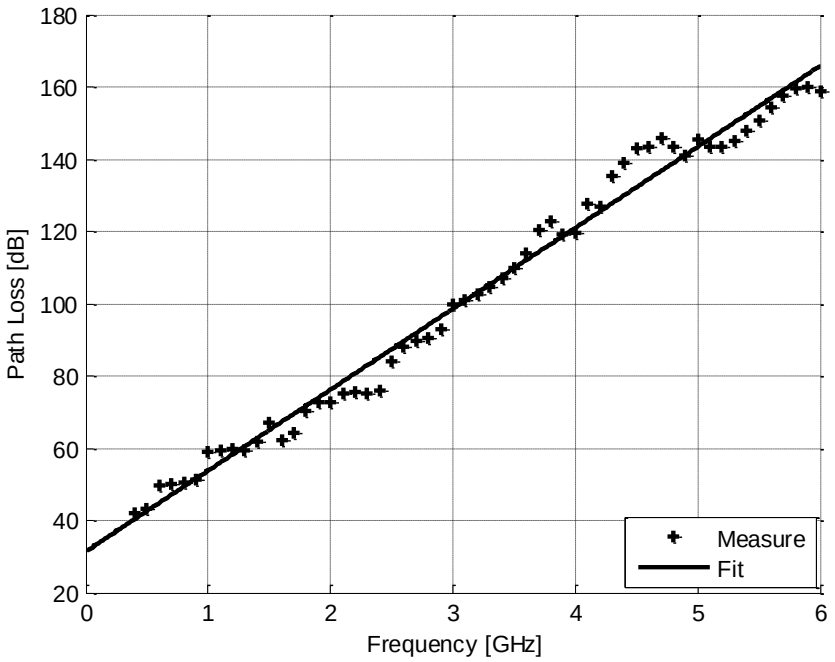

Figure 3.11. On body path loss fitting.

First, we perform the curve fitting for on body path loss. For both regions inside and outside the body, we will choose the on body location as the reference point. Consequently, we first fit the on body path loss data as a straight line shown in Fig. 3.11. The fitted line is

$$PL_{on\ body} = 22.4 * f + 31.4. \tag{3.5}$$

Next, we perform the curve fitting for in body path loss. As we observed in Fig. 3.9, the in body path loss increases linearly and we choose the reference point on the body and fit the data at all frequencies. The fitted results are,

$$PL_{in\ body} = PL_{on\ body} + k * (d - 78). \tag{3.6}$$

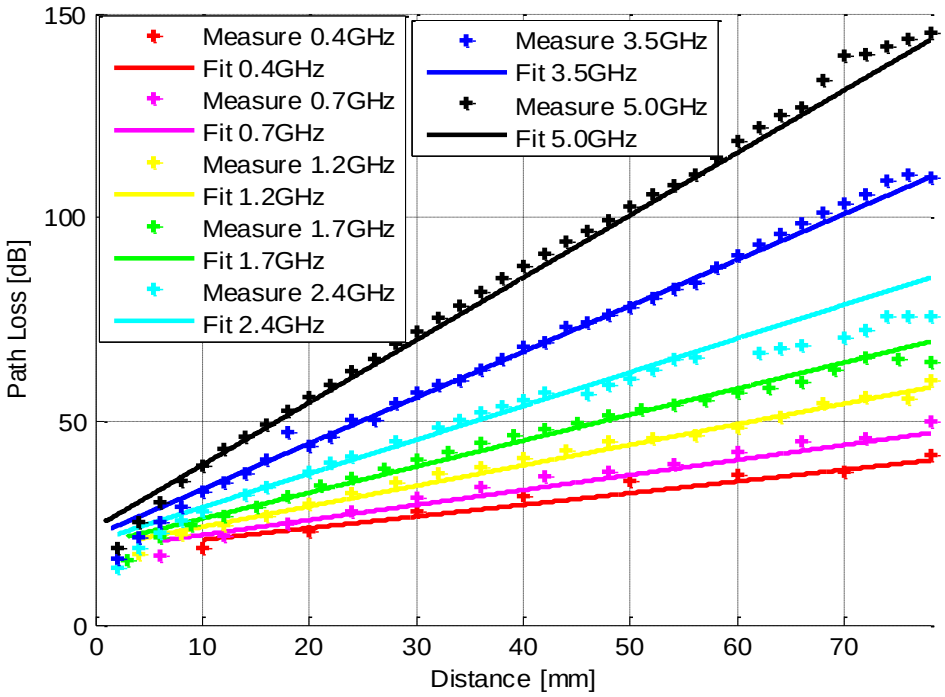

Figure 3.12. In body path loss fitting.

The parameter k is the slope for the path loss at each frequency and it can be fitted as $k = 0.271 * f + 0.1782$. In Fig. 3.12, we compare the measured data with the fitted lines. This model indicates that the in body path loss increases exponentially with distance, which is faster than the free space path loss.

Finally, we do the curve fitting for out of body path loss. The operation is similar to last step. The fitted formula is,

$$PL_{out\ of\ body} = PL_{on\ body} + 10 * \log_{10}\left(\frac{d}{78}\right)^{n}, \tag{3.7}$$

where $n = 1.71 - 2.37$ is the exponent for the path loss at each frequency. In our measured data, the exponent has an average value of $n = 2.04$. So the out of body path loss is similar to the free space path loss. We plot the measured data versus the fitted data in Fig. 3.13. From Fig. 3.11 to Fig. 3.13, we can see that our proposed models (3.5)−(3.7) generally fit well with the measured

data, except for two regions: one is the near field region of the in body antenna and the other is the out of body region closer to the body-air interface. It can be seen that the measured path loss slightly drops when the receiver just gets out of the medium. We assume that slight miscalculations by HFSS occur at the body-air interface because of multiple reflections and refractions.

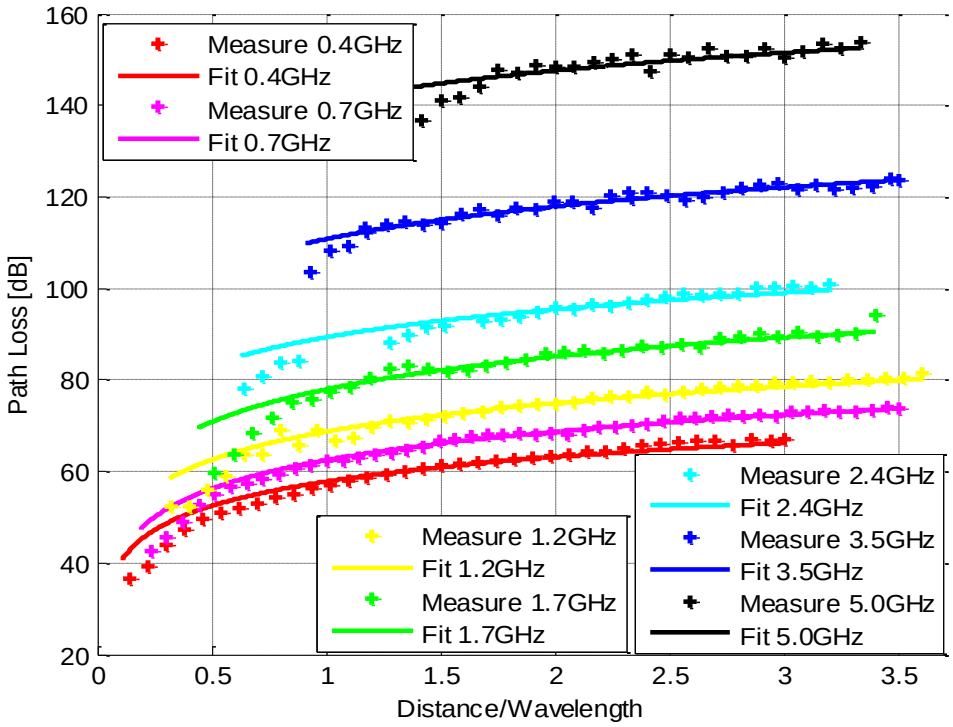

Figure 3.13. Out of body path loss fitting.

3.3.3.3 Angle Dependent Path Loss

The angular dependent characteristics of the *in vivo* channel are investigated by performing further simulations at 0.4 GHz, 1.4 GHz and 2.4 GHz. The *in vivo* antenna is fixed inside the abdomen (78mm in depth from body surface) and the *ex vivo* antenna is rotated on the body surface with the azimuth angle of $0° - 355°$ with $5°$ increment. The results are presented in Figure 3.14 and Table 3-1. It could be observed that the angular dependency (i.e. the variation of the path loss vs. azimuth angle) in terms of peak to average ratio is similar for different frequencies.

Table 3-1. Comparison of angular dependent path loss at different frequencies.

Frequencies (GHz)	**0.4**	**1.4**	**2.4**
Average (dB)	46.316	76.74442	108.8819
Maximum difference (dB)	20.3373	33.04337	45.38211
Peak to Average Ratio	1.197665	1.171730	1.208047

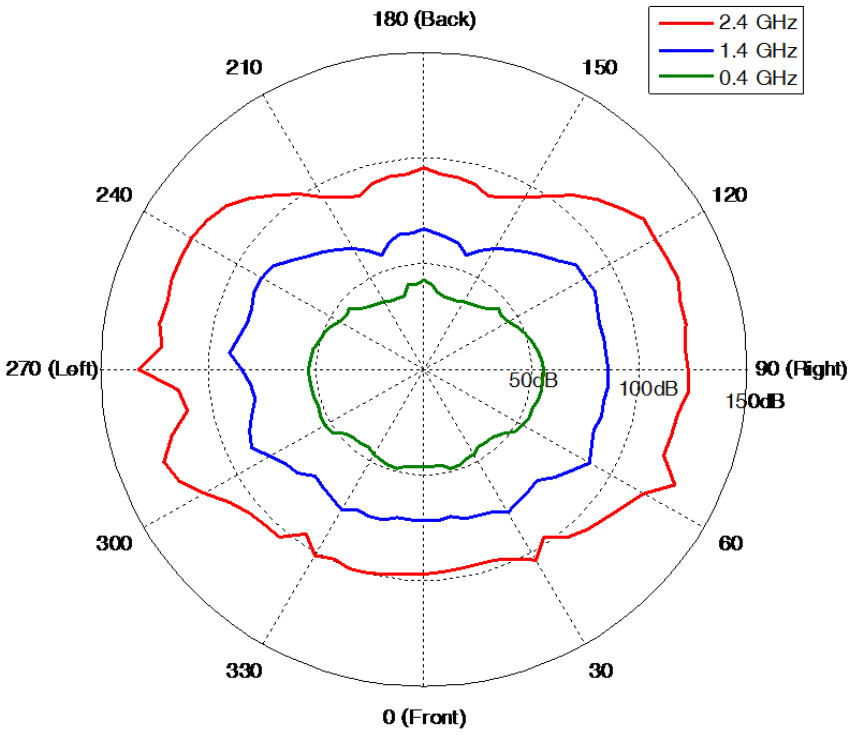

Figure 3.14. Angular dependent path loss for on body receiver.

3.4 Specific Absorption Rate (SAR) Limit

Since we are transmitting through or near the human body, the signal levels are limited to the safety guidelines set by the Federal Communications Commission (FCC). SAR levels of radio frequency (RF) radiation produced by cellular phone activity near the human head have already been extensively investigated [59]–[61]. SAR effects near other parts of the human body, such as in body area networks (BAN) applications [1] have also seen increased attention [62]. However, to the best of our knowledge, research in SAR levels produced by *in vivo* devices has so far been very limited [63]. Although, in [63], the authors provided results for SAR and BER evaluation for

implanting BAN's operating at the 400 MHz ISM band. But due to an increasing need to provide high data rate in *in vivo* communications, it is essential to evaluate the SAR under BER requirements at higher frequencies. Such results will give the system designer guidance about whether a relay network will be needed to attain reliable communications through the extremely lossy and dispersive *in vivo* channel [44]. In [45], the authors calculate the SAR levels and communication BER using a software-based test bench, where the system designer can easily monitor the performance of the communication while, at the same time, observing the SAR levels in highly accurate *in vivo* environments.

3.5 MIMO *In Vivo*

In [18], [19], we present MIMO technology in the *in vivo* environment, which is motivated by the high data rate requirements (~100 Mbps) of wirelessly transmitted low-delay High Definition video during Minimally Invasive Surgery (MIS). Various factors are considered in the MIMO *in vivo* study including antenna separation distances, antenna angular positions, human body size, and system bandwidth to determine the maximum data rate that can be supported, while satisfying the specified Specific Absorption Rate (SAR) power limitations. It is shown that by using MIMO *in vivo*, significant performance gain can be achieved, making it possible to achieve target data rates of ~100 Mbps with appropriate antenna placements and system bandwidth.

We use ANSYS HFSS Human Body Model and Agilent SystemVue as simulation tools. The antennas used in the simulations are monopoles in the 2.4 GHz ISM band. On average, the wavelength is approximately six times smaller *in vivo* than in free space, so that the antenna separation for the Tx and Rx antennas is different for the *ex vivo* and *in vivo* antennas. The simulation set up is shown in Fig. 3.15. Simulations are made considering 9 different distances and different angular positions between Tx and Rx antennas. The system capacity analysis and

FER (Frame Error Rate) performance in the *in vivo* environment have been performed based on the IEEE 802.11n standard transceiver. Agilent SystemVue is used to simulate the FER performance. The channel S-parameters between Tx and Rx antennas were extracted from HFSS.

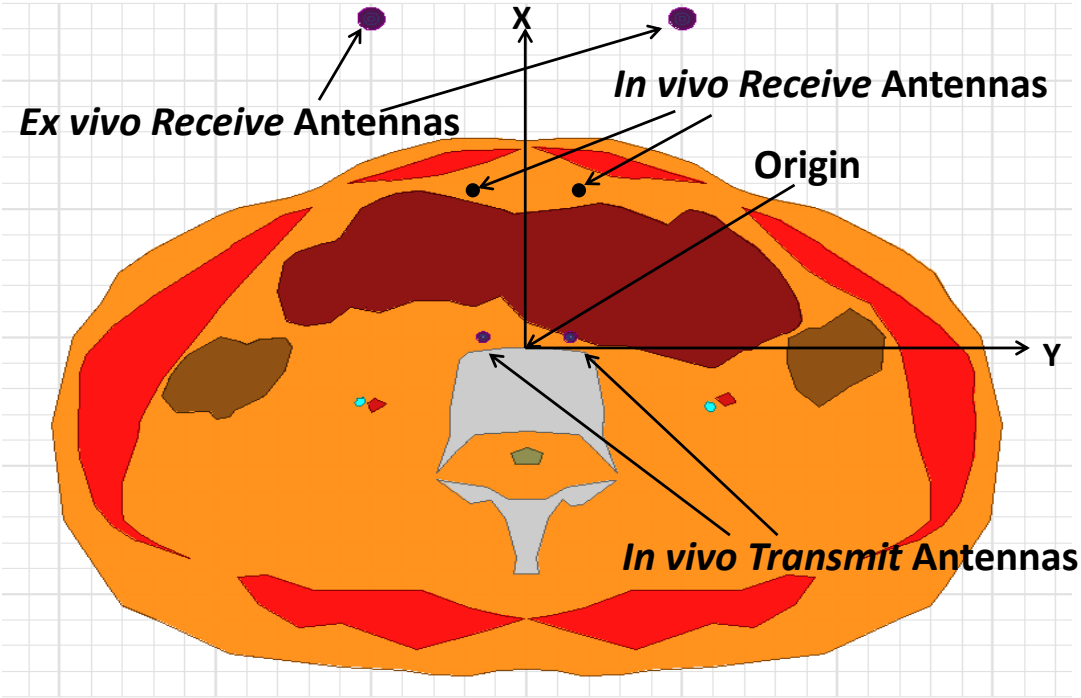

Figure 3.15. Antenna simulation setup showing locations of the MIMO antennas.

To meet the specified SAR and data rate requirements of 100 Mbps, for a distance between Tx and Rx antennas greater than 11 cm for a 20 MHz channel and 13 cm for a 40 MHz channel, a relay is necessary. MIMO *in vivo* can improve system capacity relative to SISO *in vivo* within that distance. As the Tx and Rx antenna separation becomes smaller, the performance gain becomes even bigger. Significantly higher system capacity can be observed when receiver antennas are paced at the back or the front of body than when placed at the side of the body. The SAR power limit significantly affects the MIMO *in vivo* system performance. With the constraint of a maximum allowed SAR level, an increased system bandwidth will increase MIMO *in vivo* system capacity.

3.6 Comparison of *In Vivo* and *Ex Vivo* Channel

Table 3-2. Comparison of *in vivo* and *ex vivo* channel.

Feature	***Ex vivo***	***In vivo***
Physical Wave Propagation	Constant speed Multipath − reflection, scattering and diffraction	Variable speed Multipath − plus penetration
Attenuation and Path Loss	Lossless medium Decreases inversely with distance	Very lossy medium Angular (directional) dependent
Dispersion	Multipath delays → time dispersion	Multipath delays of variable speed → frequency dependency → time dispersion
Directionality	Propagation essentially uniform	Propagation varies with direction Directionality of antennas changes with position/orientation
Near Field Communications	Deterministic near-field region around the antenna	Inhomogeneous medium → near field region changes with angles and position inside body
Power Limitations	Average and Peak	Plus specific absorption rate (SAR)
Shadowing	Follows a *log-normal* distribution	To be determined
Multipath Fading	Flat fading and frequency selective fading	To be determined
Antenna Gains	Constant	Angular and positional dependent Gains highly attenuated
Wavelength	The speed of light in free space divided by frequency	$\lambda = \frac{c}{\sqrt{\varepsilon_r} f} \rightarrow$ at 2.4GHz, average dielectric constant $\varepsilon_r = 35 \rightarrow$ roughly 6 times smaller than the wavelength in free space.

Based on our research in Section 3.1-3.5, we summarize the different characteristics of *in vivo* channel versus *ex vivo* channel in Table 3-2.

3.7 Concluding Remarks

In the simulation of using Hertizian-Dipole, we used HFSS software and Human Body Model to calculate the electric field caused by a Hertzian-Dipole at the origin and obtained the *in vivo* path loss versus different parameters in spherical coordinates. From our initial results we observed the different behaviors of the path loss between *in vivo* and *ex vivo* environments. Great attenuation is caused by the human body and the *in vivo* path loss can be up to 40 dB greater than

the free space path loss. Also the inhomogeneous medium results in the angular dependent path loss. We also compared the results to the method of using monopole antennas and found the angular dependent signal variation was caused by both the angular based path loss and *in vivo* antenna effects. This initial research is a first-step in building an *in vivo* channel model and in exploring the different types of *in vivo* antenna effects.

From the simulations of using regular dipoles, we proposed a phenomenological *in vivo* path loss model based on the measured data obtained by HFSS simulations. First we found some important characteristics for the *in vivo* path loss. The path loss increases linearly with frequency at different locations. Inside the body, the path loss also increases linearly in dB with distance except for the near field region. Outside the body, the path loss grows logarithmically with distance similar to free space. These characteristics enable us to fit the model for three different regions: on body, in body and out of body. The on body path loss is modeled as a straight line [in dB] versus frequency and it acts as the reference point for the other two regions. The in body path loss is also modeled as a straight line with both frequency and distance as the parameters. The out of body path loss is modeled as a logarithmical curve with an exponent of 1.71−2.37 on the distance, which is similar to the exponent of 2 on the distance for the free space path loss. Angle dependence is also investigated and we found that the angular variance is similar at different frequencies in terms of peak-to-average ratio.

CHAPTER 4. ENERGY EFFICIENCY OPTIMIZATION IN WBANS[4]

4.1 Overview of the IEEE 802.15.6 UWB

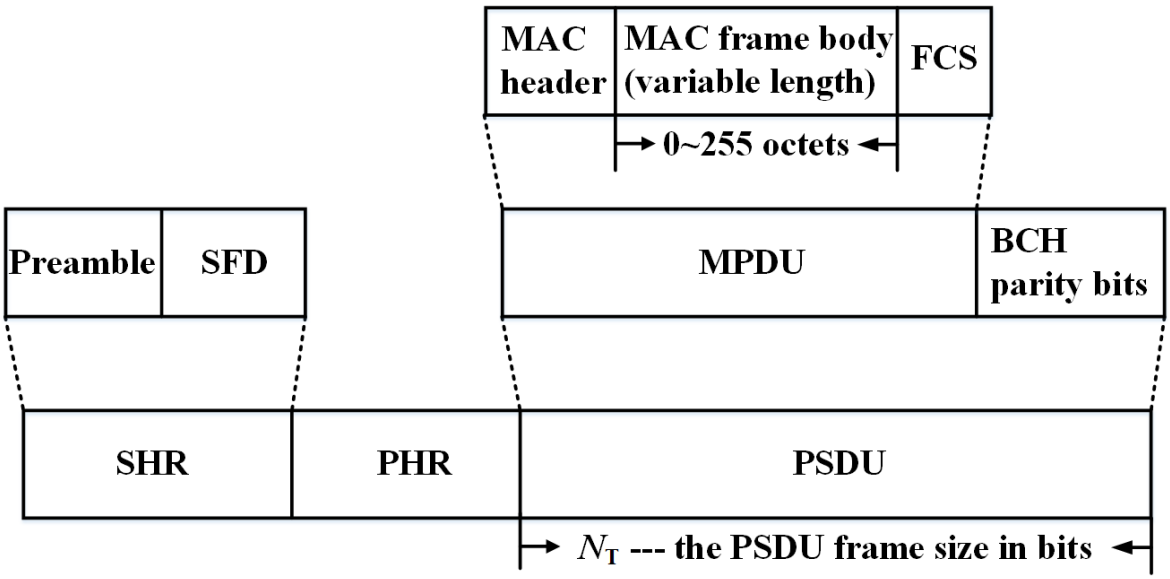

Figure 4.1. IEEE 802.15.6 UWB PPDU frame structure

We consider a set of WBAN sensor nodes and a master hub node in which the medium access and power management functionalities are coordinated by the hub. According to the IEEE 802.15.6 standard, a hub can serve up to 64 nodes [20]. Eleven channels are defined for the UWB PHY in the 3.1-10.6 GHz spectrum band, each with a channel bandwidth of 499.2 MHz. There are three supported modulation schemes for IR-UWB, namely on-off modulation, differential binary phase shift keying (DBPSK) and differential quadrature phase shift keying (DQPSK). There are two modes of operation defined in [20] such as the default and the high QoS modes. The default mode is for the medical and non-medical applications, whereas the high QoS

[4] This chapter was published in [21,35]. Permissions are included in Appendix A.

mode is to be used for high-priority medical applications only. In the section, we only discuss the default mode.

4.1.1 UWB PHY Superframe Structure

The UWB PHY frame format is referred to as the physical layer protocol data unit (PPDU). It is composed of the synchronization header (SHR), the physical layer header (PHR), and the physical layer service data unit (PSDU) as illustrated in Fig. 4.1. The PPDU duration is given by

$$T_{\text{packet}} = T_{\text{SHR}} + T_{\text{PHR}} + T_{\text{PSDU}}, \tag{4.1}$$

where the SHR, PHR, and PSDU frame durations are denoted by T_{SHR}, T_{PHR}, and T_{PSDU}, respectively.

The SHR frame consists of two parts. The first part is the preamble and it is used for timing synchronization, packet detection, and carrier frequency offset recovery. The preamble also enables the coexistence of WBANs [20]. The second part is the start-of-frame delimiter (SFD) for frame synchronization. The preamble and SFD are made up of four and one Kasami sequences of 63 bits, respectively. Between the bits of a Kasami sequence, $L - 1$ zeros are padded. To keep the duty cycle low, $L \cdot T_w$ is fixed to 128 nsec [20]. We take $T_w = 8$ nsec, $L = 16$, and $T_{\text{SHR}} = 5 \cdot 63 \cdot 128$ nsec $= 40.32$ μsec as in [20].

Table 4-1. BCH($n, k;\ t_{\text{ECC}}$) error correcting codes of the PHR and PSDU frames in the IEEE 802.15.6 UWB PHY.

Frame Type	Default Mode	High QoS Mode
PHR	BCH (40,28:2)	BCH(91,28;10)
PSDU	BCH(63,51;2)	BCH(126,63;7)

The PHR frame consists of 24 bits that carry information about the data rate of the PSDU, MAC frame body length, pulse shape, burst mode, HARQ, and scrambler seed. A shortened Bose-Chaudhuri-Hocquenghem (BCH) code of $(40,28;2)$ is used such that $k = 28$ bits are appended

with parity bits to form codewords of length $n = 40$ bits with an error correcting capability of $t_{\mathrm{ECC}} = 2$. Hence, the PHR frame bits, $N_{\mathrm{PHR}} = 40$, are transmitted at a sampling rate of 2051.2 nsec, i.e., $T_{\mathrm{PHR}} = 40{\times}2051.3$ nsec $= 82.052$ μsec.

Table 4-2. Data rate and symbol timing related parameters of the IEEE 802.15.6 UWB PHY.

N_{cpb}	T_w (nsec)	T_{sym} (nsec)	Uncoded Bit Rate (Mbps)	Coded Bit Rate (Mbps)
32	64.103	2051.3	0.488	0.395
16	32.051	1025.6	0.975	0.790
8	16.206	512.8	1.950	1.580
4	8.012	256.4	3.900	3.159
2	4.006	128.2	7.800	6.318
1	2.003	64.1	15.600	12.636

The PSDU includes the MAC protocol data unit (MPDU) and the channel code, BCH parity bits, in the default mode. The MPDU consists of a MAC header, a variable length MAC frame body, and a frame check sequence (FCS). The header and FCS of the MPDU frame are $N_{\mathrm{FCS}} = 56$ and $N_{\mathrm{MH}} = 16$ bits, respectively. The MAC frame body has a variable length of N'_{FB} bits. Thus, in a MPDU frame, the total number of bits before bit stuffing are given as

$$N'_{\mathrm{MPDU}} = N_{\mathrm{MH}} + N_{\mathrm{FCS}} + N'_{\mathrm{FB}}. \tag{4.2}$$

These are grouped in blocks of length k to codewords of length n. In Table 4-1, the error correcting codes (ECC) for the PHR and PSDU frames are summarized for the default and high QoS modes, where we follow the notation $(n, k; t_{\mathrm{ECC}})$ for the BCH codes. To align the symbol boundaries, bits are padded to the last word if $\mathrm{rem}(N'_{\mathrm{FB}} + 72, k) \neq 0$, where $\mathrm{rem}(x, y)$ is the remainder of x divided by y. In that case, the last codeword would require

$$N_{\mathrm{bs}} = N_{\mathrm{CW}}k - N'_{\mathrm{MPDU}} \tag{4.3}$$

bit stuffing such that the total number of bits before encoding becomes

$$N_{\mathrm{MPDU}} = N'_{\mathrm{MPDU}} + N_{\mathrm{bs}}. \tag{4.4}$$

When the BCH parity bits are included, the total number of payload bits for the PSDU frame becomes

$$N_{\mathrm{T}} = N_{\mathrm{MPDU}} + (n-k)N_{\mathrm{CW}}. \tag{4.5}$$

The duration of the PSDU frame is $T_{\mathrm{PSDU}} = N_{\mathrm{T}}/R_b$, where R_b is one of the uncoded bit rates in Table 4-2. The problem formulation in Section 4.2.2 will use the N_{T} to relate the error probability which depends on the number of code words N_{CW}. Since $N_{\mathrm{MH}} + N_{\mathrm{FCS}} = 72$ bits, we can express N_{CW} as

$$N_{\mathrm{CW}} = \left\lceil \frac{N_{\mathrm{MPDU}} + 72}{k} \right\rceil = \frac{N_{\mathrm{T}}}{n}. \tag{4.6}$$

Relating N_{CW} to N_{T} will help us derive the expressions in Section 4.2.2.

4.1.2 Modulation, Waveform, and Receiver

On-off modulation is a combination of M-ary waveform coding and on-off keying. With the on-off modulation, K bits from an alphabet size of $M = 2^K$ are grouped, $(b_0, b_1, \cdots, b_{K-1})$, and passed through a symbol mapper of rate $1/2$ such that an output sequence of $2K$ bits, $(d_0, d_1, \cdots, d_{2K-1})$, is obtained that has the same alphabet size. In [20], $K = 1$ is considered as the default mode with an optional mode of $K = 4$. For example, the input bit 0 is mapped to [1 0], whereas 1 is mapped to [0 1]. Note that the performance of the on-off modulation for $K = 1$ closely follows the one for binary pulse position modulation [20]. After processing by the pulse shaping filter, the mth output IR-UWB symbol can be expressed as

$$x_m(t) = \sum_{n=0}^{2K-1} d_n^{(m)} w_{2Km+n}(t - n(T_{\mathrm{sym}}/2) - mKT_{\mathrm{sym}} - h_{2Km+n}T_w), \tag{4.7}$$

where $d_n^{(m)}$ is the nth codeword component of the mth symbol, T_{sym} is the symbol time, and $\{h_{2Km+n}\}$ is the time-hopping sequence. The symbol time T_{sym} has N_w pulse waveform positions each with a duration of T_w, $T_{\text{sym}} = N_w T_w$. The symbol duration is divided into two intervals of duration $T_{\text{sym}}/2$ in order to enable on-off modulation. The duty cycle T_w/T_{sym} is fixed at $1/32 = 3.125\%$ in [20] to ensure low power consumption. The pulse waveform $w_n(t)$ is given by

$$w_n(t) = \sum_{i=0}^{N_{\text{cpb}}-1} (1 - 2s_i)p(t - iT_p), \tag{4.8}$$

where $p(t)$ denotes a single pulse of duration T_p [20]. The sequence $\{s_i\}$ denotes the scrambling sequence that helps reduce the spectral lines due to same polarity pulses [20], [64]. The integer N_{cpb} defines the number of pulses per burst and $N_{\text{cpb}} \geq 1$. In the single pulse case, $N_{\text{cpb}} = 1$, whereas $N_{\text{cpb}} \in \{2,4,8,16,32\}$ for the burst pulse option. Note that the processing gain of an IR-UWB system is $N_{\text{cpb}} N_w$ [64]. Since N_{w} is fixed by the standard , the processing gain can be varied by changing N_{cpb}.

Table 4-2 presents the timing parameters and data rates for different transmission modes for on-off modulation. The pulses are generated at a frequency of 499.2 MHz and T_p is 2.0032 nsec. The symbol is encoded with a BCH code of (63,51). An uncoded symbol rate, $R_b = 1/T_{\text{sym}}$, is multiplied with the FEC rate to obtain the coded symbol rate. Hence, N_{cpb} is used to balance the data rate and processing gain trade-off.

A non-coherent detector is considered and equally likely input bits are assumed. Each pulse has an energy of $\varepsilon_p = \varepsilon_b/N_{\text{cpb}}$. The bit error probability is given by [26], [65]

$$P_b = Q\left(\sqrt{\frac{1}{2} \cdot \frac{(h\varepsilon_b/N_0)^2}{h\varepsilon_b/N_0 + N_{\text{cpb}} T_{\text{int}} W_{\text{rx}}}}\right), \tag{4.9}$$

where h is the channel coefficient, T_{int} is the integration interval per pulse, W_{rx} is the equivalent noise bandwidth of the receiver front end, and ε_p/N_0 is the integrated signal-to-noise ratio per bit. In Section 4.2.4, we take the integration time as the pulse duration, i.e., $T_{\text{int}} = N_{\text{cpb}}T_p$, and assume that the receiver and transmitter are fully synchronized.

4.1.3 Error Correction

In Section 4.1.1, we discussed the structure of an UWB frame that consists of SHR, PHR, and PSDU, and in Section 4.1.2, the bit error probability is presented for a non-coherent ED receiver. In what follows, we discuss the error correcting capabilities of each frame type.

The SHR frame is correctly received at the receiver if both the preamble and the SFD transmissions are successful, which can be mathematically expressed as

$$P_{\text{SHR}} = P_{\text{SFD}}(1 - (1 - P_{\text{Kasami}})^4), \tag{4.10}$$

where P_{SFD} and P_{Kasami} are the probabilities of correctly decoding the SFD and Kasami sequence, respectively. Since there are four Kasami sequences in the preamble, we have $(1 - P_{\text{Kasami}})^4$ in (4.10). The probability of successful delivery of a 63-bit Kasami sequence can be expressed as [27]

$$P_{\text{Kasami}} = \sum_{i=0}^{\rho} \binom{63}{i} (P_b)^i (1 - P_b)^{63-i}, \tag{4.11}$$

where the operator $\binom{a}{b}$ represents the binomial coefficient and ρ is an implementation-dependent sensitivity margin and it is taken as $\rho = 6$ as in [27]. Since the SFD is the ones complement of a Kasami sequence, we have $P_{\text{SFD}} = P_{\text{Kasami}}$.

The BCH decoder can recover up to t_{ECC} bit errors for a BCH$(n, k; t)$ code. Then, for the PHR frame, the probability of successful reception of a codeword is

$$P_{\text{PHR}} = \sum_{i=0}^{t} \binom{N_{\text{PHR}}}{i} (P_b)^i (1 - P_b)^{N_{\text{PHR}}-i}, \tag{4.12}$$

where $N_{\mathrm{PHR}} = 40$ bits is the number of bits in PHR frame, and P_b and t_{ECC} are given in (4.9) and Table 4-1, respectively.

The PSDU frame consists of N_{CW} codewords. The probability of successful reception of PSDU frame is if all the codewords are received successfully, that is

$$P_{\mathrm{PSDU}} = (P_{\mathrm{CW}})^{N\mathrm{CW}} = (P_{\mathrm{CW}})^{\frac{N_{\mathrm{T}}}{n}}, \tag{4.13}$$

where P_{CW} is the probability successful reception of a codeword that can be expressed as

$$P_{\mathrm{CW}} = \sum_{i=0}^{t} \binom{n}{i} (P_b)^i (1 - P_b)^{n-i}, \tag{4.14}$$

The probability of successful delivery is when the SHR, PHR, and PSDU frames are successfully received, that is

$$P_{\mathrm{PPDU}} = P_{\mathrm{SHR}} P_{\mathrm{PHR}} P_{\mathrm{PSDU}} = P_{\mathrm{SHR}} P_{\mathrm{PHR}} (P_{\mathrm{CW}})^{\frac{N_{\mathrm{T}}}{n}}, \tag{4.15}$$

where P_{SHR}, P_{PHR}, and P_{PSDU} are the successful delivery probabilities of the each frame type, respectively. For the default mode, $k = 51$ as shown in Table 4-2. On one hand, frame error probability increases as N_{T} increases, while, on the other hand, a short N_{T} will result in system inefficiency due to high packet overhead.

4.2 CLOEE - Cross-layer Optimization of Energy Efficiency

4.2.1 Energy Consumption Model

There have been several models in the literature characterizing the energy consumption of IR-UWB radios, e.g., [26], [27], [66], [67]. Among these studies, we use the model in [60] as it provides a general model to accommodate the coherent and non-coherent detectors, hard and soft decision demodulators, and different modulation types. Using this model, the energy required to transmit and receive a payload bit is given by

$$\varepsilon_B = \frac{\varepsilon_{\mathrm{FB}}^{\mathrm{Tx}} + \varepsilon_{\mathrm{FB}}^{\mathrm{Rx}}}{N_T}, \tag{4.16}$$

where $\varepsilon_{\mathrm{FB}}^{\mathrm{Tx}}$ and $\varepsilon_{\mathrm{FB}}^{\mathrm{Rx}}$ represent the energy consumed at the transmitter and receiver for the PSDU frame, respectively. These two terms can be expressed as

$$\varepsilon_{\mathrm{FB}}^{\mathrm{Tx}} = \varepsilon_p N_{\mathrm{cpb}} N_T + P_{\mathrm{SYN}} T_{\mathrm{onL}}, \tag{4.17a}$$

$$\varepsilon_{\mathrm{FB}}^{\mathrm{Rx}} = (MP_{\mathrm{COR}} + \rho_c P_{\mathrm{ADC}} + P_{\mathrm{LNA}} + P_{\mathrm{VGA}} + \rho_c (P_{\mathrm{GEN}} + P_{\mathrm{SYN}})) T_{\mathrm{onL}}, \tag{4.17b}$$

where P_{SYN} is the power consumption of the clock generator and synchronizer at the transmitter and T_{onL} is the time duration to transmit N_T bits, $T_{\mathrm{onL}} = T_{\mathrm{sym}} N_T$. The terms P_{COR}, P_{ADC}, P_{LNA}, P_{VGA}, and P_{GEN}, respectively, represent the power consumption of the RAKE fingers of the receiver, the analog-to-digital converter (ADC), the low noise amplifier (LNA), the variable gain amplifier (VGA), and the pulse generator. The number of RAKE receiver fingers is denoted by M, the term $\rho_r = 1$ for coherent modulation, and $\rho_r = 0$ for non-coherent modulation, and the term $\rho_c = 1$ for soft decision, whereas $\rho_c = 0$ is for hard decision.

Similarly, the overhead energy consumption is defined as

$$\varepsilon_{\mathrm{OH}} = \varepsilon_{\mathrm{OH}}^{\mathrm{Tx}} + \varepsilon_{\mathrm{OH}}^{\mathrm{Rx}}, \tag{4.18}$$

where $\varepsilon_{\mathrm{OH}}^{\mathrm{Tx}}$ and $\varepsilon_{\mathrm{OH}}^{\mathrm{Rx}}$ denote the energy to transmit and receive the overhead, respectively, and these are given by

$$\varepsilon_{\mathrm{OH}}^{\mathrm{Tx}} = \left(N_{\mathrm{cpb}}^{\mathrm{SHR}} N_{\mathrm{SHR}} + N_{\mathrm{cpb}}^{\mathrm{PHR}} N_{\mathrm{PHR}}\right)\varepsilon_p + P_{\mathrm{SYN}}(T_{\mathrm{SHR}} + T_{\mathrm{PHR}}), \tag{4.19}$$

$$\begin{aligned} \varepsilon_{\mathrm{OH}}^{\mathrm{Rx}} = {} & (MP_{\mathrm{COR}} + \rho_c P_{\mathrm{ADC}} + P_{\mathrm{LNA}} + P_{\mathrm{VGA}} \\ & + \rho_r (P_{\mathrm{GEN}} + P_{\mathrm{SYN}})\big)(T_{\mathrm{SHR}} + T_{\mathrm{PHR}}), \end{aligned} \tag{4.20}$$

where $N_{\mathrm{cpb}}^{\mathrm{SHR}} = 4$, $N_{\mathrm{cpb}}^{\mathrm{PHR}} = 32$, $N_{\mathrm{SHR}} = 63 \cdot 5 = 315$, and T_{SHR} and T_{PHR} are defined as in Section 4.1.1.

Finally, the startup energy is

$$\varepsilon_{\mathrm{ST}} = \varepsilon_{\mathrm{ST}}^{\mathrm{Tx}} + \varepsilon_{\mathrm{ST}}^{\mathrm{Rx}} = 2P_{\mathrm{SYN}}T_{\mathrm{ST}}, \tag{4.21}$$

where T_{ST} is the time duration for the start-up of the devices.

4.2.2 Problem Formulation

Consider a hub and N_{S} nodes, each requesting R_0 bits per second, in a one-hop star topology. The following are defined to aid the problem formulation:

Definition 1:

A function f is strictly quasiconcave if its domain $\mathcal{D}$ is convex, and for any $x, y \in \mathcal{D}$ with $f(x) \neq f(y)$, the following is true for all $\lambda \in (0,1)$ [68]

$$f(\lambda x + (1-\lambda)y) > \min\{f(x), f(y)\}, \tag{4.22}$$

Definition 2:

The energy efficiency is defined as the ratio of the total number of successfully received bits to the total energy consumed at the transmitter and receiver. It can be expressed in the units of bits/Joule as

$$\eta\left(N_{\mathrm{T}}, N_{\mathrm{cpb}}\right) = \frac{N_{\mathrm{T}}P_{\mathrm{SHR}}P_{\mathrm{PHR}}(P_{\mathrm{CW}})^{\frac{N_{\mathrm{T}}}{n}}}{N_{\mathrm{T}} \cdot \varepsilon_{\mathrm{B}} + \varepsilon_{\mathrm{OH}} + \varepsilon_{\mathrm{ST}}}, \tag{4.23}$$

Lemma 1:

The optimal PSDU frame size that maximizes (4.23) can be expressed as

$$N_{\mathrm{T}}^{\mathrm{EE}} = \left[\sqrt{\frac{(\varepsilon_{\mathrm{OH}} + \varepsilon_{\mathrm{ST}})^2}{(2\varepsilon_{\mathrm{B}})^2} - \frac{n(\varepsilon_{\mathrm{OH}} + \varepsilon_{\mathrm{ST}})}{\varepsilon_{\mathrm{B}}\log(P_{\mathrm{CW}})}} - \frac{\varepsilon_{\mathrm{OH}} + \varepsilon_{\mathrm{ST}}}{2\varepsilon_{\mathrm{B}}}\right], \tag{4.24}$$

Proof:

It follows that when we take the derivative of (4.23) with respect to N_{T} and rearrange the terms, it is straightforward to obtain (4.24).0

Theorem 1:

Energy efficiency is strictly quasiconcave in N_{T}.

Proof:

The second-order condition for a strictly quasiconcave function is that the second derivative needs to be non-positive at any point with zero slope [69]. Then, to prove the quasiconcavity of η, we need to show that

$$\nabla_{N_\mathrm{T}}\eta = 0 \Rightarrow \nabla_{N_\mathrm{T}^2}\eta < 0. \tag{4.25}$$

Let us define

$$A = P_\mathrm{SHR}P_\mathrm{PHR}(P_\mathrm{CW})^{\frac{N_\mathrm{T}}{n}}, \tag{4.26}$$

$$\varepsilon_1 = \varepsilon_\mathrm{OH} + \varepsilon_\mathrm{ST}, \tag{4.27}$$

$$\gamma = \varepsilon_\mathrm{B}N_\mathrm{T} + \varepsilon_1. \tag{4.28}$$

Then, the gradient of η is given by

$$\frac{\partial\eta}{\partial N_\mathrm{T}} = \frac{A\left(N_\mathrm{T}^2\frac{\varepsilon_\mathrm{B}\log(P_\mathrm{CW})}{n} + N_\mathrm{T}\frac{\varepsilon_1\log(P_\mathrm{CW})}{n} + \varepsilon_1\right)}{\gamma^2}. \tag{4.29}$$

Let us introduce

$$\beta = N_\mathrm{T}^2\frac{\varepsilon_\mathrm{B}\log(P_\mathrm{CW})}{n} + N_\mathrm{T}\frac{\varepsilon_1\log(P_\mathrm{CW})}{n} + \varepsilon_1. \tag{4.30}$$

Note that N_T^EE is the root of β, where the gradient becomes zero. The second derivative of η can be expressed as

$$\frac{\partial^2\eta}{\partial N_\mathrm{T}^2} = \frac{A\frac{\log(P_\mathrm{CW})}{n}(\beta + 2N_\mathrm{T}\varepsilon_\mathrm{B} + \varepsilon_1)}{\gamma^2} - \frac{A\beta(2\varepsilon_\mathrm{B})}{\gamma^3}. \tag{4.31}$$

To prove that (4.25) holds true, we check the sign of $\frac{\partial^2\eta}{\partial N_\mathrm{T}^2}$ when the gradient is zero. Since $\log(P_\mathrm{CW}) \leq 0$ for $0 \leq P_\mathrm{CW} \leq 1$ and $\beta = 0$ at N_T^EE, we have $\frac{\partial^2\eta}{\partial N_\mathrm{T}^2} \leq 0$ which satisfies (4.25). Thus, we prove that η is strictly quasiconcave in N_T.

Theorem 2:

If a function η is a strictly quasiconcave, then a local optimal solution is also a global maximum solution.

Proof:

See the proof of Theorem 3.5.6 in [68].

Definition 3:

The network throughput is defined as the ratio of the total number bits that are successfully received at receiver to the duration of a frame, and can be defined in the units of bits/sec as

$$R\left(N_{\mathrm{T}}, N_{\mathrm{cpb}}\right) = \frac{N_{\mathrm{T}} P_{\mathrm{SHR}} P_{\mathrm{PHR}} (P_{\mathrm{CW}})^{\frac{N_{\mathrm{T}}}{n}}}{T_{\mathrm{SHR}} + T_{\mathrm{PHR}} + N_{\mathrm{T}} T_{\mathrm{sym}}}. \tag{4.32}$$

where the terms P_{SHR} and P_{PHR} are functions of N_{cpb} through P_b. The probability P_{CW} is a function of both N_{T} and N_{cpb}.

Lemma 2:

For a given N_{cpb}, the optimal PSDU frame size that maximizes the throughput, $R(N_{\mathrm{T}}, N_{\mathrm{cpb}})$, is given by

$$N_{\mathrm{T}}^{\mathrm{THR}} = \left\lfloor \sqrt{\frac{(T_{\mathrm{SHR}} + T_{\mathrm{PHR}})^2}{(2T_{\mathrm{sym}})^2} - \frac{n(T_{\mathrm{SHR}} + T_{\mathrm{PHR}})}{T_{\mathrm{sym}} \log(P_{\mathrm{CW}})}} - \frac{T_{\mathrm{SHR}} + T_{\mathrm{PHR}}}{2T_{\mathrm{sym}}} \right\rfloor, \tag{4.33}$$

Proof:

When the derivative of (4.32) is taken with respect to N_{T}, equate it to zero, and rearrange the terms, we obtain the expression in (4.33) for the optimal PSDU frame size.

Our objective is to maximize the network energy efficiency subject to the minimum rate constraint, which is given by

$$\text{(P)} \quad \max \quad \frac{f(N_{\mathrm{T}}, N_{\mathrm{cpb}})}{g(N_{\mathrm{T}}, N_{\mathrm{cpb}})} = \frac{N_{\mathrm{T}} P_{\mathrm{SHR}} P_{\mathrm{PHR}} (P_{\mathrm{CW}})^{\frac{N_{\mathrm{T}}}{n}}}{(N_{\mathrm{T}} \cdot \varepsilon_{\mathrm{B}} + \varepsilon_{\mathrm{OH}} + \varepsilon_{\mathrm{ST}})}, \tag{4.34a}$$

$$\text{s.t.} \quad \frac{N_{\mathrm{T}} P_{\mathrm{SHR}} P_{\mathrm{PHR}} (P_{\mathrm{CW}})^{\frac{N_{\mathrm{T}}}{n}}}{T_{\mathrm{SHR}} + T_{\mathrm{PHR}} + N_{\mathrm{T}} T_{\mathrm{sym}}} \geq R_0 N_{\mathrm{S}}, \tag{4.34b}$$

The Lagrangian of (4.34) can be expressed as

$$\mathcal{L}(N_{\mathrm{T}}, N_{\mathrm{cpb}}, \lambda) = \quad \eta(N_{\mathrm{T}}, N_{\mathrm{cpb}}) + \lambda(R(N_{\mathrm{T}}, N_{\mathrm{cpb}}) - R_0 N_{\mathrm{S}}), \tag{4.35}$$

where λ is the Lagrangian variable associated with the minimum rate constraints.

Lemma 3:

The optimal solution, $(N_{\mathrm{T}}^*, N_{\mathrm{cpb}}^*)$, and the corresponding Lagrangian dual variable λ^* must satisfy the following Karush-Kuhn-Tucker (KKT) conditions

$$\nabla_{N_{\mathrm{T}}} \eta(N_{\mathrm{T}}^*, N_{\mathrm{cpb}}^*) + \lambda^* \nabla_{N_{\mathrm{T}}} R(N_{\mathrm{T}}^*, N_{\mathrm{cpb}}^*) = 0, \tag{4.36a}$$

$$\nabla_{N_{\mathrm{cpb}}} \eta(N_{\mathrm{T}}^*, N_{\mathrm{cpb}}^*) + \lambda^* \nabla_{N_{\mathrm{cpb}}} R(N_{\mathrm{T}}^*, N_{\mathrm{cpb}}^*) = 0, \tag{4.36b}$$

$$\lambda^* \left[R(N_{\mathrm{T}}^*, N_{\mathrm{cpb}}^*) - R_0 N_{\mathrm{S}}\right] = 0, \text{and } \lambda^* \geq 0, \tag{4.36c}$$

where ∇_x denotes the gradient with respect to x. Any point that satisfies (4.36a)-(4.36b) is called a stationary point. Complementary slackness and dual feasibility conditions are expressed in (4.36c). These conditions suggest that if the minimum rate constraint is satisfied, $R(N_{\mathrm{T}}, N_{\mathrm{cpb}}) > R_0 N_{\mathrm{S}}$, then $\lambda^* = 0$. Otherwise, we have $\lambda^* > 0$.

The problem (4.34) is a single-ratio fractional program and it can be solved using the dual fractional program [70]. Let $h(N_{\mathrm{T}}, N_{\mathrm{cpb}})$ denote the constraint of (4.34) such as

$$h(N_{\mathrm{T}}, N_{\mathrm{cpb}}) = R_0 N_{\mathrm{S}} - \frac{N_{\mathrm{T}} P_{\mathrm{SHR}} P_{\mathrm{PHR}} (P_{\mathrm{CW}})^{\frac{N_{\mathrm{T}}}{n}}}{T_{\mathrm{SHR}} + T_{\mathrm{PHR}} + T_{\mathrm{sym}} N_{\mathrm{T}}}, \tag{4.37}$$

Then, the dual fractional program can be expressed as

$$\text{(D)} \min_{\lambda \geq 0} \left[\max_{N_{\mathrm{T}}} \frac{f(N_{\mathrm{T}}, N_{\mathrm{cpb}}) - \lambda h(N_{\mathrm{T}}, N_{\mathrm{cpb}})}{g(N_{\mathrm{T}}, N_{\mathrm{cpb}})} \right], \tag{4.38}$$

Problem (4.38) can be solved iteratively. We first fix λ and use any line search method to solve (4.38), and we obtain N_{T}^{*}. Next, we update the dual variable λ as

$$\lambda_{l+1} = \left[\lambda_l - \alpha_l\left(R\left(N_{\mathrm{T}}^{*}, N_{\mathrm{cpb}}\right) - R_0 N_{\mathrm{S}}\right)\right]^{+}, \tag{4.39}$$

where the operator $[x]^{+}$ denotes $\max(x, 0)$ and α_l is the step size of the lth iteration. We keep iterating until the stopping condition is satisfied. The algorithm terminates when the relative change in N_{T} between two iterations is less than some tolerance, i.e, $|N_{\mathrm{T}}(l+1) - N_{\mathrm{T}}(l)|/N_{\mathrm{T}}(l) \leq \Delta$ [68].

4.2.3 Algorithm

Algorithm 1. CLOEE – Cross-Layer Optimization for Energy Efficiency for IEEE 802.15.6 IR-UWB

function CLOEE($\varepsilon_{\mathrm{B}}, \varepsilon_{\mathrm{OH}}, \varepsilon_{\mathrm{ST}}, T_{\mathrm{SHR}}, T_{\mathrm{PHR}}, T_{\mathrm{p}}, R_0, N_{\mathrm{S}}$)
  Set an all-zeros vector $\mathbf{N}_{\mathrm{T}}$ of size $\left|\{N_{\mathrm{cpb}}\}\right|$ and $n \leftarrow 0$
  for $\mathbf{N}_{\mathrm{cpb}} = \{1,2,4,8,16,32\}$ **do**
    Set $l \leftarrow 0$ and solve (4.24) to obtain $N_{\mathrm{T}}(l)$
    Set $\lambda(l) \leftarrow \max\left(R_0 N_{\mathrm{S}} - R\left(N_{\mathrm{T}}(l), \mathbf{N}_{\mathrm{cpb}}(n)\right), 0\right)$
    if $R\left(N_{\mathrm{T}}(l), \mathbf{N}_{\mathrm{cpb}}(n)\right) \geq R_0 N_{\mathrm{S}}$ **then**
      $\mathbf{N}_{\mathrm{T}}(n) \leftarrow N_{\mathrm{T}}(l)$
    else
      if $R\left(N_{\mathrm{T}}^{\mathrm{THR}}(l), \mathbf{N}_{\mathrm{cpb}}(n)\right) > R_0 N_{\mathrm{S}}$ **then**
        repeat
          Solve (4.38) to obtain $N_{\mathrm{T}}(l)$
          Update $\lambda(l+1)$ using (4.39)
          Set $l \leftarrow l + 1$
        until stopping criteria is satisfied
        $\mathbf{N}_{\mathrm{T}}(n) \leftarrow N_{\mathrm{T}}(l)$
      else
        $\mathbf{N}_{\mathrm{T}}(n) \leftarrow N_{\mathrm{T}}^{\mathrm{THR}}$
      end if
    end if
    $n \leftarrow n + 1$
  end for
  $\left(N_{\mathrm{T}}^{*}, N_{\mathrm{cpb}}^{*}\right) \leftarrow \arg\max_{(N_{\mathrm{T}}, N_{\mathrm{cpb}})} \eta(\mathbf{N}_{\mathrm{T}}, \mathbf{N}_{\mathrm{cpb}})$
end function

The proposed algorithm, CLOEE, is summarized in Algorithm 1. We identify three scenarios. First, if the throughput at $N_{\mathrm{T}}^{\mathrm{EE}}$ satisfies the rate constraint, i.e., $R(N_{\mathrm{T}}^{\mathrm{EE}}, N_{\mathrm{T}}^{\mathrm{cpb}}) > R_0 N_{\mathrm{S}}$, then $N_{\mathrm{T}}^{\mathrm{EE}}$ is obtained in a single-step using (4.24). This occurs often for short to medium link distances. Second, if the throughput at $N_{\mathrm{T}}^{\mathrm{EE}}$ does not satisfy the rate constraint, but $N_{\mathrm{T}}^{\mathrm{THR}}$ satisfies it, i.e., $R(N_{\mathrm{T}}^{\mathrm{EE}}) < R_0 N_{\mathrm{S}}$ and $R(N_{\mathrm{T}}^{\mathrm{THR}}) > R_0 N_{\mathrm{S}}$, then we solve (4.38). In the link adaptation, this typically occurs during the mode transitions. Lastly, for long link distances, when there is no N_{T} that satisfies the rate constraint at N_{cpb}, we assign $N_{\mathrm{T}}^{\mathrm{THR}}$ to N_{T}.

4.2.4 Simulation Results

Figs. 4.2(a)-(b) illustrate the dependence of the energy efficiency and throughput on the PSDU frame size. The points $N_{\mathrm{T}}^{\mathrm{EE}}$, $N_{\mathrm{T}}^{\mathrm{THR}}$, and N_{T}^{*} are also shown. The results are given for a link distance of 8.4 meters, where error probability is high. Rates with $N_{\mathrm{cpb}} \in \{1,2,4\}$ perform very poorly, whereas the higher orders achieve better performance. Note that at a shorter distance, the order of these curves can be different and the performance depends on the link distance, see Figs. 4.3(c)-(d).

Then we evaluate the performance of CLOEE. For comparison, we also simulate numerous static strategies and an exhaustive search approach. The performance results presented in this section are obtained by using MATLAB. The channel characteristics of WBANs vary with the patient's attributes (e.g., gender, weight, fat), radiation pattern that shapes the specific absorption rate (SAR), and patient motions. In this section, the channel model in [71] is used to characterize the propagation environment in the 3.1-10.6 GHz band, for which the path loss is [71] $L(d) = a \cdot \log_{10}(d) + b + \chi$, where a and b are constants, d is the distance in millimeters, and χ is a Gaussian distributed random variable with a zero mean and a variance σ^2. Typical values for a hospital room are $a = 19.2$, $b = 3.38$, and $\sigma = 4.40$ [71]. The noise spectral density is taken as

-174 dBm/Hz, W_{rx} as 499.2 MHz, noise figure as 10 dB, and implementation margin as 5 dB [20]. A non-coherent receiver and hard decision combining is considered, $\rho_r = 0$, and $\rho_c = 0$. For the energy consumption model, we have $\varepsilon_p = 20$ pJ, $P_{\mathrm{COR}} = 10.08$ mW, $P_{\mathrm{ADC}} = 2.2$ mW, $P_{\mathrm{LNA}} = 9.4$ mW, $P_{\mathrm{VGA}} = 22$ mW, $P_{\mathrm{SYN}} = 30.6$ mW, $P_{\mathrm{GEN}} = 2.8$ mW, and $T_{\mathrm{ST}} = 400$ μs [66].

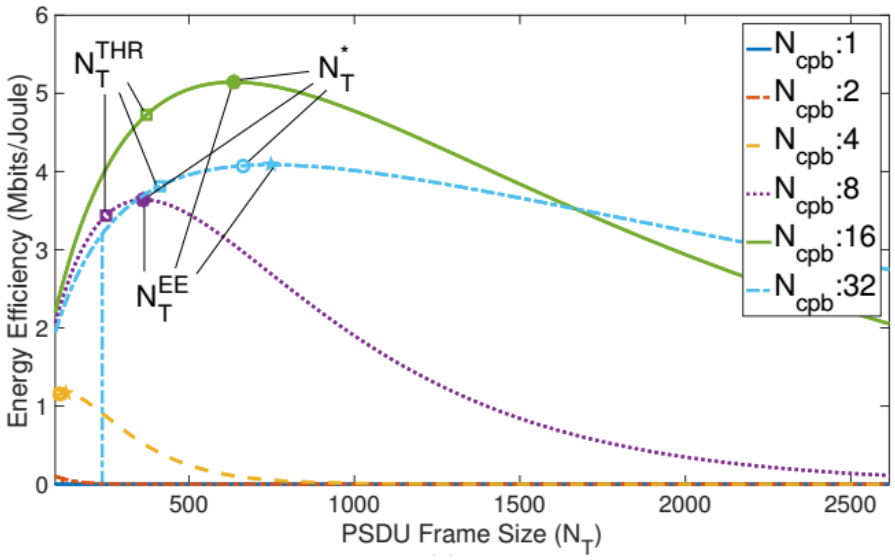

(a)

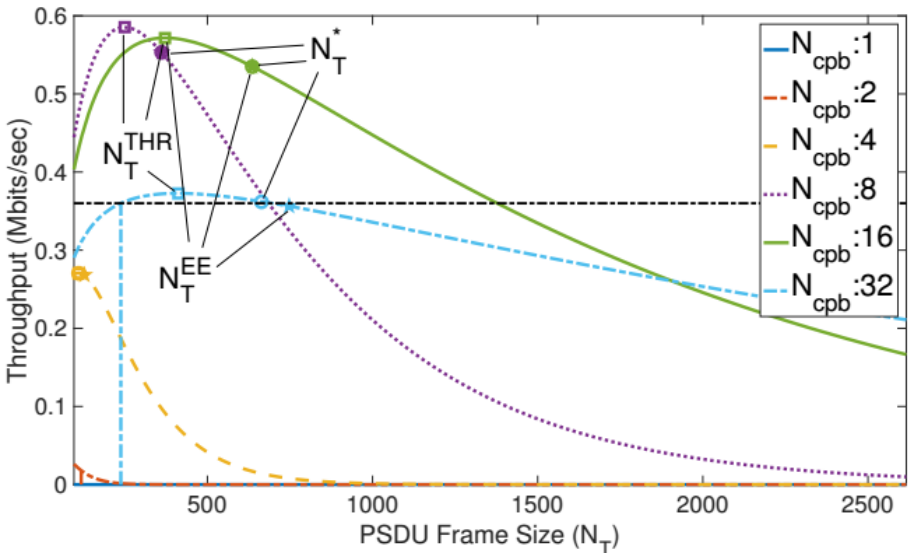

(b)

Figure 4.2. Energy efficiency and throughput versus the PSDU frame size at 8.4 meters for $R_0 = 15$ kbits/sec and $N_S = 24$ nodes.

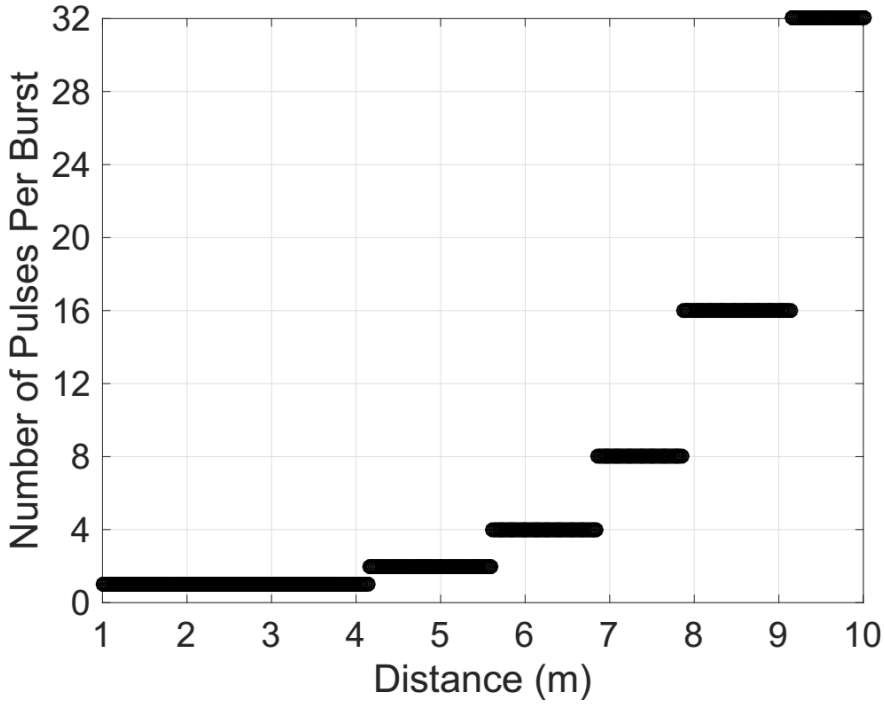

(a)

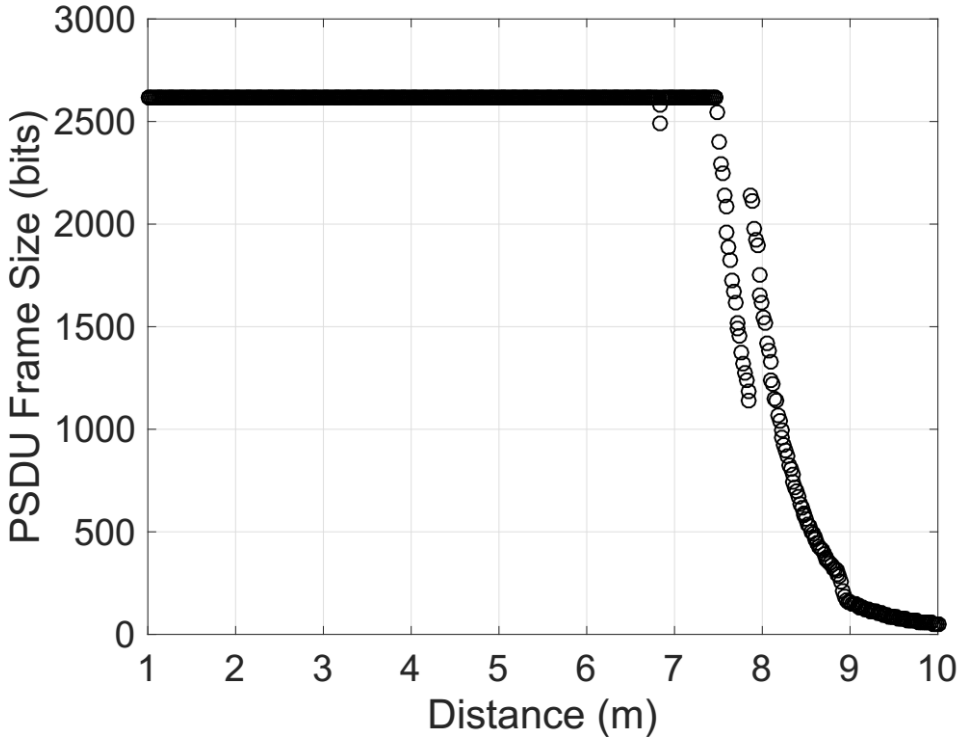

(b)

Figure 4.3. Link adaptation results for maximizing the energy efficiency.

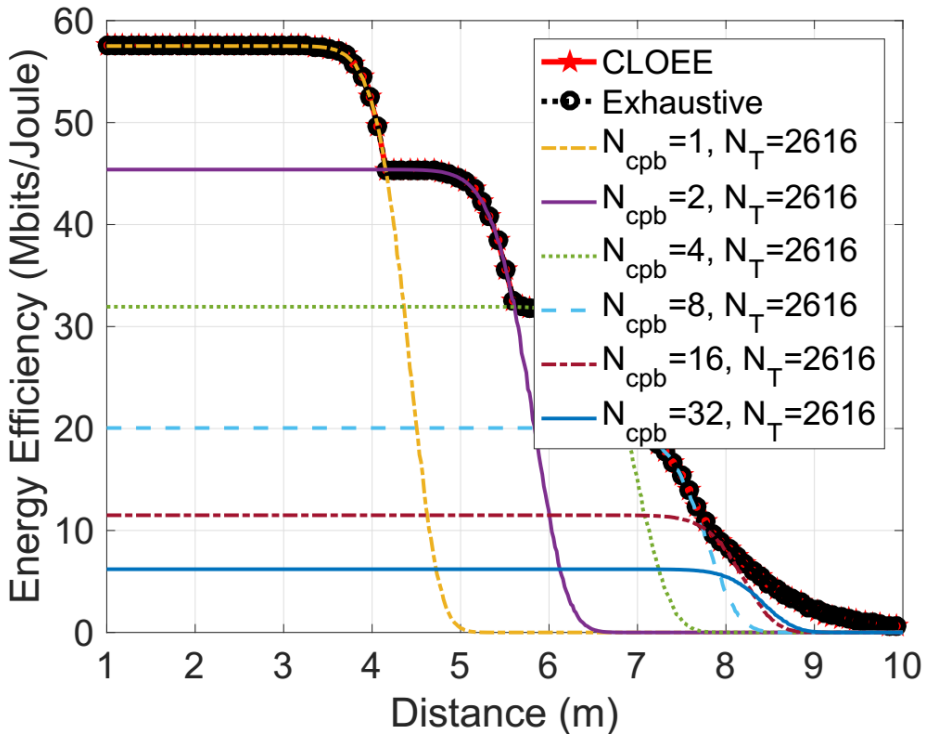

(c)

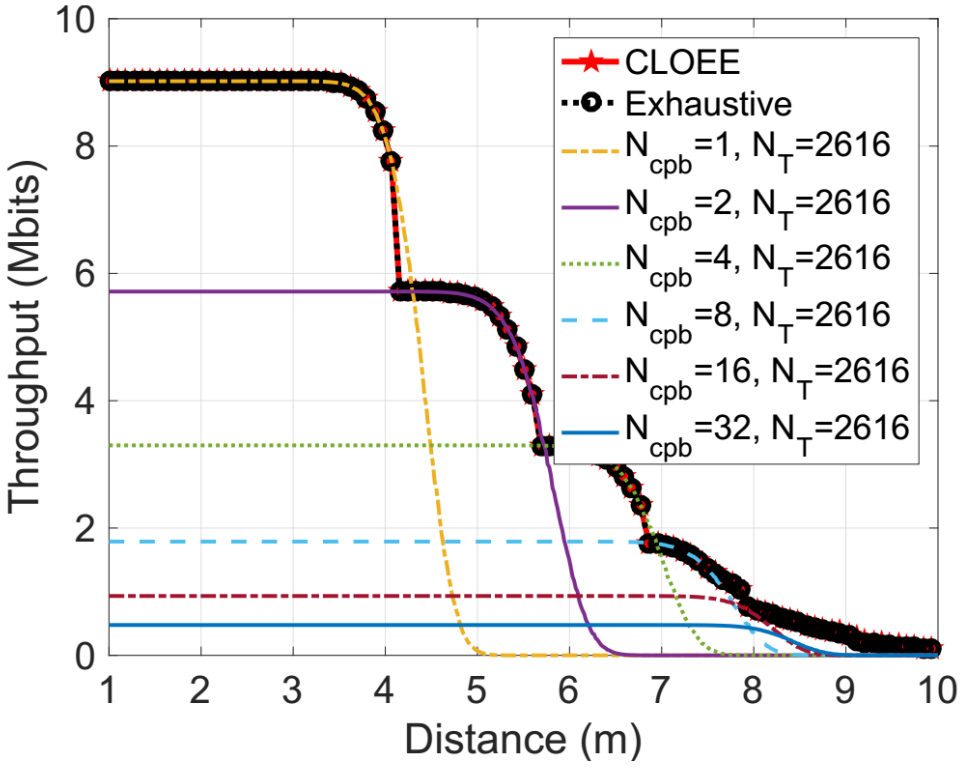

(d)

Figure 4.3. (Continued)

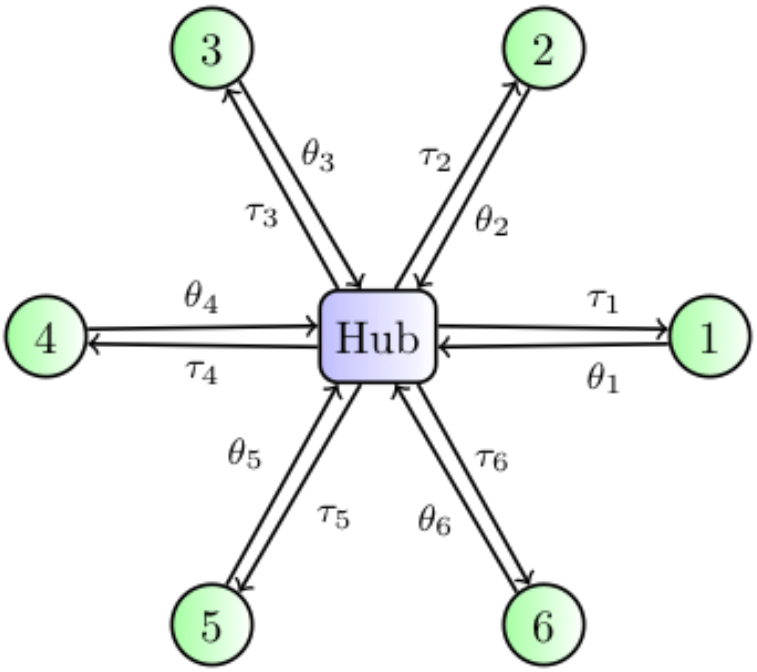

Figure 4.4. One-hop star network topology for WBANs consisting of multiple nodes and a hub. Nodes send their application requirements and the hub sends back their channel access probabilities.

Link distance and channel characteristics strongly influence the optimal PHY and MAC layer parameters for link adaptation. Figs. 4.3(a)-(d) depict the link adaptation optimization as a function of the PSDU frame size and the number of pulses per burst when the link distance varies from one to ten meters. Figs. 4.3(a)-(b) present the corresponding values of N_{T} and N_{cpb} obtained using CLOEE. It can be observed that for distances up to 7.5 meters, longer frame sizes and higher data rates (few pulses per burst) provide the highest energy efficiency. For longer link distances, due to the lower SNR and thereby higher error probability, shorter frames sizes and more pulses per burst are preferred. For example, PSDU frame size decreases steeply after 7.5 meters and the optimal number of pulses per burst soars to its maximum number of 32. In Figs. 4.3(c)-(d), the performance of five static strategies, exhaustive search, and CLOEE are evaluated. The performance of CLOEE and exhaustive search overlap which demonstrates the advantage of

CLOEE since its computational complexity is much smaller. As expected, CLOEE outperforms the static strategies in various performance metrics. For instance, the performance of $(N_{\mathrm{cpb}}, N_{\mathrm{T}}) = (1,2616)$ and CLOEE are similar for short distances up to 4 meters. Beyond this point, the performance of $(N_{\mathrm{cpb}}, N_{\mathrm{T}}) = (2,2616)$ decays quickly, whereas CLOEE satisfies the QoS constraints up to 8.8 meters, indicating its extended transmission range about a factor of two. Also, $(N_{\mathrm{cpb}}, N_{\mathrm{T}}) = (32,2616)$ provides a very robust transmission, but it is highly inefficient for short distances since it achieves only 6.2 Mbits/Joule, whereas CLOEE offers 57.5 Mbits/Joule at the same distance, indicating close to an order of magnitude gain.

4.3 EECAP - Energy Efficiency Optimization of Channel Access Probability

4.3.1 Network Topology and Channel Access Probabilities

As shown in Fig. 4.4, consider a one-hop star topology for WBAN, which has one hub and N_s nodes. For node i, $i = 1,2,\ldots,N_s$, the channel access probability, PSDU frame body size, distance from the hub and its minimum rate constraint are denoted as τ_i, N_i^T, d_i, and R_i^{min}, respectively. The scenario we investigate is that every node contends for the medium and the hub works as a controller to determine the optimal access probability of the nodes. Fig. 4.4 depicts an example scenario where multiple nodes report their requirements, denoted by θ_i, and the hub sends back their channel access probabilities that solve the maximization problem. The node requirements can be multi-bit signals, and are application and node specific addressing a variety of constraints such as the rate, delay, power, reliability, QoS, and security levels. In this paper, we only focus on the minimum rate constraint for simplicity, i.e., $\theta_i = R_i^{min}$, although the proposed framework can address multiple constraints at the same time.

Similar to the channel states described in [72] and [73] for IEEE 802.11 networks, we define three channel states for the one-hop star WBAN:

- *Successful transmission:* one of the nodes gets the channel and successfully transmits its packets;
- *Collision:* more than one user transmit packets and they collide;
- *Idle channel:* none of the nodes transmits.

For node i, the probability of successful transmission is

$$P_i^S = \tau_i \prod_{j \neq i} (1 - \tau_j) = \tau_i (1 - p_i), \tag{4.40}$$

where

$$p_i = 1 - \prod_{j \neq i} (1 - \tau_j), \tag{4.41}$$

is the collision probability experienced by node i because of other nodes [73]. Then the probability of successful transmission for all the nodes is the sum of each node's probability of success,

$$P^S = \sum_i P_i^S = \sum_i \tau_i (1 - p_i). \tag{4.42}$$

For the case of collision, the probability is given by,

$$P^C = 1 - P^S - P^I, \tag{4.43}$$

where P^I is the probability of an idle channel,

$$P^I = \prod_i (1 - \tau_i). \tag{4.44}$$

The probabilities in (4.42)- (4.44) can be expressed by linear functions of τ_k, $k = 1,2,\ldots,N_s$, which are shown below:

$$P^S = x_k^S \tau_k + y_k^S, \tag{4.45}$$

$$P^C = x_k^C \tau_k + y_k^C, \tag{4.46}$$

$$P^I = x_k^I \tau_k + y_k^I, \tag{4.47}$$

where

$$x_k^C = \sum_{i \neq k} \tau_i \frac{1 - p_i}{1 - \tau_k}, \tag{4.48}$$

$$x_k^S = 1 - p_k - x_k^C, \tag{4.49}$$

$$x_k^I = p_k - 1, \tag{4.50}$$

and

$$y_k^S = x_k^C, \tag{4.51}$$

$$y_k^C = p_k - x_k^C, \tag{4.52}$$

$$y_k^I = 1 - p_k, \tag{4.53}$$

These terms will help us obtain closed-form expressions in Section 4.3.4.

4.3.2 Energy Consumption Model

We use the same energy consumption model as in Section 4.2.1, but we further define the energy consumptions for each of the three channel states described in Section 4.3.1. For successful transmission, the energy consumed is

$$\varepsilon_i^S = \varepsilon_B N_i^T + \varepsilon_{OH} + \varepsilon_{ST}, \tag{4.54}$$

where ε_B stands for the energy required to transmit and receive a payload bit, ε_{OH} is the energy consumed for the transmission and reception of the overhead, ε_{ST} means the startup energy. The PSDU frame size for node i is denoted as N_i^T. When collision happens, the energy is given by

$$\varepsilon_i^C = \varepsilon_B^{Tx} N_i^T + \varepsilon_{OH}^{Tx} + \varepsilon_{ST}^{Tx}, \tag{4.55}$$

where ε_B^{Tx}, ε_{OH}^{Tx} and ε_{ST}^{Tx} are defined similarly as the energy required for payload bit, overhead and startup in transmission only. When the channel is idle, we assume that no energy is consumed, i.e., $\varepsilon^I = 0$. Our model can be easily adapted to new cases when we consider the energy consumed by the circuits during the idle channel.

The details about the energy consumption model for different detector, modulation, and demodulation types can be found in [66].

4.3.3 Time Duration Model

The time duration will also be different for each of the three channel states. If node i successfully transmits its packet and receives the acknowledgement packet from the hub, the time duration is given by

$$T_i^S = T_i^{PPDU} + T_{ACK} + 2T_{pSIFS} + 2\sigma_i, \tag{4.56}$$

where $T_i^{PPDU} = T_{SHR} + T_{PHR} + N_{Ti}T_{sym}$ is node i's PPDU time duration, which has been defined in Section 4.1.2. $T_{ACK} = T_{SHR} + T_{PHR} + N_T^{min}T_{sym}$ is the time duration of the acknowledgement packet that sent from the hub. We assume it uses the minimum frame length, $N_T^{min} = 126$ bits [20]. The time period of the short interframe spacing is $T_{pSIFS} = 75\ \mu s$ [20]. The propagation time is denoted by σ_i. The time spent in the scenario of collision is given by

$$T_i^C = T_i^{PPDU} + T_{pSIFS} + \sigma_i. \tag{4.57}$$

The time period in an idle channel is given by the CSMA slot time period. From [20], we have $T^I = 292\ \mu s$ and it is used in the expression for the throughput.

4.3.4 Problem Formulation

The energy efficiency and throughput which consider the channel access probabilities are defined to aid the problem formulation:

Definition 4:

The energy efficiency for node i is defined as the successfully transmitted payload information divided by the average energy consumption, which can be expressed as

$$\eta_i = \frac{N_i^T P_i^S P_i^{SHR} P_i^{PHR} (P_i^{CW})^{\frac{N_i^T}{n}}}{P^S \varepsilon_i^S + P^C \varepsilon_i^C + P^I \varepsilon_i^I}. \tag{4.58}$$

***Definition 5*:**

Node i's throughput is defined as the number of successfully transmitted payload bits divided by the average time duration, which is given by

$$R_i = \frac{N_i^T P_i^S P_i^{SHR} P_i^{PHR} (P_i^{CW})^{\frac{N_i^T}{n}}}{P^S T_i^S + P^C T_i^C + P^I T_i^I}. \tag{4.59}$$

Lemma 5:

The derivative of the node k's throughput with respect to τ_k is a monotonically increasing function, i.e., $\partial R_k / \partial \tau_k \geq 0$.

Proof:

The derivative of R_k respect to τ_k is,

$$\frac{\partial R_k}{\partial \tau_k} = \frac{\left[N_k^T (1 - p_k) P_k^{SHR} P_k^{PHR} (P_k^{CW})^{\frac{N_k^T}{n}} \right] YT}{(XT \cdot \tau_k + YT)^2}. \tag{4.60}$$

Since $T_k^S > T_k^C$ as in [74],

$$YT = y_k^S T_k^S + y_k^C T_k^C + y_k^I T^I = x_k^C T_k^S + (p_k - x_k^C) T_k^C + (1 - p_k) T^I \geq 0. \tag{4.61}$$

Therefore, $\partial R_k / \partial \tau_k \geq 0$.

Consequently, the minimum value of τ_k that satisfies the rate constraint can be obtained by letting $R_k = R_k^{min}$, then

$$(\tau_k^{min})^{THR} = \frac{R_k^{min} * YT}{N_k^T (1 - p_k) P_k^S P_k^{SHR} P_k^{PHR} (P_k^{CW})^{\frac{N_k^T}{n}} - R_k^{min} * XT}, \tag{4.62}$$

where

$$XT = x_k^S T_k^S + x_k^C T_k^C + x_k^I T_i^I, \tag{4.63}$$

and

$$YT = y_k^S T_k^S + y_k^C T_k^C + y_k^I T_i^I, \tag{4.64}$$

If $(\tau_k^{min})^{THR} \notin (0,1)$, there is no feasible solution for τ_k that satisfies the rate constraint.

Lemma 6:

If $P_k^{CW} \in (0,1)$ holds, then the optimal PSDU frame length for the node k's throughput is given by

$$(N_k^T)^{THR} = \left[-\frac{[n + \log(P_k^{CW})] * TO}{\log(P_k^{CW}) * TN} \right]_{N_T^{min}}^{N_T^{max}}, \tag{4.65}$$

where

$$TO = P^S\left(T_{SHR} + T_{PHR} + T_{ACK} + 2T_{pSIFS} + 2\sigma\right) + P^C(T_{SHR} + T_{PHR} + T_{pSIFS} + \sigma_k) + P^I T_k^I, \tag{4.66}$$

and

$$TN = (P^S + P^C)T_{sym}. \tag{4.67}$$

If $P_k^{CW} = 0$, then the throughput is always zero, $R_k = 0$. If $P_k^{CW} = 1$, then $(N_k^T)^{THR} = N_T^{max}$.

Our problem (EE) is to maximize the network energy efficiency subject to the minimum rate constraint and the access probability constraint, which is given by

$$\begin{aligned} \text{(EE)} \quad & \max \sum_i \eta_i \\ \text{s.t.} \quad & R_i \geq R_i^{min} \\ & \sum_i \tau_i \leq 1 \\ & 0 \leq \tau_i \leq 1 \\ & N_T^{min} \leq N_i^T \leq N_T^{max}. \end{aligned} \tag{4.68}$$

The Lagrangian of (4.68) is given by

$$L = \sum_i \eta_i + \sum_i \lambda_i\left(R_i - R_i^{min}\right) + \mu\left(1 - \sum_i \tau_i\right), \tag{4.69}$$

where λ_i is the Lagrangian variable associated with the minimum rate constraint of node i and μ is the Lagrangian variable related to the access probability constraint. Another important objective that is widely used in resource allocation problems is the sum of the logarithm of energy

efficiencies. To solve this problem, we replace the expression $\sum_i \eta_i$ in (4.68) and (4.69) with $\sum_i \log \eta_i$, and refer to the problem as (LogEE). The LogEE problem trades off efficiency to provide higher fairness.

The channel access probability and the PSDU frame length for all the nodes can be expressed as the vectors below

$$\boldsymbol{\tau} = [\tau_1, \tau_2, \dots, \tau_{N_s}], \tag{4.70}$$

$$\mathbf{N_T} = [N_1^T, N_2^T, \dots, N_{N_s}^T], \tag{4.71}$$

where the symbols in bold and not italic define vectors. The optimal solution, $(\boldsymbol{\tau}^*, \mathbf{N_T}^*)$, as well as the corresponding Lagrangian variables $\boldsymbol{\lambda}^* = [\lambda_1{}^*, \lambda_2{}^*, \dots, \lambda_{N_s}{}^*]$ and μ^* can be obtained by applying the Karush–Kuhn–Tucker optimality conditions, which are given by

$$\begin{gathered}
\sum_i \nabla_{\boldsymbol{\tau}} \eta_i (\boldsymbol{\tau}^*, \mathbf{N_T}^*) + \sum_i \lambda_i{}^* \nabla_{\boldsymbol{\tau}} R_i (\boldsymbol{\tau}^*, \mathbf{N_T}^*) - \mu^* \nabla_{\boldsymbol{\tau}} \left(\sum_i \tau_i{}^* \right) = 0, \\
\sum_i \nabla_{\mathbf{N_T}} \eta_i (\boldsymbol{\tau}^*, \mathbf{N_T}^*) + \sum_i \lambda_i{}^* \nabla_{\mathbf{N_T}} R_i (\boldsymbol{\tau}^*, \mathbf{N_T}^*) = 0, \\
\lambda_i{}^* \left[R_i(\boldsymbol{\tau}^*, \mathbf{N_T}^*) - R_i^{min} \right] = 0 \; and \; \lambda_i{}^* \geq 0, \\
\mu^* [1 - \textstyle\sum_i \tau_i{}^*] = 0 \; and \; \mu^* \geq 0,
\end{gathered} \tag{4.72}$$

where ∇_x is the gradient of a function with respect to the variable x. The problem (4.68) is a single-ratio fractional program and it can be translated into a dual fractional program, after which is solved via the Gauss-Seidel iterative method [68]. The dual fractional program is given by [70]

$$(\text{Dual} - \text{EE}) \qquad \min_{\boldsymbol{\lambda}, \mu \geq 0} \left[\max_{\boldsymbol{\tau}, \mathbf{N_T}} L \right]. \tag{4.73}$$

We denote this dual fractional program as (Dual-EE) if the maximization of the sum of energy efficiency is considered. If the sum of the logarithmic energy efficiency is evaluated, the corresponding Lagrangian will be used and the dual fractional program will be named as (Dual-LogEE).

If there is no possible solution for problem (4.68), we will solve the problem (LogTHR) shown below,

$$\begin{aligned} \text{(LogTHR)} \quad & \max_{\boldsymbol{\tau},\mathbf{N_T}} \left(\sum\nolimits_i \log R_i \right) \\ \text{s.t.} \quad & \sum\nolimits_i \tau_i \le 1 \\ & 0 \le \tau_i \le 1 \\ & N_T^{min} \le N_i^T \le N_T^{max}. \end{aligned} \tag{4.74}$$

Algorithm 2. EECAP – Energy Efficiency Optimization of Channel Access Probabilities

Given $\mathbf{d}, \mathbf{h}, \mathbf{R^{min}}$ and N_S
Initialize $\boldsymbol{\tau}$ and $\mathbf{N}_\mathrm{T}$
repeat
  for node $k = \{1,2,\dots,N_\mathrm{S}\}$ **do**
    solve (4.62) to obtain $\tau_{k,\min}^{\mathrm{THR}}$
    solve (4.65) to obtain $N_{k,\mathrm{T}}^{\mathrm{THR}}$
  end for
until stopping criteria is satisfied
if $R_k\left(\boldsymbol{\tau}_{k,\min}^{\mathrm{THR}}, \mathbf{N}_{k,\mathrm{T}}^{\mathrm{THR}}\right) \ge R_k^{\min}$ and $\sum_k \tau_{k,\min}^{\mathrm{THR}} \le 1$ **then**
  repeat
    for node $k = \{1,2,\dots,N_\mathrm{S}\}$ **do**
      solve (4.73) to obtain $(\tau_k)^{\mathrm{EE}}$ and $(N_k^{\mathrm{T}})^{\mathrm{EE}}$
      $\lambda_k = \max\left(R_k^{\min} - R_k\left(\boldsymbol{\tau}^{\mathrm{EE}}, \mathbf{N}_{\mathrm{T}}^{\mathrm{EE}}\right), 0\right)$
    end for
    $\mu^{\mathrm{EE}} = \max(\sum_k (\tau_k)^{\mathrm{EE}} - 1, 0)$
  until stopping criteria is satisfied
  return $(\boldsymbol{\tau}^\star, \mathbf{N}_{\mathrm{T}}^\star) = (\boldsymbol{\tau}^{\mathrm{EE}}, \mathbf{N}_{\mathrm{T}}^{\mathrm{EE}})$
else
  repeat
  for node $k = \{1,2,\dots,N_\mathrm{S}\}$ **do**
    solve (4.74) to obtain $(\tau_k)^{\mathrm{LogTHR}}$ and $(N_k^{\mathrm{T}})^{\mathrm{LogTHR}}$
  end for
  $\mu^{\mathrm{LogTHR}} = \max(\sum_k (\tau_k)^{\mathrm{LogTHR}} - 1, 0)$
  until stopping criteria is satisfied
  return $(\boldsymbol{\tau}^\star, \mathbf{N}_{\mathrm{T}}^\star) = (\boldsymbol{\tau}^{\mathrm{LogTHR}}, \mathbf{N}_{\mathrm{T}}^{\mathrm{LogTHR}})$
end if

The problem (4.74) can be solved numerically by taking the Lagrangian and turning into a dual fractional problem. Then the optimal access probability $\boldsymbol{\tau}^{\mathrm{LogTHR}}$ can be solved iteratively and the optimal frame size $(\mathbf{N_T})^{\mathrm{LogTHR}}$ can be calculated by (4.65).

4.3.5 Algorithm

Our algorithm for the problem (4.68) includes three subproblems. We call them MIN-THR, OPT-L and OPT-LogTHR. The MIN-THR determines if the problem has a feasible solution over the space of $\boldsymbol{\tau}$ and$\mathbf{N_T}$. If MIN-THR succeeds, OPT-L will be implemented to determine the optimal solution that maximizes the energy efficiency under the constraints and solves the dual fractional program in (4.73). If MIN-THR fails, it means that there is no such a feasible solution that satisfies all the constraints, then OPT-LogTHR is applied and the solution that maximizes the sum of the logarithmic throughput will be the outcome. In this case, the energy efficiency is not considered and this typically occurs for high minimum rate constraints or at medium to high link distances between the nodes and hub. The proposed algorithm is presented in Algorithm 2.

4.3.6 Simulation Results

In this section, we evaluate the performance of our algorithm for the energy efficiency optimization under the rate and access probability constraints in MATLAB. The value of N_{cpb} is determined according to the link distances reported in Fig. 4.3(a). Therefore, in this simulation, we only do a joint optimization of the frame size and the channel access probability. This is different from the results generated by the first algorithm CLOEE. In CLOEE, we did a joint optimization of the frame size and the number of pulses per burst. It is a cross-layer optimization because frame size is a parameter in MAC layer and the number of pulses per burst is a PHY parameter. We employ the UWB channel model for WBANs in [71]. The values of the parameters in the energy consumption model are the same in Section 4.2.4.

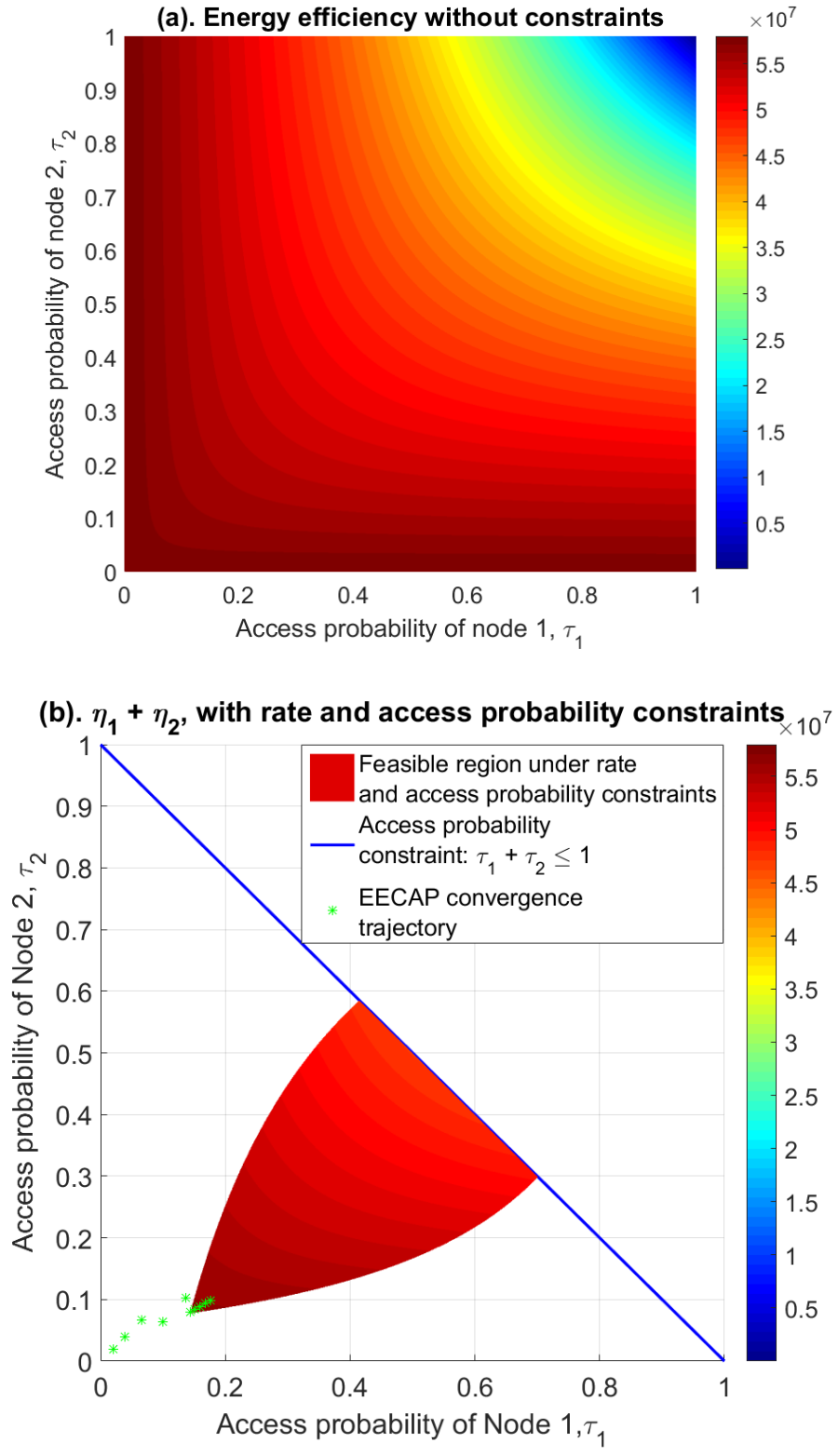

Figure 4.5. Feasibility regions of the (EE) and (LogEE) problems with and without constraints are depicted as a function of access probabilities of the two nodes. Link distance is 1 meter and the minimum rate constraint is taken as 1 Mbits/sec for node 1 and 0.5 Mbits/sec for node 2.

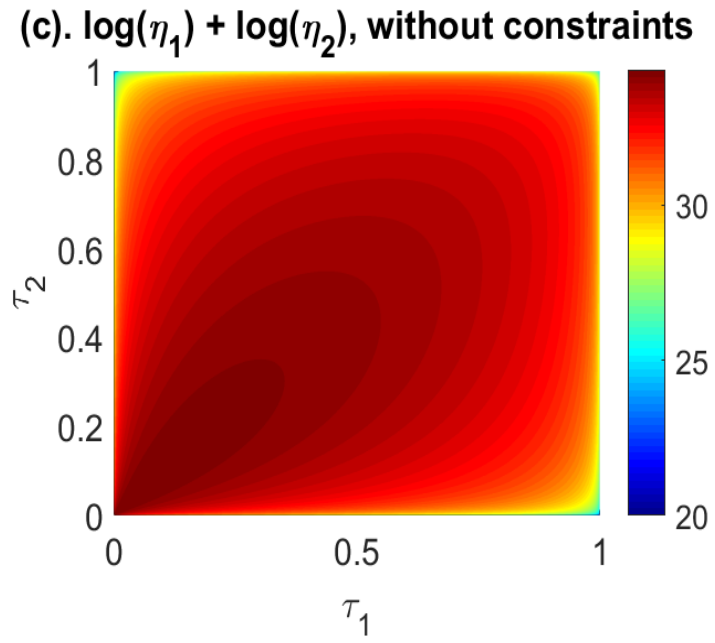

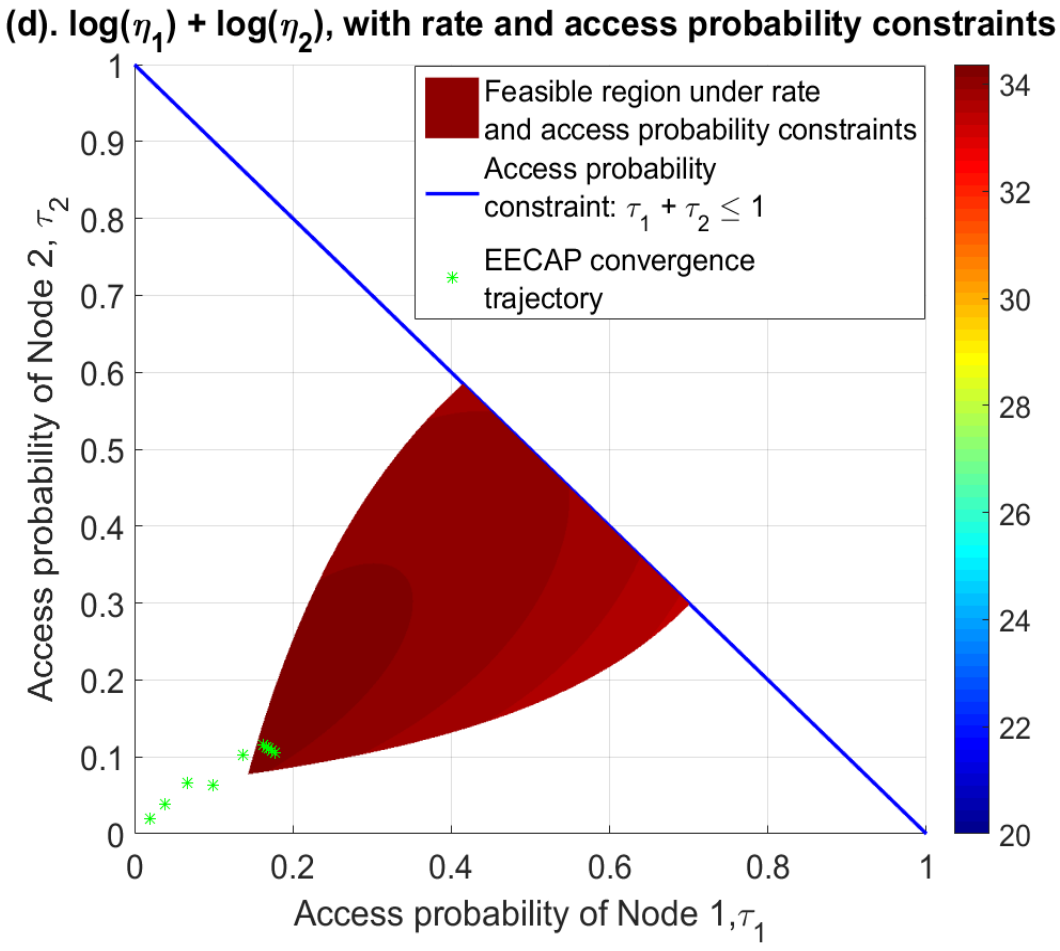

Figure 4.5. (Continued)

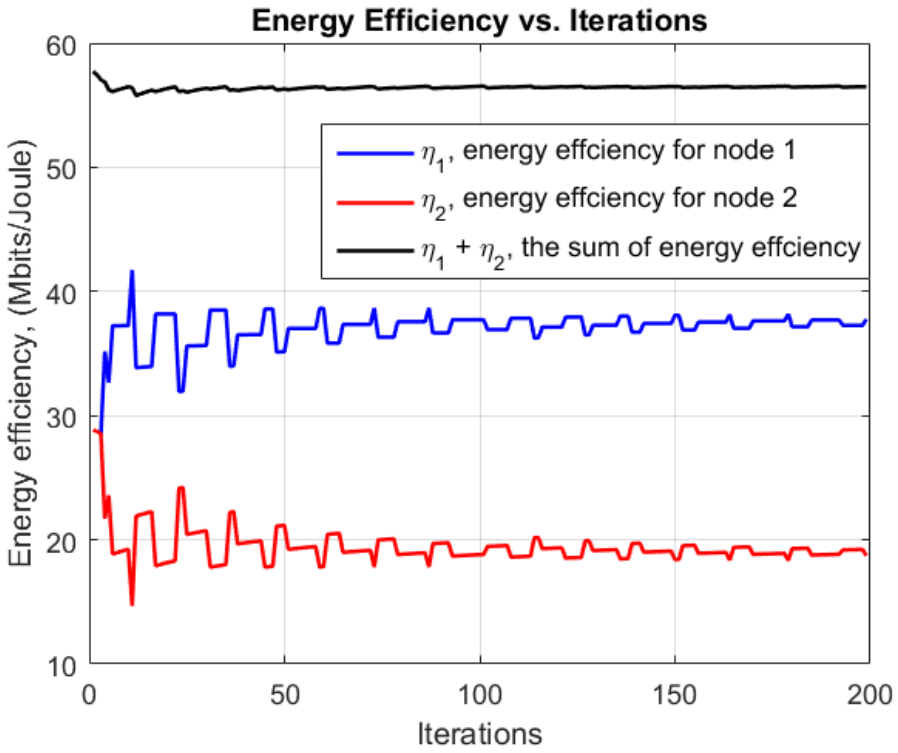

Figure 4.6. Energy efficiency versus iterations. Convergence of the proposed algorithm for the simulation in Fig. 4.5(b).

In Figs. 4.5(a)-(d), we first investigate the feasible regions of Problems (EE) and (LogEE) with and without rate constraints. For visual clarity, we present the results for only two nodes. Fig. 4.5(a) depicts the sum of energy efficiencies under no constraints. It can be observed that the maximum energy efficiency is obtained when either node's access probability is zero. Similarly, the sum of logarithmic energy efficiency is plotted in Fig. 4.5(c) without any constraint. The maximum is at $(0^+, 0^+)$. The reason for this is that since the collisions will waste energy and idle channel does not cost any energy, the system will try to avoid collisions at the sacrifice of reduced access probability. The sum of logarithmic energy efficiency (LogEE) provides a fair solution between the two nodes. Figs. 4.5(b) and (d) illustrate the feasible region with the rate and access constraints. We also plot the solution of EECAP with star and show its evolution over 200 iterations. We set the distance to be 1 meter for both nodes so that the optimal PSDU frame length is its maximum length. The rate constraint is set to be $(R_1^{min}, R_2^{min}) = (1, 0.5)$ Mbit/s. The optimal

solution $\boldsymbol{\tau}^*_{\mathbf{EE}}$ is $(0.1430, 0.0770)$ in Fig. 4.5(b) and $\boldsymbol{\tau}^*_{\mathbf{logEE}} = (0.1610, 0.1410)$ in Fig. 4.5(d). We can see that for the Problem (EE), ${\tau_1}^*$ is approximately twice as ${\tau_2}^*$, but for the (LogEE) problem, this is not the case since fairness is favored. For both cases, our algorithm is able to approach to the optimal solution in a limited number of iterations. We show the rapid convergence of our proposed algorithm in Fig. 4.6. It depicts the energy efficiency versus iterations. Note that these are also the results shown in Fig. 4.5(b). We set the initial value of the access probability as (0.01, 0.01), so that the sum of the energy efficiency is higher at first, but does not satisfy the rate constraints. After about 5 iterations, it steps into the feasible region and starts to look for the optimal solution that maximize the sum of energy efficiency. We can see that the fluctuations get smaller as more iterations are performed.

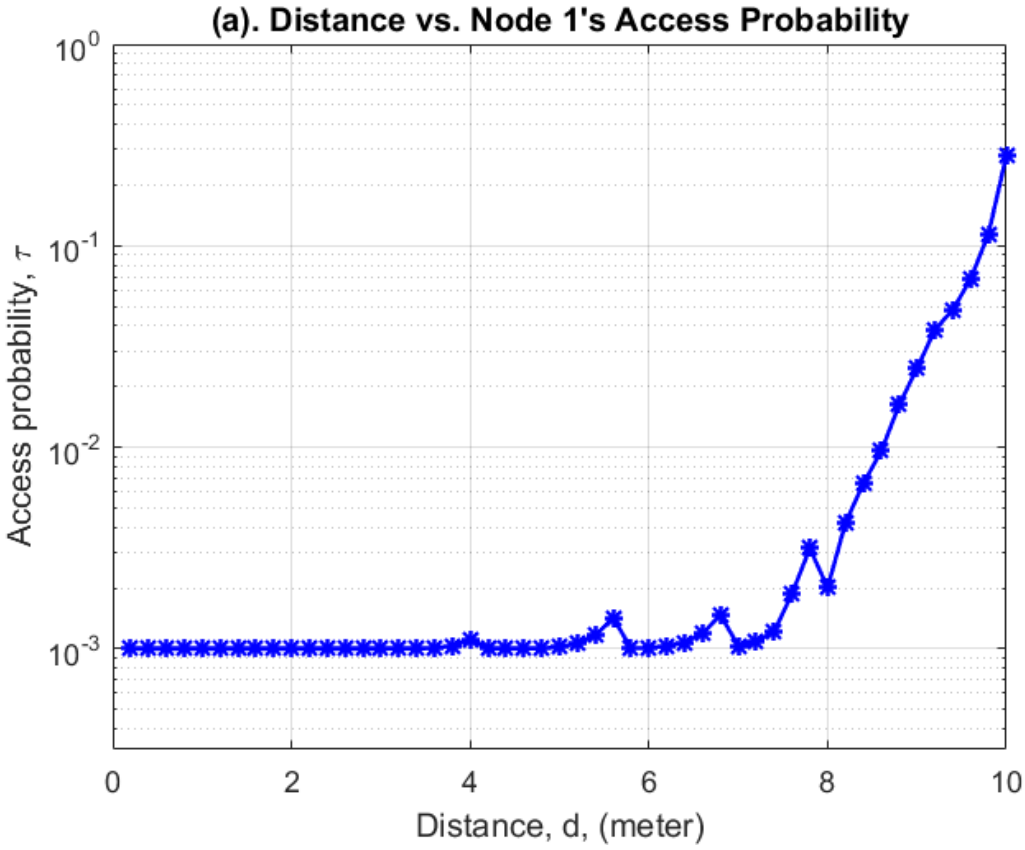

Figure 4.7. Link distance adaptation results for sum energy efficiency maximization under the rate and access probability constraints. Rate constraint is 1 Mbit/sec and the number of nodes is 2.

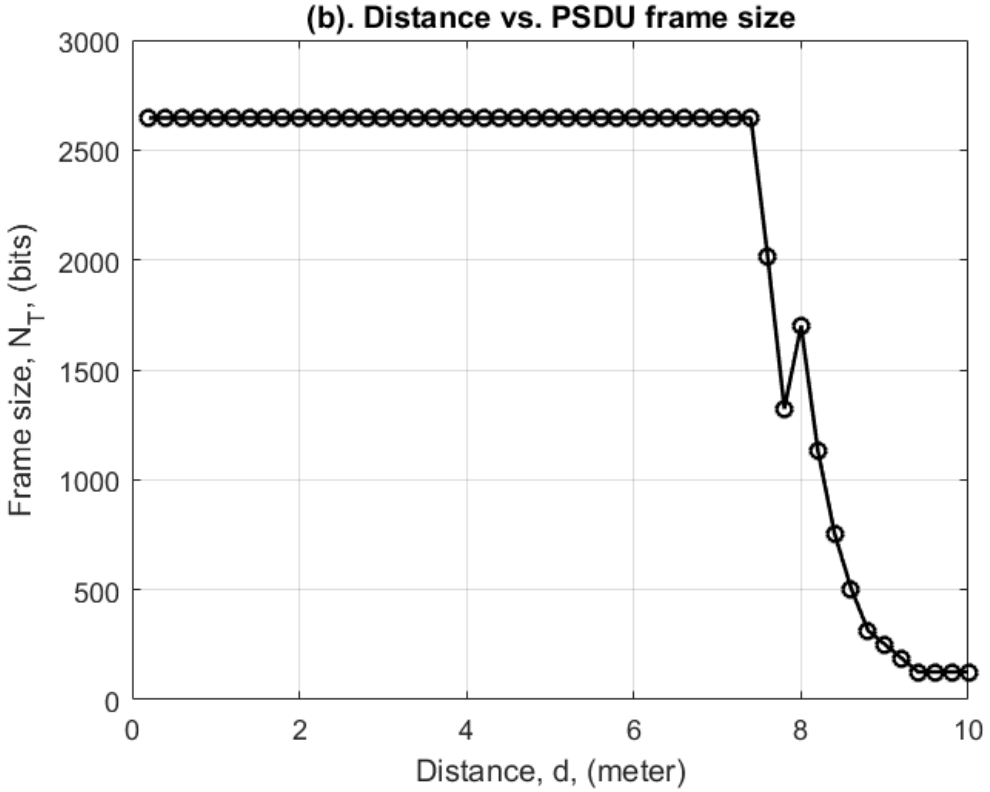

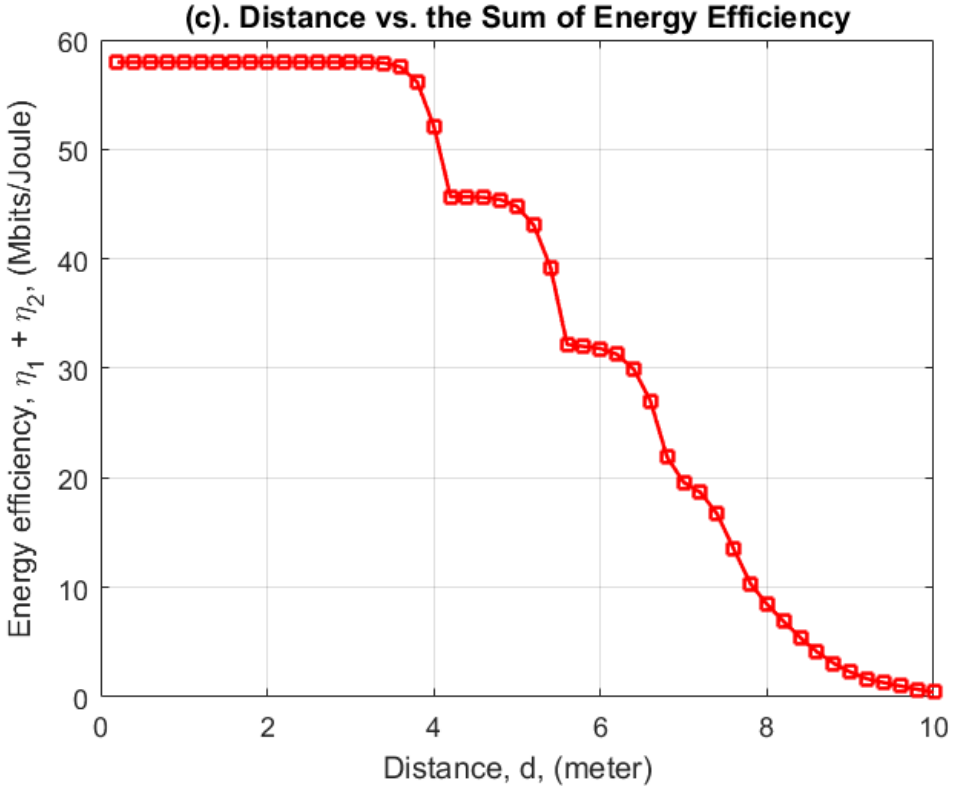

Figure 4.7. (Continued)

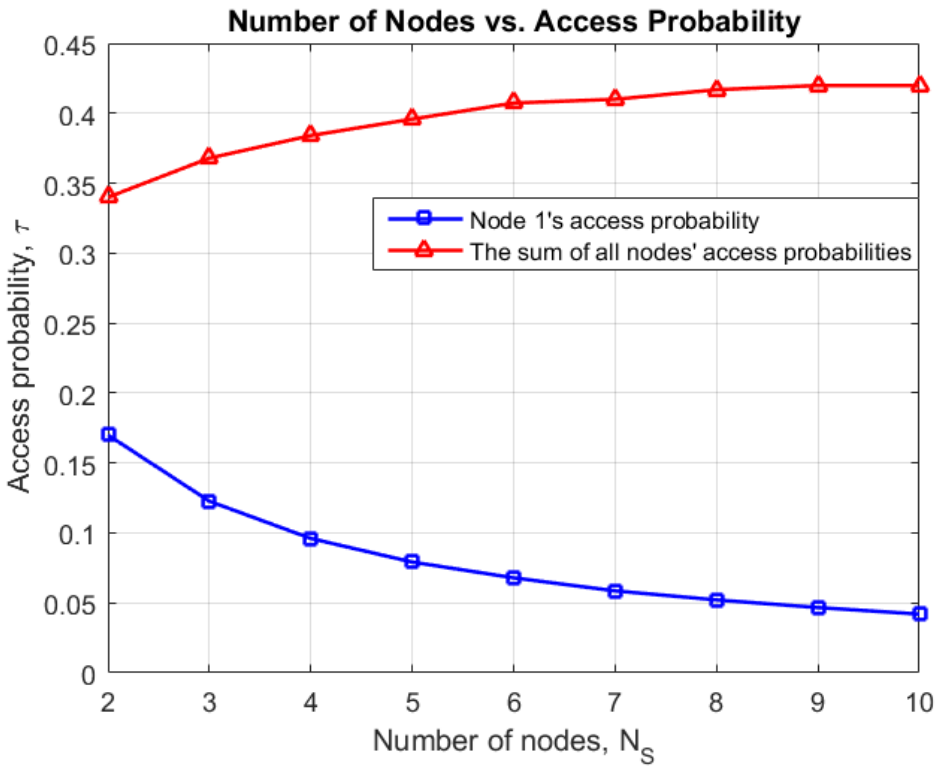

Figure 4.8. Optimal access probabilities versus the number of nodes for sum energy efficiency maximization with minimum rate constraint of 1 Mbits/s and link distances of 1 meter.

The distance between the node and the hub has a strong impact on the optimal channel access probability and frame length, since the probability of successful delivery of frames drops as the distance increases. We depict the distance versus the optimal access probability, optimal PSDU frame size, and sum of energy efficiencies, respectively, in Figs. 4.7(a)-(c). The number of nodes is 2 and the rate constraint is fixed to 18 Kbps. Only node 1's optimal access probability is displayed since the nodes are identical in this setting. When the distance grows above 7.5 meters, the error probability starts to increase significantly, which results in a sudden increase of the optimal access probability and a steep decrease of the optimized frame size. The same observation for the frame size was also reported in the results of CLOEE. The maximum energy efficiency also drops with distance. The transitions in Figs. 4.7(a)-(c) reflect the points where N_{cpb} changes. For example, at the link distances from $d = 7.8m$ to $d = 8m$, the decrease in the optimal access

probability (see Fig. 4.7(a)) and the increase in frame length (see Fig. 4.7(c)) are due to the selection of a higher N_{cpb} value to increase robustness.

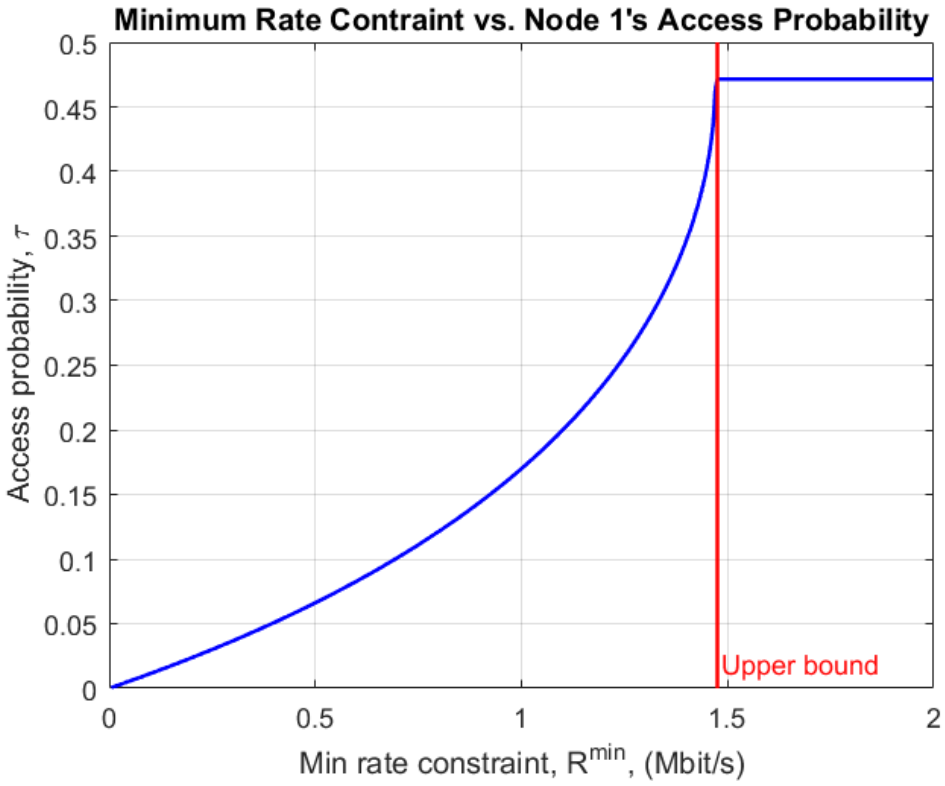

Figure 4.9. Optimal channel access probability solving (Dual-EE) and (LogTHR) for different values of minimum rate constraint in which the network has two nodes at link distances of 1 meter.

Figure 4.8 depicts the effect of the number of nodes on the optimal channel access probability that maximize the sum of energy efficiencies. The rate constraint fixed at 1 Mbits/sec. The node distances to the hub are taken as 1 meter and the number of nodes increases from two to ten. For an individual node, its optimal access probability decreases as the number of nodes grows. However, when we consider the overall system utilization, defined as the sum of individual access probabilities, it increases with the number of nodes.

Figure 4.9 shows the optimal access probability versus the rate constraints. The number of nodes is 2 and the distance is 1 meter. We note the upper bound of the minimum rate constraint is 1.475 Mbits/s. There is no feasible solution beyond this limit and the subproblem OPT-LogTHR

is solved to find the optimal access probability that maximizes the sum of logarithmic throughput. Before the upper bound, the optimal access probability exhibits an exponential increase with respect to the rate constraints.

4.4 Concluding Remarks

We designed two algorithms for energy efficiency optimization in IEEE 802.15.6 IR-UWB WBANs.

Low energy consumption, reliability, and high energy efficiency are essential for the operation of WBAN devices. The energy efficiency of WBANs closely depends on the choice of PHY and MAC layer related parameters. We have proposed a cross-layer optimization for network energy efficiency maximization for IEEE 802.15.6 IR-UWB WBANs. In particular, we derived a closed-form expression to determine the optimal frame size subject to the minimum rate constraints; further a search is performed for optimal number of pulses per burst. Our simulation results demonstrate that the proposed CLOEE algorithm achieves the same performance as an exhaustive search and provides significant improvements in terms of energy efficiency (by an order of magnitude) and transmission range (by a factor of two) compared to the static strategies. In the future work, the proposed algorithm will be extended to approximate the frame error rate as a function of P_b and N_{T} to obtain explicit expressions for N_{cpb}. As a final remark, the proposed CLOEE is universal and it can be applied to any network by updating the related frame parameters (e.g., size, sampling rate, and coding rate of the PHR, SHR, and PSDU), and bit error probabilities over the channel.

Considering the channel access probabilities, we first defined three channel states: successful transmission, collision and idle channel for the one-hop star WBAN and presented the optimum channel access probabilities for each state. Then, we formulated the problem of

optimizing the energy efficiency and throughput under the rate constraints and access probability constraints. We proposed an algorithm for each problem and evaluated its performance with simulations. In the simulations, the results from our algorithm were compared with an exhaustive search. It was observed that the proposed algorithm converges fast to the optimal solution. The difference of the two kinds of energy efficiency definitions, (EE) and (LogEE) was also investigated. Based on our study, we could conclude that the optimal access probability increases with the link distance and minimum rate constraint (exponentially) and decreases with the number of nodes.

CHAPTER 5. GAME THEORETICAL APPROACHES FOR ENERGY EFFICIENCY IN WBANS[5]

5.1 A Tutorial on Game Theory

Let us first present a brief review of the basics in game theory. The games can be defined in one of the following two ways: strategic and extensive forms. Consider the strategic form which is defined by the triple

$$< \mathcal{K}, \{S_k\}_{k\in\mathcal{K}}, \{u_k\}_{k\in\mathcal{K}} >, \tag{5.1}$$

where $\mathcal{K} = \{1,2,\ldots,N\}$ is the set of players, S_k is the set of strategies for player k, and u_k indicates the set of utilities for player k. There are three components in a game: players, strategies (actions), utilities (payoffs). The utility or payoff measures the level of satisfaction of the player. A pure strategy provides a complete definition of how a player will play a game. In particular, it determines the move a player will make for any situation it could face. A player's strategy set is the set of pure strategies available to that player. A mixed strategy is an assignment of a probability to each pure strategy. This allows for a player to randomly select a pure strategy. Since probabilities are continuous, there are infinitely many mixed strategies available to a player.

A non-cooperative game is a game with competition between individual players. The players are assumed to be selfish and try to maximize their own utility. When other players' strategies are fixed, the strategy (or strategies) that produces the most favorable outcome for a player is called the *best response* (BR) of this player. A *Nash Equilibrium* (NE) is a stable state of

[5] This chapter was published in [36]. Permissions are included in Appendix A.

a system involving the interaction of different participants, in which no participant can gain by a unilateral change of strategy if the strategies of the others remain unchanged. If a profile of actions has the feature that all the players play at their BRs, this profile of actions is a NE for this game.

Since the players are only concerned with their own payoffs, it is often that the NE is not efficient from the viewpoint of the whole system. The famous game, prisoner's dilemma, offers such an example. *Pareto optimality* (PO) can be used to check whether the solution is efficient or not. It is a state of allocation of resources in which it is impossible to make any one individual better off without making at least one individual worse off. The *Social Optimality* (SO) is often used as a measure for the efficiency of a strategy vector, which is defined as the profile that maximizes the weighted sum-utility.

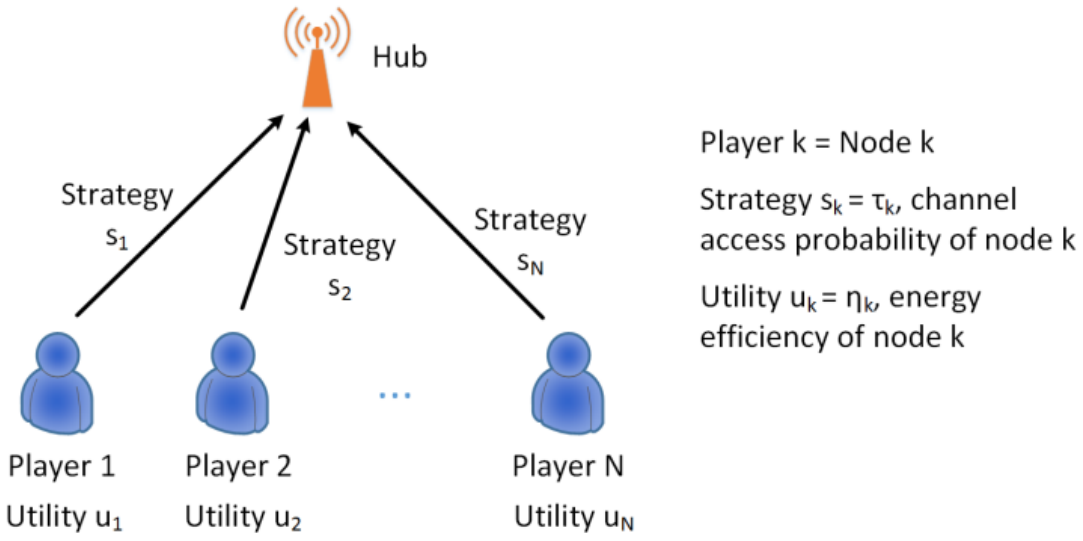

Figure 5.1. Energy efficiency game in IEEE 802.15.6 UWB WBANs.

To improve the overall efficiency and enable some level of cooperation in the game, there are two common methods. First method is to provide a recommended strategy by a public signal and let each player choose its action according to its observation of the same public signal (e.g. the traffic light in a traffic game). If no player has any incentive to deviate from the recommended

strategy, then it is called as a *Correlated Equilibrium* (CE). For the first method, we can consider that the hub in a star topology provides the public signal using a broadcast frame. The second method is the repeated game in which players participate in repeated interactions within a finite or potentially infinite time horizon. Then the game has its history. The assumptions can be complete/incomplete information and perfect/imperfect monitoring. The complete information means that each player has the information on others. The perfect monitoring means each player has the record of all past actions and outcomes. While playing the game, each player tries to maximize its expected payoff.

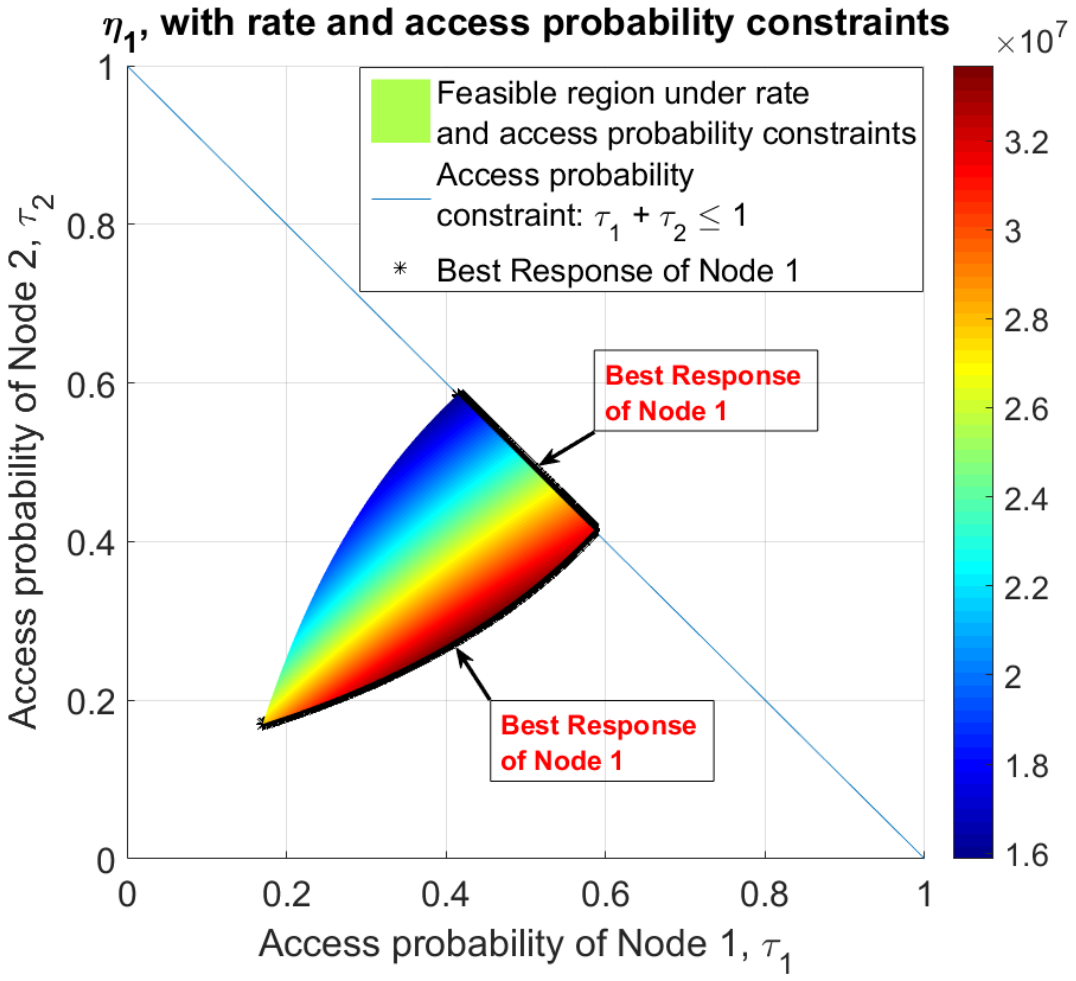

(a)

Figure 5.2. Best responses of Node 1 and Node 2.

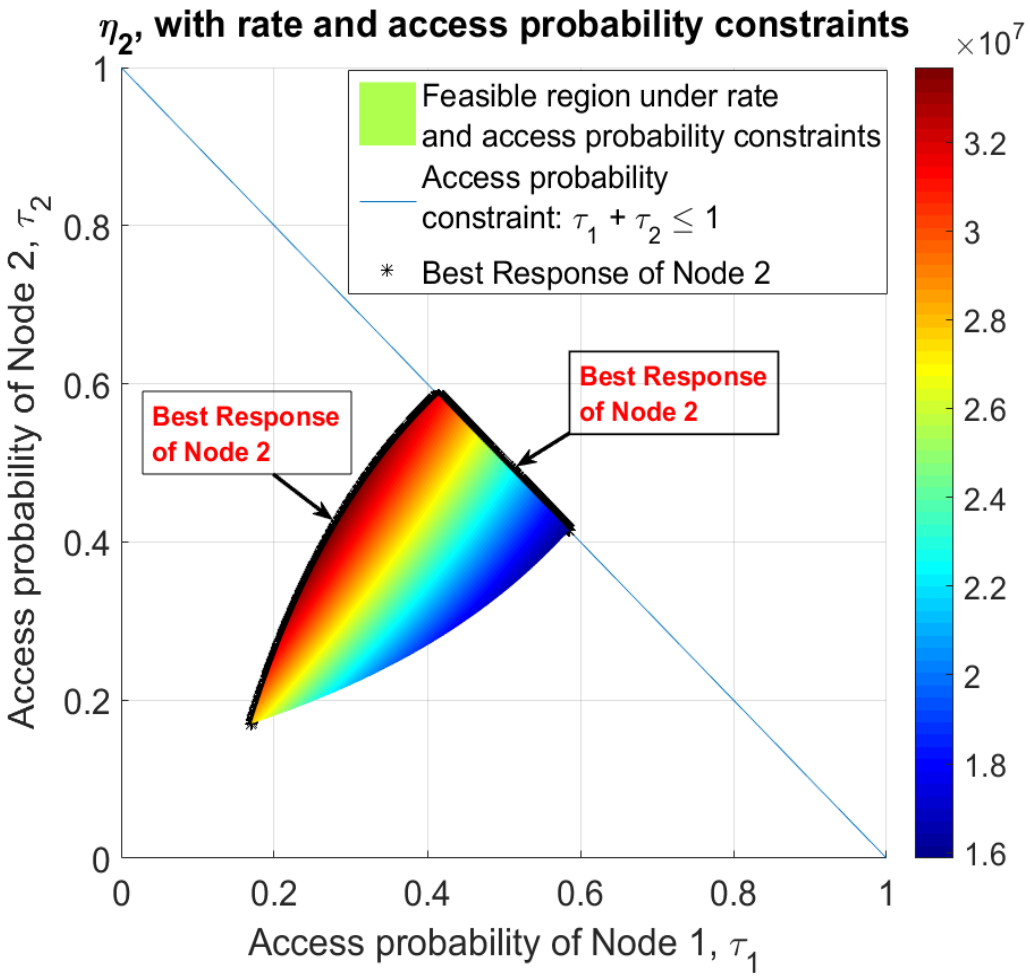

(b)

Figure 5.2. (Continued)

5.2 Definition of the Energy Efficiency Game

Consider again the one-hop star network topology in Fig. 5.1 for two users. We define an energy efficiency game that takes into account the rate and access probabilities. The strategy of player k is the channel access probability τ_k with the utility function where the energy efficiency is defined in Chapter 4. This is a game with continuous strategy and can be formulated as a single-stage or repeated game. This assignment of the strategy and utility can be changed according to the specific requirements. We examine the best responses and provide the NE for the single-stage game. The frontier of PO is plotted to check the efficiency of the NE. We show that cooperation

is need to improve the efficiency of the game. Our observations and conclusions can be extended to multiple users.

5.3 Best Responses and Nash Equilibrium of the Energy Efficiency Game

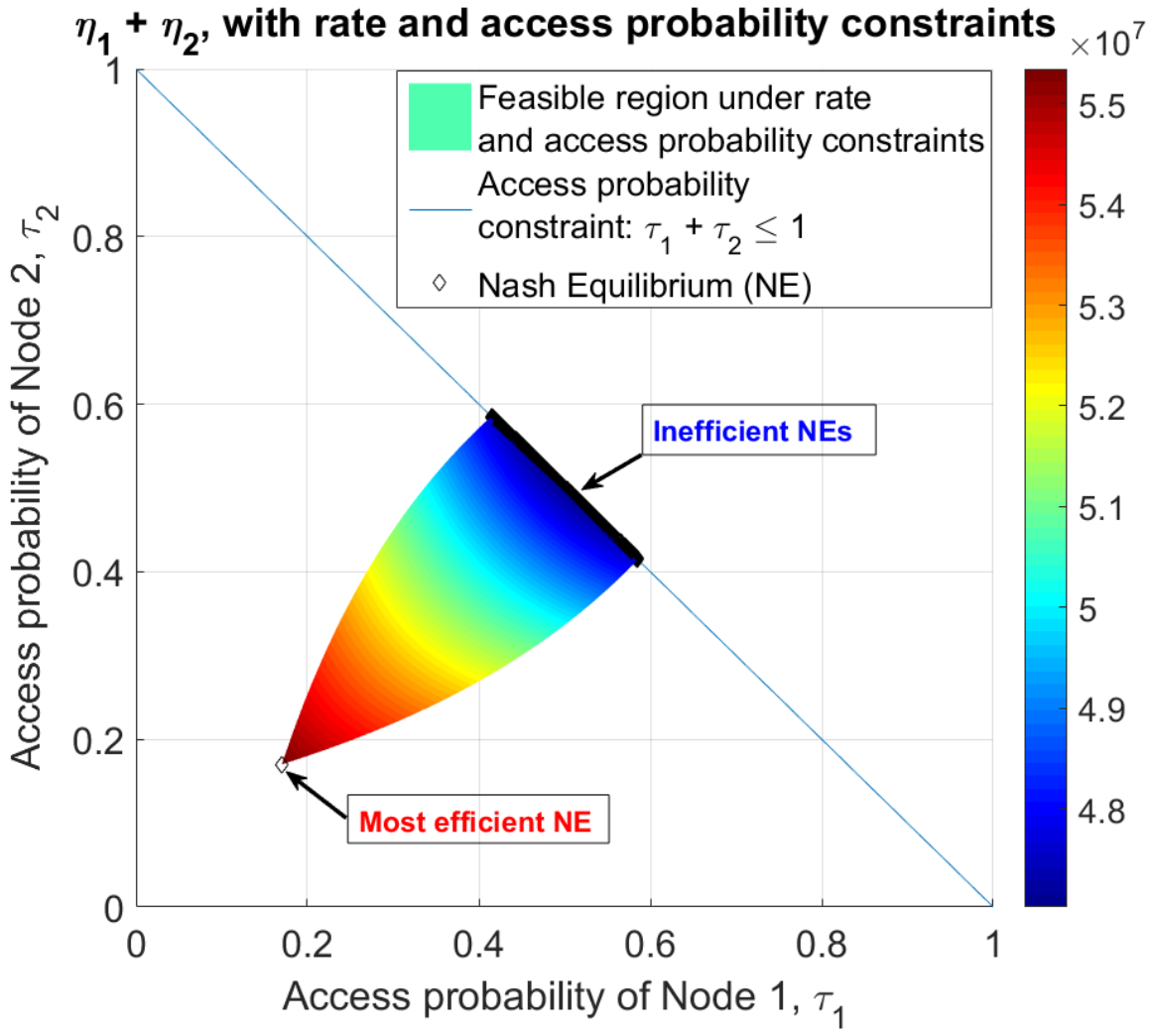

Figure 5.3. Nash Equilibrium (NE) of single-stage energy efficiency game.

The best response of node k is its strategy that maximize its own utility when other players' strategies are fixed. For the game with two nodes, when node 1(2)'s access probability is fixed, the best response of node 2(1) is the access probability that maximizes $u_2 = \eta_2$ ($u_1 = \eta_1$). The results are shown in Fig. 5.2(a-b). By taking the overlap of best responses of two nodes, we obtain the NE of the game that is depicted in Fig. 5.3. We observe that there are multiple NEs for this

game and most of them are not efficient because they are close to the blue color. Therefore, the cooperation is necessary for the energy efficiency game. The possible solutions are CE, game with pricing, and repeated games.

5.4 Cooperation in the Energy Efficiency Game

5.4.1 Pareto Optimality and Social Optimality

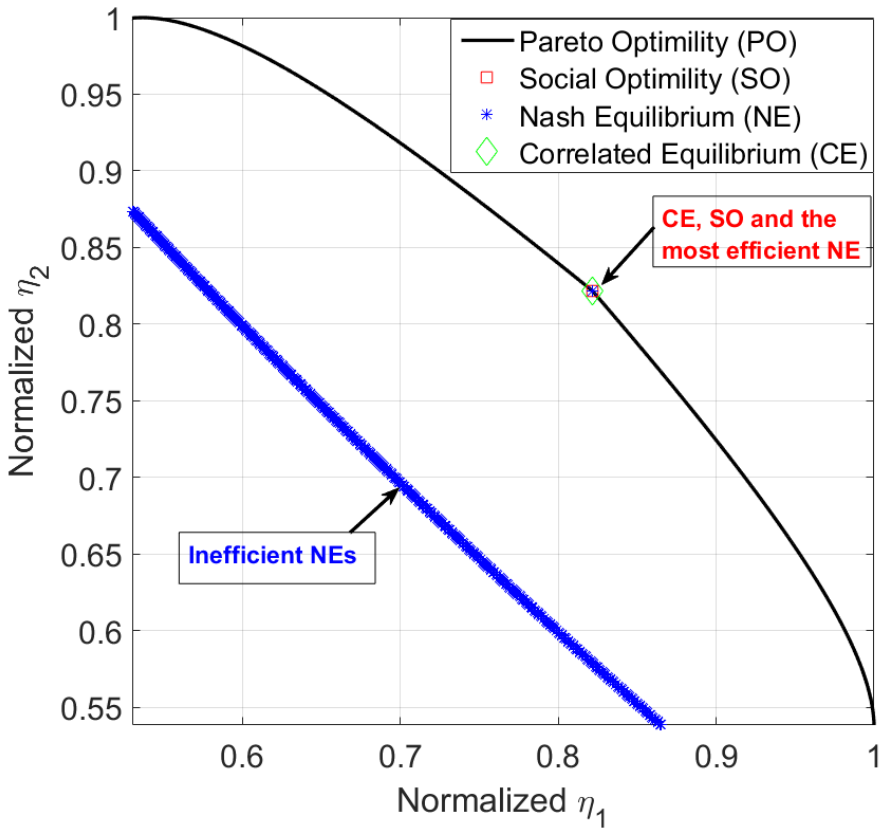

Figure 5.4. Efficiency evaluation of Pareto Optimality (PO), Social Optimality (SO), Correlated Equilibrium (CE) and Nash Equilibrium (NE).

In Fig. 5.4, we plot the PO, SO, CE, and NE in the coordinates of normalized energy efficiency. The PO measures the efficiency of the game and any point below the curve of PO is regarded as energy inefficient. We can observe that most of the NEs are not energy efficient. The point of SO, CE, and the most efficient NE point coincide. The SO maximizes the weighted sum utilities and the utilities are equally weighted in Fig. 5.4.

5.4.2 Correlated Equilibrium

The CE is a generalization of the NE, where an arbitrator (public signal) helps the players to correlate their strategies, so as to favor a decision process in the interplay. In Fig. 5.4, we assume that the public signal is sent by the hub that solves the problem of energy efficiency maximization and broadcasts each user its channel access probability, τ_k.

5.4.3 Repeated Game

A direct extension is to extend the single stage game to a multi-stage repeated games where the users are more patient and have discounted utilities. Constructing an equilibrium that gives the players incentive to cooperate and not deviate from this equilibrium is an important research question that closely depends on the protocol and device specific parameters. Energy efficient punishment strategies for cheating player is also an important research area.

We develop a repeated game model using the Grim Trigger strategy, the steps are: 1). The nodes solve the most efficient solution, denoted as S^*, by making $R_i = R_i^{min}$. 2). The nodes play with the implicitly agreed action profile S^* if no deviation is detected. 3). If there is a deviation, the punishment strategy is playing at $\tau_{\mathrm{i}} = 1$, making all other users' energy efficiency to be zero. 4). The discounted payoff is $u_i = (1-\delta)\sum_{t=0}^{\infty}\delta^t\eta_i$, where δ is the discount factor. 5). All users prefer to cooperate (i.e. play S^*), if we design the discount factor $\delta > \max_i\{1-\eta_i^{S^*}/\eta_i^P\}$, where $\eta_i^{S^*}$ is the energy efficiency when user i plays S^* and η_i^P is the energy efficiency when user i plays the punishment strategy. This repeated game model has the same performance as the most efficient NE point.

5.5 Concluding Remarks

In this chapter, we first view the energy efficiency problem in the perspective of game theory, which acts as a distributed method of optimization, compared to the centralized method of

optimization presented in Chapter 4. After building the game model, we analyze the best responses and Nash Equilibrium points of the game. It is shown that the game has multiple NE points and most of the NE points are inefficient from the view of the entire system. To solve this problem, we develop two methods, Correlated Equilibrium and Repeated Game, to encourage some level of cooperation for this non-cooperative game and show that they can achieve the same performance as the centralized method described in Chapter 4. A comparison of the methods in Chapter 4 and Chapter 5 is given in Table 5-1.

Table 5-1. Overview of approaches for optimizing energy efficiency in WBANs.

	Chapter 4. Energy Efficiency Optimization in WBANs	Chapter 5. Game Theoretical Approaches for Energy Efficiency in WBANs
Architecture	Centralized	Distributed (Cooperative and Non-Cooperative)
Assumptions	The hub sends the optimized parameters to the nodes	Non-cooperative game (with some level of cooperation)
Approaches	CLOEE and EECAP	Correlated Equilibrium (CE) and Repeated Game (RG)
Scalability	No	Yes
Application	Networks with a hub/centralized node	Distributed networks such as *ad hoc*
Benefit	Efficient for the network with a powerful hub	Enhance network scalability via distributed control
Constraints	Rate and access probability	Rate and access probability
Results	Efficiently determines the optimal solution	Achieves the same optimization results as Centralized approach

CHAPTER 6. CONCLUSION AND FUTURE DIRECTIONS[6]

6.1 Main Contributions and Conclusions

This dissertation is about the research in Wireless Body Area Networks (WBANs). As a part of WBANs, the *in vivo* communications requires the characterization of the *in vivo* channel. Chapter 3 of this dissertation mainly deals with the characterization of the *in vivo* wireless channel. It is shown that the *in vivo* wireless channel has distinguished characteristics compared to the classic cellular and free space channel. The attenuation is higher and also varies with angles. In the characterization, we build the mathematical model with respect to frequency and distance, utilizing the human body model in HFSS. Our proposed model fits well with the measured data. For the angular dependence of the *in vivo* path loss, we show that the angular dependence is similar at different frequencies in terms of peak to average ratio. Some results in MIMO *in vivo* project are also presented in this chapter.

In the next chapter, we focus on the energy efficiency optimization in WBANs under the standard of IEEE 802.15.6 IR-UWB. Two algorithms, CLOEE and EECAP, were proposed to maximize the energy efficiency under a variety of constraints. CLOEE provides cross-layer optimization of the frame size (MAC) and modulation level (PHY). EECAP considers different channel states and gives the optimal channel access probability and frame size. Both algorithms are computationally efficient and can be extended to two-hop WBANs and 5G/IoT networks.

[6] This chapter was published in [36]. Permissions are included in Appendix A.

We solve the same problem in Chapter 5 in the perspective of game theory. Energy efficiency game was built and it was demonstrated that cooperation is necessary to achieve social efficiency. Approach is extensible to 5G/IoT networks. Correlated Equilibrium and Repeated Game were investigated to enable cooperation.

6.2 Future Directions

- *Delay requirements and Lyapunov Optimization*: While we considered the joint power and data rate requirements for the link adaptation problem in this paper, one can also formulate another joint design objective such as optimizing the throughput and delay. The data for delay sensitive applications such as video and voice-over-IP can be prioritized over the delay-insensitive applications such as messaging. There has been research on formulating the energy efficiency and lifetime maximization problems subject to delay and energy constraints using a stochastic network optimization framework. Open research problems of incorporating rate and delay constraints with interfering links into the problem while maximizing the network energy efficiency still remain as an active research area.
- *Duty Cycling, Sleep Modes, and Energy Consumption Characterization in Sleep Modes*: Depending on the devices architecture and application demands, the devices can enter the *deep sleep modes* or *light sleep modes*. On one hand, in the deep sleep mode, the device can turn off multiple components and achieve higher energy savings at the cost of a longer wake-up time. On the other hand, the light sleep mode offers less energy savings at the benefit of a shorter wake-up time. When the device has enough data to transmit, the device can wake up from its deep sleep and transmit its data, while it waits the acknowledgement messages entering the light sleep mode. A major challenge that

needs to be addressed to design intelligent MAC protocols with deep and light sleep modes is that the energy consumption of the components of a device need to be characterized precisely in the operation, light sleep, and deep sleep modes so that these values can be incorporated into the MAC protocols. Also, the interoperability between devices from different manufacturers with possibly different device energy consumption need to be taken into account.

- *Wake-up Radios:* Another important research area for energy efficiency is the implementation of WuR-based MAC and routing protocols, and the WuR hardware circuitry design. The WuR radios are extremely useful in applications where events rarely occur but the environment need to be constantly monitored. Devices with WuR capabilities can be active for extended time periods since they can stay in sleep modes longer. However, despite the low power consumption of WuR circuits, their receiver sensitivity is low which limits their communication range. Therefore, extending the communication range of WuRs is a very critical. Also, the false positives in wake-up calls (WuCs) need to be reduced. A WuR employs MAC messages with a flexible address header with specific destinations. Hardware design solutions such as preamble detectors, that filter out the common interference sources and alleviate false wake-up interrupts, are needed to complement the WuR-based MAC and routing protocols.

REFERENCES

[1] M. Chen, S. Gonzalez, A. Vasilakos, H. Cao, and V. C. Leung, "Body Area Networks: A Survey," *Mob Netw Appl*, vol. 16, no. 2, pp. 171–193, Apr. 2011.

[2] S. Ullah *et al.*, "A Comprehensive Survey of Wireless Body Area Networks," *J. Med. Syst.*, vol. 36, no. 3, pp. 1065–1094, Jun. 2012.

[3] K.-S. Kwak, S. Ullah, and N. Ullah, "An overview of IEEE 802.15.6 standard," in *2010 3rd International Symposium on Applied Sciences in Biomedical and Communication Technologies (ISABEL)*, 2010, pp. 1–6.

[4] H. S. Savci, A. Sula, Z. Wang, N. S. Dogan, and E. Arvas, "MICS transceivers: regulatory standards and applications [medical implant communications service]," in *IEEE SoutheastCon, 2005. Proceedings*, 2005, pp. 179–182.

[5] Q. Zhao and B. M. Sadler, "A Survey of Dynamic Spectrum Access," *IEEE Signal Process. Mag.*, vol. 24, no. 3, pp. 79–89, May 2007.

[6] B. Allen, M. Dohler, E. Okon, W. Q. Malik, A. Brown, and D. J. Edwards, *Ultra-wideband: antennas and propagation for communications, radar and imaging*. Wiley-Blackwell, 2006.

[7] T. Rappaport, *Wireless Communications: Principles and Practice*, 2nd ed. Upper Saddle River, NJ, USA: Prentice Hall PTR, 2001.

[8] T. C. W. Schenk, N. S. Mazloum, L. Tan, and P. Rutten, "Experimental characterization of the body-coupled communications channel," in *IEEE International Symposium on Wireless Communication Systems. 2008. ISWCS '08*, 2008, pp. 234–239.

[9] D. Smith, L. Hanlen, J. Zhang, D. Miniutti, D. Rodda, and B. Gilbert, "Characterization of the Dynamic Narrowband On-Body to Off-Body Area Channel," in *IEEE International Conference on Communications, 2009. ICC '09*, 2009, pp. 1–6.

[10] J. Ryckaert, P. De Doncker, R. Meys, A. de Le Hoye, and S. Donnay, "Channel model for wireless communication around human body," *Electron. Lett.*, vol. 40, no. 9, p. 543, 2004.

[11] Y. Hao *et al.*, "Statistical and deterministic modelling of radio propagation channels in WBAN at 2.45GHz," in *IEEE Antennas and Propagation Society International Symposium 2006*, 2006, pp. 2169–2172.

[12] K. Takizawa *et al.*, "Channel models for wireless body area networks," in *30th Annual International Conference of the IEEE Engineering in Medicine and Biology Society, 2008. EMBS 2008*, 2008, pp. 1549–1552.

[13] J. M. Choi, H.-J. Kang, and Y.-S. Choi, "A Study on the Wireless Body Area Network Applications and Channel Models," in *Second International Conference on Future Generation Communication and Networking, 2008. FGCN '08*, 2008, vol. 2, pp. 263–266.

[14] M. Hamalainen, A. Taparugssanagorn, and J. Iinatti, "On the WBAN radio channel modelling for medical applications," in *Proceedings of the 5th European Conference on Antennas and Propagation (EUCAP)*, 2011, pp. 2967–2971.

[15] H. Viittala, M. Hamalainen, J. Iinatti, and A. Taparugssanagorn, "Different experimental WBAN channel models and IEEE802.15.6 models: Comparison and effects," in *2nd International Symposium on Applied Sciences in Biomedical and Communication Technologies, 2009. ISABEL 2009*, 2009, pp. 1–5.

[16] "'ANSYS HFSS' [Online]. Available: http://www.ansys.com/Products/Simulation+Technology/Electronics/Signal+Integrity/ANSYS+HFSS [Accessed: 8-Oct-2014]."

[17] "'SystemVue Electronic System-Level (ESL) Design Software.' [Online]. Available: http://www.keysight.com/en/pc-1297131/systemvue-electronic-system-level-esl-design-software?nid=-34264.0&cc=US&lc=eng [Accessed: 8-Oct-2014]."

[18] C. He, Y. Liu, T. P. Ketterl, G. E. Arrobo, and R. D. Gitlin, "MIMO *in vivo*," in *Wireless and Microwave Technology Conference (WAMICON), 2014 IEEE 15th Annual*, 2014, pp. 1–4.

[19] C. He, Y. Liu, T. P. Ketterl, G. E. Arrobo, and R. D. Gitlin, "Performance Evaluation for MIMO *In Vivo* WBAN Systems," *ArXiv14098642 Cs Math*, Sep. 2014.

[20] "IEEE SA - 802.15.6-2012 - IEEE Standard for Local and metropolitan area networks - Part 15.6: Wireless Body Area Networks." [Online]. Available: https://standards.ieee.org/findstds/standard/802.15.6-2012.html. [Accessed: 22-Sep-2016].

[21] K. Davaslioglu, Y. Liu, and R. D. Gitlin, "CLOEE - Cross-Layer Optimization for Energy Efficiency of IEEE 802.15.6 IR-UWB WBANs," *ArXiv160905256 Cs Math*, Sep. 2016.

[22] F. Cuomo, C. Martello, A. Baiocchi, and F. Capriotti, "Radio resource sharing for ad hoc networking with UWB," *IEEE J. Sel. Areas Commun.*, vol. 20, no. 9, pp. 1722–1732, Dec. 2002.

[23] F. Touati and R. Tabish, "U-Healthcare System: State-of-the-Art Review and Challenges," *J. Med. Syst.*, vol. 37, no. 3, p. 9949, Jun. 2013.

[24] S. Movassaghi, M. Abolhasan, J. Lipman, D. Smith, and A. Jamalipour, "Wireless Body Area Networks: A Survey," *IEEE Commun. Surv. Tutor.*, vol. 16, no. 3, pp. 1658–1686, Third 2014.

[25] R. Cavallari, F. Martelli, R. Rosini, C. Buratti, and R. Verdone, "A Survey on Wireless Body Area Networks: Technologies and Design Challenges," *IEEE Commun. Surv. Tutor.*, vol. 16, no. 3, pp. 1635–1657, Third 2014.

[26] H. Karvonen, J. Iinatti, and M. Hämäläinen, "A cross-layer energy efficiency optimization model for WBAN using IR-UWB transceivers," *Telecommun. Syst.*, vol. 58, no. 2, pp. 165–177, Nov. 2014.

[27] M. S. Mohammadi, Q. Zhang, E. Dutkiewicz, and X. Huang, "Optimal Frame Length to Maximize Energy Efficiency in IEEE 802.15.6 UWB Body Area Networks," *IEEE Wirel. Commun. Lett.*, vol. 3, no. 4, pp. 397–400, Aug. 2014.

[28] M. S. Mohammadi, E. Dutkiewicz, Q. Zhang, and X. Huang, "Optimal Energy Efficiency Link Adaptation in IEEE 802.15.6 IR-UWB Body Area Networks," *IEEE Commun. Lett.*, vol. 18, no. 12, pp. 2193–2196, Dec. 2014.

[29] C. Tachtatzis, F. D. Franco, D. C. Tracey, N. F. Timmons, and J. Morrison, "An energy analysis of IEEE 802.15.6 scheduled access modes," in *2010 IEEE Globecom Workshops*, 2010, pp. 1270–1275.

[30] C. Tachtatzis, F. D. Franco, D. C. Tracey, N. F. Timmons, and J. Morrison, "An Energy Analysis of IEEE 802.15.6 Scheduled Access Modes for Medical Applications," in *Ad Hoc Networks*, 2011, pp. 209–222.

[31] Y. Liu and R. D. Gitlin, "A phenomenological path loss model of the *in vivo* wireless channel," in *2015 IEEE 16th Annual Wireless and Microwave Technology Conference (WAMICON)*, 2015, pp. 1–3.

[32] *Advances in Body-Centric Wireless Communication: Applications and state-of-the-art*. IET Digital Library, 2016.

[33] Y. Liu, T. P. Ketterl, G. E. Arrobo, and R. D. Gitlin, "Modeling the wireless *in vivo* path loss," in *2014 IEEE MTT-S International Microwave Workshop Series on RF and Wireless Technologies for Biomedical and Healthcare Applications (IMWS-Bio2014)*, 2014, pp. 1–3.

[34] C. He, Y. Liu, G. E. Arrobo, T. P. Ketterl, and R. D. Gitlin, "*In vivo* wireless communications and networking," in *2015 Information Theory and Applications Workshop (ITA)*, 2015, pp. 163–172.

[35] Y. Liu, K. Davaslioglu, and R. D. Gitlin, "Energy Efficiency Optimization of Channel Access Probabilities in IEEE 802.15.6 UWB WBANs," *ArXiv161002092 Cs*, Oct. 2016.

[36] Y. Liu, K. Davaslioglu, and R. D. Gitlin, "Energy Efficiency and Resource Allocation of IEEE 802.15.6 IR-UWB WBANs: Current State-of-the-Art and Future Directions," presented at the Information Theory and Applications Workshop (ITA), San Diego, CA, 2017.

[37] M. Hatay, "Empirical formula for propagation loss in land mobile radio services," *IEEE Trans. Veh. Technol.*, vol. 29, no. 3, pp. 317–325, Aug. 1980.

[38] L. J. Greenstein, V. Erceg, Y. S. Yeh, and M. V. Clark, "A new path-gain/delay-spread propagation model for digital cellular channels," *IEEE Trans. Veh. Technol.*, vol. 46, no. 2, pp. 477–485, May 1997.

[39] S. L. Cotton and W. G. Scanlon, "Channel Characterization for Single- and Multiple-Antenna Wearable Systems Used for Indoor Body-to-Body Communications," *IEEE Trans. Antennas Propag.*, vol. 57, no. 4, pp. 980–990, 2009.

[40] T.-H. Kim, J.-H. Oh, W.-J. Jeong, J.-H. Yoo, and J.-K. Pack, "Channel modelling of WBAN system and human exposure due to WPT," in *2010 Asia-Pacific Symposium on Electromagnetic Compatibility (APEMC)*, 2010, pp. 29–32.

[41] K. Sayrafian-Pour, W.-B. Yang, J. Hagedorn, J. Terrill, K. Y. Yazdandoost, and K. Hamaguchi, "Channel Models for Medical Implant Communication," *Int. J. Wirel. Inf. Netw.*, vol. 17, no. 3–4, pp. 105–112, Dec. 2010.

[42] D. Kurup, W. Joseph, G. Vermeeren, and L. Martens, "In-body Path Loss Model for Homogeneous Human Tissues," *IEEE Trans. Electromagn. Compat.*, vol. 54, no. 3, pp. 556–564, Jun. 2012.

[43] A. Alomainy and Y. Hao, "Modeling and Characterization of Biotelemetric Radio Channel From Ingested Implants Considering Organ Contents," *IEEE Trans. Antennas Propag.*, vol. 57, no. 4, pp. 999–1005, Apr. 2009.

[44] T. P. Ketterl, G. E. Arrobo, A. Sahin, T. J. Tillman, H. Arslan, and R. D. Gitlin, "*In vivo* wireless communication channels," in *Wireless and Microwave Technology Conference (WAMICON), 2012 IEEE 13th Annual*, 2012, pp. 1–3.

[45] T. P. Ketterl, G. E. Arrobo, and R. D. Gitlin, "SAR and BER evaluation using a simulation test bench for *in vivo* communication at 2.4 GHz," in *Wireless and Microwave Technology Conference (WAMICON), 2013 IEEE 14th Annual*, 2013, pp. 1–4.

[46] J. Kim and Y. Rahmat-Samii, "Implanted antennas inside a human body: simulations, designs, and characterizations," *IEEE Trans. Microw. Theory Tech.*, vol. 52, no. 8, pp. 1934–1943, Aug. 2004.

[47] K. Y. Yazdandoost, "A 2.4 GHz antenna for medical implanted communications," in *Microwave Conference, 2009. APMC 2009. Asia Pacific*, 2009, pp. 1775–1778.

[48] K. Y. Yazdandoost and R. Kohno, "An antenna for medical implant communications system," in *Microwave Conference, 2007. European*, 2007, pp. 968–971.

[49] T. Houzen, M. Takahashi, K. Saito, and K. Ito, "Implanted Planar Inverted F-Antenna for Cardiac Pacemaker System," in *International Workshop on Antenna Technology: Small Antennas and Novel Metamaterials, 2008. iWAT 2008*, 2008, pp. 346–349.

[50] P. Soontornpipit, C. M. Furse, and Y. C. Chung, "Design of implantable microstrip antenna for communication with medical implants," *IEEE Trans. Microw. Theory Tech.*, vol. 52, no. 8, pp. 1944–1951, Aug. 2004.

[51] T. Karacolak, A. Hood, and E. Topsakal, "Design of a Dual-Band Implantable Antenna and Development of Skin Mimicking Gels for Continuous Glucose Monitoring," *IEEE Trans. Microw. Theory Tech.*, vol. 56, no. 4, pp. 1001–1008, Apr. 2008.

[52] G. L. Stuber, J. R. Barry, S. W. McLaughlin, Y. Li, M.-A. Ingram, and T. G. Pratt, "Broadband MIMO-OFDM wireless communications," *Proc. IEEE*, vol. 92, no. 2, pp. 271–294, 2004.

[53] Y. Ouyang, D. J. Love, and W. J. Chappell, "Body-Worn Distributed MIMO System," *IEEE Trans. Veh. Technol.*, vol. 58, no. 4, pp. 1752–1765, 2009.

[54] Y. Wang, I. B. Bonev, J. O. Nielsen, I. Z. Kovacs, and G. F. Pedersen, "Characterization of the Indoor Multiantenna Body-to-Body Radio Channel," *IEEE Trans. Antennas Propag.*, vol. 57, no. 4, pp. 972–979, 2009.

[55] "'ANSYS Physiological Modeling' [Online]. Available: http://www.ansys.com/Industries/Healthcare/Physiological+Modeling [Accessed: 8-Oct-2014]."

[56] K. S. Deepak and A. V. Babu, "Optimal packet size for energy efficient WBAN under m-periodic scheduled access mode," in *2014 Twentieth National Conference on Communications (NCC)*, 2014, pp. 1–6.

[57] C. S. Lin and P. J. Chuang, "Energy-efficient two-hop extension protocol for wireless body area networks," *IET Wirel. Sens. Syst.*, vol. 3, no. 1, pp. 37–56, Mar. 2013.

[58] C. Gabriel, "Compilation of the Dielectric Properties of Body Tissues at RF and Microwave Frequencies.," Jun. 1996.

[59] M. H. Mat, M. F. b A. Malek, A. Omar, M. S. Zulkefli, and S. H. Ronald, "Analysis of the correlation between antenna gain and SAR Levels inside the human head model at 900MHz," in *2012 Asia-Pacific Symposium on Electromagnetic Compatibility*, 2012, pp. 513–516.

[60] M. Ahmed, “Investigating Radiation Hazard and Safety Aspects of Handheld Mobile,” in *2009 Third International Conference on Mobile Ubiquitous Computing, Systems, Services and Technologies*, 2009, pp. 1–9.

[61] C. Lazarescu, I. Nica, and V. David, “SAR in human head due to mobile phone exposure,” in *2011 E-Health and Bioengineering Conference (EHB)*, 2011, pp. 1–4.

[62] T. Koike-Akino, “SAR Analysis in Dispersive Tissues for *In Vivo* UWB Body Area Networks,” in *GLOBECOM 2009 - 2009 IEEE Global Telecommunications Conference*, 2009, pp. 1–6.

[63] S. Aoyama, D. Anzai, and J. Wang, “SAR evaluation based on required BER performance for 400 MHz implant BANs,” in *2012 Asia-Pacific Symposium on Electromagnetic Compatibility*, 2012, pp. 365–368.

[64] S. Gezici, H. Kobayashi, H. V. Poor, and A. F. Molisch, “Performance evaluation of impulse radio UWB systems with pulse-based polarity randomization in asynchronous multiuser environments,” in *2004 IEEE Wireless Communications and Networking Conference (IEEE Cat. No.04TH8733)*, 2004, vol. 2, p. 908–913 Vol.2.

[65] K. Witrisal *et al.*, “Noncoherent ultra-wideband systems,” *IEEE Signal Process. Mag.*, vol. 26, no. 4, pp. 48–66, Jul. 2009.

[66] T. Wang, W. Heinzelman, and A. Seyedi, “Link Energy Minimization in IR-UWB Based Wireless Networks,” *IEEE Trans. Wirel. Commun.*, vol. 9, no. 9, pp. 2800–2811, Sep. 2010.

[67] *Ultra-Low-Power Short-Range Radios | Patrick P. Mercier | Springer*. .

[68] M. S. Bazaraa, C. M. Shetty, and H. D. Sherali, *Nonlinear programming: theory and algorithms*. 1993.

[69] S. Boyd and L. Vandenberghe, *Convex Optimization*. Cambridge University Press, 2004.

[70] R. Horst and P. M. Pardalos, *Handbook of Global Optimization*. Springer Science & Business Media, 2013.

[71] “Yazdandoost, Kamya Yekeh, and Kamran Sayrafian-Pour. ‘Channel model for body area network (BAN).’ IEEE P802 15 (2009): 08-0780.”

[72] G. Bianchi, “Performance analysis of the IEEE 802.11 distributed coordination function,” *IEEE J. Sel. Areas Commun.*, vol. 18, no. 3, pp. 535–547, Mar. 2000.

[73] L. Giarre, G. Neglia, and I. Tinnirello, “Medium access in WiFi networks: strategies of selfish nodes [Applications Corner],” *IEEE Signal Process. Mag.*, vol. 26, no. 5, pp. 124–128, Sep. 2009.

[74] M. Cagalj, S. Ganeriwal, I. Aad, and J. P. Hubaux, “On selfish behavior in CSMA/CA networks,” in *Proceedings IEEE 24th Annual Joint Conference of the IEEE Computer and Communications Societies.*, 2005, vol. 4, pp. 2513–2524 vol. 4.

APPENDIX A: COPYRIGHT PERMISSIONS

Below is permission for the use of material in Chapter 1, 2 and 4.

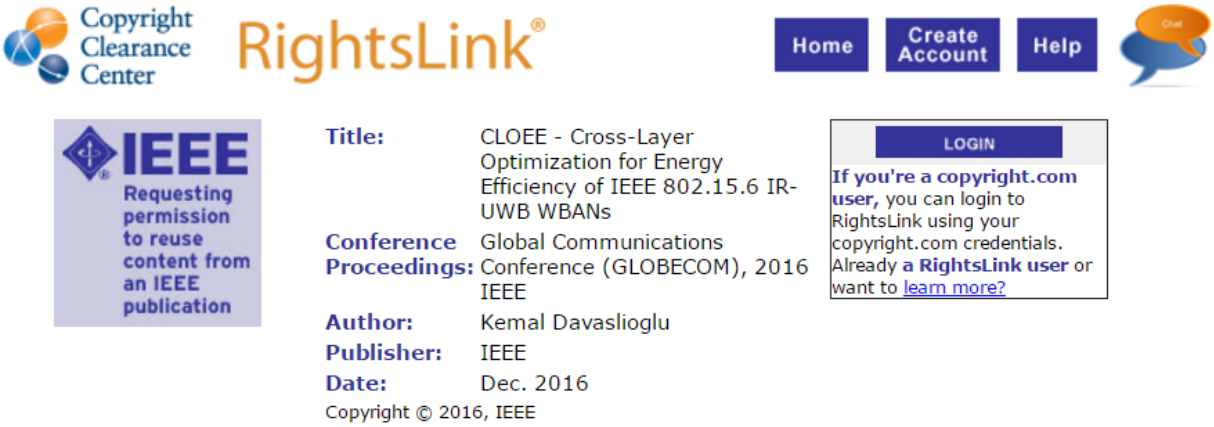

Copyright Clearance Center RightsLink®

Home | Create Account | Help

IEEE Requesting permission to reuse content from an IEEE publication

Title:	CLOEE - Cross-Layer Optimization for Energy Efficiency of IEEE 802.15.6 IR-UWB WBANs
Conference Proceedings:	Global Communications Conference (GLOBECOM), 2016 IEEE
Author:	Kemal Davaslioglu
Publisher:	IEEE
Date:	Dec. 2016

Copyright © 2016, IEEE

LOGIN

If you're a copyright.com user, you can login to RightsLink using your copyright.com credentials. Already **a RightsLink user** or want to learn more?

Thesis / Dissertation Reuse

The IEEE does not require individuals working on a thesis to obtain a formal reuse license, however, you may print out this statement to be used as a permission grant:

Requirements to be followed when using any portion (e.g., figure, graph, table, or textual material) of an IEEE copyrighted paper in a thesis:

1) In the case of textual material (e.g., using short quotes or referring to the work within these papers) users must give full credit to the original source (author, paper, publication) followed by the IEEE copyright line © 2011 IEEE.
2) In the case of illustrations or tabular material, we require that the copyright line © [Year of original publication] IEEE appear prominently with each reprinted figure and/or table.
3) If a substantial portion of the original paper is to be used, and if you are not the senior author, also obtain the senior author's approval.

Requirements to be followed when using an entire IEEE copyrighted paper in a thesis:

1) The following IEEE copyright/ credit notice should be placed prominently in the references: © [year of original publication] IEEE. Reprinted, with permission, from [author names, paper title, IEEE publication title, and month/year of publication]
2) Only the accepted version of an IEEE copyrighted paper can be used when posting the paper or your thesis on-line.
3) In placing the thesis on the author's university website, please display the following message in a prominent place on the website: In reference to IEEE copyrighted material which is used with permission in this thesis, the IEEE does not endorse any of [university/educational entity's name goes here]'s products or services. Internal or personal use of this material is permitted. If interested in reprinting/republishing IEEE copyrighted material for advertising or promotional purposes or for creating new collective works for resale or redistribution, please go to http://www.ieee.org/publications_standards/publications/rights/rights_link.html to learn how to obtain a License from RightsLink.

If applicable, University Microfilms and/or ProQuest Library, or the Archives of Canada may supply single copies of the dissertation.

Below is permission for the use of material in Chapter 3.

Thesis / Dissertation Reuse

The IEEE does not require individuals working on a thesis to obtain a formal reuse license, however, you may print out this statement to be used as a permission grant:

Requirements to be followed when using any portion (e.g., figure, graph, table, or textual material) of an IEEE copyrighted paper in a thesis:

1) In the case of textual material (e.g., using short quotes or referring to the work within these papers) users must give full credit to the original source (author, paper, publication) followed by the IEEE copyright line © 2011 IEEE.
2) In the case of illustrations or tabular material, we require that the copyright line © [Year of original publication] IEEE appear prominently with each reprinted figure and/or table.
3) If a substantial portion of the original paper is to be used, and if you are not the senior author, also obtain the senior author's approval.

Requirements to be followed when using an entire IEEE copyrighted paper in a thesis:

1) The following IEEE copyright/ credit notice should be placed prominently in the references: © [year of original publication] IEEE. Reprinted, with permission, from [author names, paper title, IEEE publication title, and month/year of publication]
2) Only the accepted version of an IEEE copyrighted paper can be used when posting the paper or your thesis on-line.
3) In placing the thesis on the author's university website, please display the following message in a prominent place on the website: In reference to IEEE copyrighted material which is used with permission in this thesis, the IEEE does not endorse any of [university/educational entity's name goes here]'s products or services. Internal or personal use of this material is permitted. If interested in reprinting/republishing IEEE copyrighted material for advertising or promotional purposes or for creating new collective works for resale or redistribution, please go to http://www.ieee.org/publications_standards/publications/rights/rights_link.html to learn how to obtain a License from RightsLink.

If applicable, University Microfilms and/or ProQuest Library, or the Archives of Canada may supply single copies of the dissertation.

Below is the permission for the use of material in Chapter 4, 5, 6.

- **Does IEEE require individuals working on a thesis or dissertation to obtain formal permission for reuse?**

The IEEE does not require individuals working on a thesis to obtain a formal reuse license, however, you must follow the requirements listed below:

Textual Material

Using short quotes or referring to the work within these papers) users must give full credit to the original source (author, paper, publication) followed by the IEEE copyright line © 2011 IEEE.

In the case of illustrations or tabular material, we require that the copyright line © [Year of original publication] IEEE appear prominently with each reprinted figure and/or table.

If a substantial portion of the original paper is to be used, and if you are not the senior author, also obtain the senior author's approval.

Full-Text Article

If you are using the entire IEEE copyright owned article, the following IEEE copyright/ credit notice should be placed prominently in the references: © [year of original publication] IEEE. Reprinted, with permission, from [author names, paper title, IEEE publication title, and month/year of publication]

Only the accepted version of an IEEE copyrighted paper can be used when posting the paper or your thesis on-line.

In placing the thesis on the author's university website, please display the following message in a prominent place on the website: In reference to IEEE copyrighted material which is used with permission in this thesis, the IEEE does not endorse any of [university/educational entity's name goes here]'s products or services. Internal or personal use of this material is permitted. If interested in reprinting/republishing IEEE copyrighted material for advertising or promotional purposes or for creating new collective works for resale or redistribution, please go to http://www.ieee.org/publications_standards/publications/rights/rights_link.html to learn how to obtain a License from RightsLink.

If applicable, University Microfilms and/or ProQuest Library, or the Archives of Canada may supply single copies of the dissertation.

ABOUT THE AUTHOR

Yang Liu received his B.S. degree in Biology Science from Wuhan University in 2010 and his M.S. degree in Electrical Engineering from Beijing University of Posts and Telecommunications in 2013. Currently he is pursuing the Ph.D. degree in Electrical Engineering in University of South Florida and expect to graduate in Spring 2017. His research interests include *in vivo* wireless communications and networking, energy efficiency optimization in networks, and game theoretical applications in wireless networking.